NTNU
Norwegian University of
Science and Technology

Description and Analysis of Floating Bridges

Kristina Husevåg Lund

Marine Technology
Submission date: June 2017
Supervisor: Bernt Johan Leira, IMT

Norwegian University of Science and Technology
Department of Marine Technology

NTNU
Norwegian University of
Science and Technology

Description and Analysis of Floating Bridges

Kristina Husevåg Lund

June 9, 2017

Supervisor: Professor Bernt Johan Leira
Department of Marine Technology

Master Thesis, Spring 2017

for

Stud. Techn. Kristina Husevåg Lund

Description and Analysis of Floating Bridges

Beskrivelse og analyse av flytebroer

Floating bridges are relevant for crossing of very deep and wide lakes of fjord systems. In order to compute the static and dynamic response of these bridges, the joint properties of the whole hydro-elastic system need to be accounted for. The objective of the present project is to outline methods for the response analysis and illustrate the calculation procedure for a particular example structure.

The following subjects are to be addressed as part of this work:

1. A review is to be made of existing floating bridges and future planes for such bridges. Similarities and differences between the different bridges are to be highlighted.

2. The loads which are acting on such bridges are to be described and associated structural models are discussed. Corresponding methods for both static and dynamic response analysis are elaborated and relevant numerical algorithms are described.

3. A specific example of a floating bridge structure is to be selected for the purpose of illustrate the modelling aspects and calculation procedures. The selection of the example structure is to be made based on discussion with the supervisor.

4. Parameter studies are performed (to the extent that time allows) with respect to variation of the geometry and the associated natural frequencies (and mode shapes) for the example structure. It is relevant that the type and extent of such parameter variation are agreed upon with the supervisor during the course of the project study.

The work scope may prove to be larger than initially anticipated. Subject to approval from the supervisor, topics may be deleted from the list above or reduced in extent.

In the thesis, the candidate shall present her personal contribution to the resolution of problems within the scope of the thesis work. Theories and conclusions should be based on mathematical derivations and/or logic reasoning identifying the various steps in the deduction.

The candidate should utilise the existing possibilities for obtaining relevant literature.

The thesis should be organised in a rational manner to give a clear exposition of results, assessments, and conclusions. The text should be brief and to the point, with a clear language. Telegraphic language should be avoided.

The thesis shall contain the following elements: A text defining the scope, preface, list of contents, summary, main body of thesis, conclusions with recommendations for further work, list of symbols and acronyms, references and (optional) appendices. All figures, tables and equations shall be numbered.

The supervisor may require that the candidate in early stage of work, presents a written plan for completion of the work. The original contribution of the candidate and material taken from other sources shall be clearly defined. Work from other sources shall be properly referenced using an acknowledge referencing system.

The thesis shall be submitted in electric form:

- Signed by the candidate
- The text defining the scope included
- In bound volume(s)
- Drawing and/or computer prints which cannot be bound should be organised in a separated folder

Supervisor: Professor Bernt J. Leira

Trondheim, 15. Januar 2017

Bernt J. Leira

Preface

This master's thesis is the product of the work performed by student Kristina Husevåg Lund during the spring semester 2017 at the Norwegian University of Science and Technology. The master's thesis is based on the work performed in the project thesis during the fall of 2016. The assignment has been to demonstrate how static and dynamic analyses can be performed on a simplified model of a floating bridge. The chosen bridge is a proposed crossing of Bjørnafjorden. In addition, three other bridges were analysed to study how variations of cross-section geometry and number of supports affect the responses.

The scope was purposed by my supervisor Professor Bernt Johan Leira, and I would like to thank him for guidance throughout the work with my thesis. Finally, I would like to thank my classmates for help when performing the analyses and for proofreading.

Trondheim, June 9, 2017

Kristina H. Lund

Abstract

During the project Ferry-free coastal route E39, directed by National Public Road Administration, NPRA, seven ferry-crossings are intended to be replaced by straight crossing. One of these is Bjørnafjorden, where a proposed crossing is a multi-span suspension bridge, supported by two tension leg platforms, TLPs. A simplified model of this proposed crossing was created in Abaqus/CAE. Further, three additional models were created to study how the number of supports and alteration of cross-section affect the responses.

The first two horizontal eigenfrequencies were compared to available eigenfrequencies from NPRA. All models had higher eigenfrequencies, which indicates that the models are stiffer, or that the mass and added mass are smaller, or a combination.

For the static analysis, three loads were applied. These were current at the floater and traffic and wind along the bridge. The environmental loads were determined for 1-year, 50-year and 100-year return periods. The longitudinal and vertical displacement along the bridge, in addition to bending moment, were determined for every model. When the number of supports were increased, the vertical displacement was significantly reduced, while the largest vertical displacement occurred for the model with reduced thickness of the horizontal beams in the cross-section. This was also true for the longitudinal displacement when only the environmental loads were applied.

For the dynamic analysis, an incoming harmonic wave was applied in horizontal and vertical direction at the floater. Two wave periods were utilized; the first is a feasible period and the second is the first obtained eigenperiod. Resonance caused significantly larger motions for the floaters. Generally, a reduction of the cross-section's thickness on horizontal beams resulted in an increased sway response, while the largest response in heave occurred for a reduced cross-section height.

Norsk sammendrag

I prosjektet Ferjefri E39, ledet av Statens Vegvesen, er intensjonen å erstatte syv fergekrysninger med faste veiforbindelser. En av krysningene er over Bjørnafjorden, hvor ett forslag er å bruke en hengebru med flere spenn understøttet av to TLP flytere. En forenklet modell av denne løsningen var laget i programmet Abaqus/CAE. I tillegg ble tre lignende modeller laget for å se hvordan antall flytere og endringer av tverrsnittet på modellene, påvirker responsene.

De to første horisontale egenfrekvensene ble sammenlignet med de fra Statens Vegvesen. Det var da tydelig at alle modellene hadde høyere egenfrekvenser, noe som indikerer at enten modellene er stivere, eller de har en mindre masse, eller en kombinasjon.

I den statiske analysen ble tre laster påført. Det var strømninger på flyterne, trafikk og vind langs broen. Strømninger og vind var bestemt for 1-års periode, 50-års periode og 100-års periode. Horisontale og vertikale forflytninger langs modellene i tillegg til bøyemomentet, ble bestemt for hver modell. Modellen med en ekstra flyter hadde en betydelig reduksjon i vertikal forflytning, mens modellen med redusert tykkelse på de horisontale bjelkene i tverrsnittet hadde de største forflytningene. Dette skjedde også for horisontal forflytning når kun strømninger og vind var påført.

I den dynamiske analysen ble en horisontal og vertikal bølge påført flyterne. To bølgeperioder var brukt, hvor den første er en realistisk periode, mens den andre er den første horisontale og vertikale egenperiode. Resonans skapte betydelige større bevegelser for flyterne. Generelt ga modellen med redusert horisontale bjelker i tverrsnittet størst respons i svai, mens modellen med redusert høyde på tverrsnittet ga størst bevegelser i hiv.

Contents

List of Figures

List of Tables

Nomenclature

Abbreviations

Symbol	Description
COB	Centre of Buoyancy
COG	Centre of Gravity
DNV	Det Norske Veritas
NLGEOM	Geometric non-linearity
NPRA	National Public Road Administration
TLP	Tension Leg Platform

Roman Symbols

Symbol	Description
A	Cross-section
$\mathbf{A}$	Frequency added mass matrix
$\mathbf{A}$	Quadratic matrix
$A_{i,j}$	Added mass in i-direction caused by acceleration in j-direction
A_S	Cross-section area
A_{wp}	Waterplane area
a	Site- and height dependent parameter
a_i	Acceleration in i-direction
B	Buoyancy of platform
$B_{i,j}$	Damping in i-direction caused by velocity in j-direction
b	Site- and height dependent parameter
C	Arbitrary function dependent on time
$\mathbf{C}$	Damping matrix
C	Hydrostatic stiffness
C	Shape coefficient
$C_{a,i}$	Added mass coefficient
C_d	Drag coefficient

$C_{i,j}$	Restoring force in i-direction caused by displacement in j-direction
C_m	Mass coefficient
$\mathbf{C_2}$	Frequency dependent hydrodynamic damping coefficient
C_{33}	Hydrostatic stiffness in heave
C_{44}	Hydrostatic stiffness in roll
C_{55}	Hydrostatic stiffness in pitch
c_i	Arbitrary constant
D	Diameter to the floater
d	Water depth to still water level
dF	Horizontal force per unit length on a strip
d_0	Reference depth for wind generated current
E	Young's modulus
$\mathbf{F}$	Force matrix
F	Function
F	Horizontal force
$F_{current}$	Current force
$F_{diff,i}$	Diffraction force in x-, y- or z-direction
F_i	Force in x-, y- or z-direction
F_{tot}	Total force
$F_{U_{10,max},1year}$	Annual maximum of the 10-minutes mean wind speed
F_{wind}	Wind force
f	Eigenfrequency in Hz
g	Standard acceleration due to gravity
H	Cross-section height
H_{mo}	Significant wave height if measured from spectre
H_s	Significant wave height
h	Inner height
h	Water depth
h_1	Height for caisson
h_2	Height for cylinder
$\mathbf{I}$	Identity matrix

I	Moment of inertia
I_x	Moment of inertia about x-axis of all tethers
I_y	Moment of inertia about y-axis of all tethers
I_{wpx}	Moment of inertia
I_{wpy}	Moment of inertia
$\mathbf{i}$	Unit vector along the x-axis
$\mathbf{j}$	Unit vector along the y-axis
$\mathbf{K}$	Stiffness matrix
K_C	Conventional stiffness
K_G	Geometrical stiffness
$\mathbf{K_I}$	Incremental stiffness
K_p	Total stiffness
$\mathbf{k}$	Hydrostatic restoring forces
k	Factor
k	Modulus of foundation
$\mathbf{k}$	Unit vector along the z-axis
k	Wave number
k_{11}^G	Geometric stiffness in surge
k_{22}^G	Geometric stiffness in sway
k_{33}^C	Conventional stiffness in heave
k_{44}^C	Conventional stiffness in roll
k_{66}^C	Conventional stiffness in yaw
k_{66}^G	Geometric stiffness in yaw
L	Length
$\mathbf{L}$	Lower triangular matrix
$\mathbf{L}^T$	Upper triangular matrix
$\mathbf{M}$	Mass matrix
M_{max}	Maximum moment
M2	Bending moment
$m_{added,i}$	Added mass in x-, y- and z-direction
$\mathbf{n_i}$	Unit vector

n_l	Integer number of notional lanes
P	Concentrated load
p	Water pressure
p_0	Atmospheric pressure
Q_i	Concentrated load for notional lane no. i
Q_{ik}	Characteristic load
q	Wind pressure
$q_{footpath}$	Footpath load
q_i	Uniformly distributed load for notional lane no. i
q_{ik}	Characteristic load
$q_{remaining}$	Load magnitude for the remaining area
q_{rk}	Characteristic load
$q_{traffic}$	Traffic load
$\mathbf{R}$	External loads
$\mathbf{R_{int}}$	Internal load
$\mathbf{R_m}$	External load for step m
$\mathbf{R_{m+1}}$	External loads for step $m+1$
$\mathbf{r}$	Displacement for the system
$\dot{\mathbf{r}}$	Velocity to the system
$\ddot{\mathbf{r}}$	Acceleration of the system
$\mathbf{r_m}$	Displacement for the system for step m
$\mathbf{r_{m+1}}$	Displacement for the system for step $m+1$
r_1	Radius for caisson
r_2	Radius for cylinder
S	Projected area
S	Wet surface area
T	Eigenperiod in seconds
T	Wave period
T_h	Eigenperiod for horizontal movement
T_n	Tether tension force
T_p	Wave period

T_R	Return period
T_v	Eigenperiod for vertical movement
t	Time
t_1	Thickness for vertical beams
t_2	Thickness for horizontal beams
$U_{T,z}$	Wind velocity averaged over a time interval T at height z above mean water level
U_w	Wind velocity
$U_{1hour,10min}$	1 hour sustained wind speed at height of 10 metres above sea level
U2	Vertical displacement
U3	Longitudinal displacement
U_{10,T_R}	10-minute mean wind speed with return period T_R
$U_{10,max}$	Maximum of the 10-minutes mean wind speed
u	Fluid velocity
u	Velocity in x-direction
$\dot{u}$	Fluid acceleration
$\mathbf{V}$	Fluid velocity potential
V_{max}	Maximum shear force
V_R	Reference volume
v_c	Current velocity
$\mathbf{v_c}$	Current velocity vector
$\mathbf{v_{c,circ}}$	Circulation current vector
$\mathbf{v_{c,tide}}$	Tide generated current vector
$v_{c,tide}$	Tide generated velocity
$\mathbf{v_{c,wind}}$	Wind generated current vector
$v_{c,wind}$	Wind generated current velocity
W	Cross-section width
W	Weight of platform
w	Carriageway width
w	Inner width
w_l	Width to each notional lanes

x	Coordinate axis
$\mathbf{x}$	New eigenvector
x_n	Distance from mid-point of the floater in x-direction
y	Coordinate axis
y_{max}	Maximum displacement
y_n	Distance from mid-point of the floater in y-direction
$\mathbf{z}$	An approximation to the eigenvector
$\mathbf{z_k}$	An approximation to the eigenvector for k
$\mathbf{z_{k-1}}$	An approximation to the eigenvector for $k-1$
z	Coordinate axis
z	Distance from still water level, draught
z_B	Vertical coordinates of buoyancy
z_G	Vertical coordinates of gravity centre
z_T	Vertical coordinates of tendon top

Greek Symbols

Symbol	Description
α	Angle
α	Exponent
α_{Qi}	Adjustment factor
α_{qi}	Adjustment factor
α_{qr}	Adjustment factor
Δ	Delta
ζ	Wave elevation
ζ_a	Wave amplitude
η_j	Displacement in j-direction
η_1	Surge
η_2	Sway
η_3	Heave
η_4	Roll

η_5	Pitch
η_6	Yaw
$\dot{\eta}_j$	Velocity in j-direction
$\ddot{\eta}_j$	Acceleration in j-direction
θ	Eigenvalue
λ	Constant
λ	Eigenvalue
λ	Stiffness ratio
λ	Wavelength
λ_i	New eigenvalue
$\bar{\lambda}_i$	Previous eigenvalue
λ_R	Rayleigh quotient
μ	Eigenvalue
μ	Shift
ν_{steel}	Poisson's ratio for steel
ρ	Sea density
ρ_a	Mass density of air
$\rho_{concrete}$	Density to concrete
ρ_{steel}	Density to steel
ϕ	Eigenvector
ϕ	Velocity potential
ω	Eigenfrequency in rad/s
ω	Wave frequency
ω_i	Eigenfrequency no. i
ω_i	Frequency no. i
∇	Differential operator

1 Introduction

The project Ferry-free coastal route E39, directed by National Public Road Administration, NPRA, has an ambition to improve E39 and replace ferry-crossings with straight crossings within 2035[1]. The project involves seven ferry-crossings which are intendent to be replaced by straight crossings, where the floating bridge concept is a possibility for several of these. Floating bridges are highly convenient in situations where the crossing has a large width or large depth, or where conventional foundations are inconvenient because of the soft seabed[2]. However, due to the dimension of some of the ferry-crossings, modification or new technology must be utilized.

This thesis gives a description and an overview of different types of floating bridges, and existing floating bridges are briefly described. Further, an eigenvalue analysis, static analysis and dynamic analysis are illustrated on a simplified model by utilizing the software Abaqus/CAE. The theory behind the analyses and the calculated applied loads are described.

1.1 Background

The planned Ferry-free coastal route E39, between Kristiansand and Trondheim, is seen in figure 1. Ferry-crossings intended to be replaced by fixed straight crossings are Boknafjorden, Bjørnafjorden, Sognefjorden, Nordfjord, Sulafjorden, Romsdalsfjorden and Halsafjorden[3]. The width and depth for some of these crossings present a challenge. Hence, well-known concepts, such as the traditional floating bridge and the suspension bridge, must be modified or new technology, such as the submerged floating tunnel, must be applied. When evaluating the different concepts, ship traffic must be assessed, and a low influence on current and future ship traffic is a requirement[3].

Figure 1: Future planned fjords crossings in Norway[1]

A multi-span suspension bridge and a subsea tunnel has been studied as crossings of Boknafjorden. A ship channel with a height of 70 metre and width of 400 metre is required if the multi-span suspension bridge is chosen[3]. However, it has been decided that a subsea tunnel will be constructed because of the cost[3]. For Bjørnafjorden, mainly five concepts have been considered. These are a suspension bridge with one main-span, a multi-span suspension bridge, a floating bridge with sideway-anchors, a floating bridge end-anchored and a submerged floating tunnel[3]. For the multi-span suspension bridge, one or two pontoons or Tension Leg Platforms, TLPs, are intended to support the bridge. The crossing of Sognefjorden has been located between Lavik and Oppedal, where the depth and width

is 1250 metre and 3700 metres, respectively[3]. Because of its dimensions, it is concluded that for this crossing, new technology is needed[1]. As a crossing of Nordfjord, a suspension bridge is considered as the most favourable[3].

Sulafjorden has a width of 3100 metre at its narrowest[3]. However, in this area, the bridge is exposed to waves, and by moving the bridge to a more protected area, the crossing distance increases. For this crossing, a floating bridge, a submerged floating tunnel, and a suspension bridge has been considered as possible crossings[3]. Three alignment roads have been studied for crossing Romsdalsfjorden, where one or several subsea tunnels are included in the design[3]. In addition to a subsea tunnel, a suspension bridge with a main span of 1600 metre are involved in the crossing for one of the alignment roads. Since several bridges with a main span of 1600 metre or more have been constructed, this is deemed possible. However, more data is needed before the decision of which alignment road to realise can be made[3].

A suspension bridge, a floating bridge and a submerged floating tunnel have been studied as crossings of Halsafjorden, nonetheless, it has been decided that a suspension bridge will be applied[1]. However, if a submerged floating tunnel is ever to be built, the pilot test will be in Halsafjorden[1].

1.2 Objective

The objective of this thesis, is to study a simplified model subjected for static and dynamic loads. A simplified model of one proposed design of Bjørnafjorden Bridge is utilized as an example to illustrate the analyses. The main questions that are studied in this thesis are:

1. How a simplified model will respond to environmental and traffic loads
2. How an increased number of support effects the eigenvalue and static and dynamic responses
3. How the cross-section effects the eigenvalue and static and dynamic responses

The analyses were performed on four models where the first is a simplified model of the proposed design for Bjørnafjorden Bridge. The second model is similar as the first model, but the height of the cross-section is reduced. The third model has the same cross-section as the first model with expectance of the reduced thickness of the horizontal beams of the cross-section. The last model has the same cross-section as the first model, but the number of support is increased. By comparing the results achieved for each model, it can be study how these chosen parameters affect the responses.

1.3 Scope and limitations

Static and dynamic analyses on a floating bridge are illustrated on a simplified model. The only loads applied during the analyses, is current, traffic, wave, and wind. In addition, the applied loads are estimated based on assumptions and simplifications. Fatigue and serviceability concern are neglected, even though this can have a major influence on the results.

1.4 Different types of floating bridges

A floating bridge can be simplified as a beam supported by floating elements, which are defined as either pontoon-structures or as semi-submersible structures[4]. A pontoon-structure is a floating component with a small depth compared to its width, and is suitable in areas with calm water, such as inside a cove or near

the coastline[4]. Semi-submersible structures consist of columns with watertight ballast compartments attached to pontoons, and due to the ballast compartment, they are appropriate for large wavelengths and wave heights[4]. In addition to floating bridges, modification of known concepts and new technology, such as submerged floating tunnel and suspension bridges supported by TLPs, are discussed in this section.

Conventional floating bridge

For conventional floating bridges, the pontoons can be connected to each other or individually separated. By having connected pontoons, the ship traffic is significant influenced and lateral forces are larger compared to separated pontoons[5]. Even though separated pontoons have a smaller influence on ship traffic, the risk of ship impacts due to the high number of pontoons, remains[6]. Since several floating bridges have been constructed, the existing broad knowledge is a major advantage for this concept. Some existing floating bridges are briefly described in the following.

Lacey V. Murrow Memorial Bridge across Lake Washington was inaugurated in 1940 and is seen in figure 2. It was the first permanent highway concrete floating bridge, and was supported by 25 reinforced connected concrete pontoons[7]. During a rainstorm in 1990, while undergoing a renovation, eight pontoons sank and the remaining pontoons suffered major damage[7]. The reconstruction of the bridge was completed in 1993, and the number of pontoons was reduced to 20[7]. Evergreen Point Bridge, seen in figure 3, was opened for traffic in 1963 to satisfy the need of an additional crossing over Lake Washington[7]. The bridge is supported by concrete pontoons which are pre-stressed longitudinally and rigidly connected[7]. In 1989, the third bridge across Lake Washington, Homer M. Hadley Memorial Bridge, was built 18.3 metre north of Lacey V. Murrow Memorial Bridge[7], seen in figure 2.

Figure 2: The Lacey V. Murrow Memorial Bridge at the right and the Homer M. Hadley Bridge at the left[7]

Figure 3: The Second Lake Washington Bridge[8]

The Hood Canal Bridge in USA was completed in 1961. 23 reinforced and longitudinally pre-stressed concrete pontoons, rigidly connected, supported the bridge[7]. During a storm in 1979, the western half of the bridge was destroyed and had to be replaced. Since the new half was built with better material and under stricter criteria, the eastern part was replaced with a similar design in 2009[7]. The new eastern half is seen in figure 4.

Figure 4: The new eastern half of the Hood Canal Bridge[7]

Bergøysund Bridge is the first Norwegian floating bridge, and is seen in figure 5. It was completed in 1992, and is a tubular truss superstructure supported by seven pontoons[9]. It has a shape of an arc, which is useful since forces caused by wind, wave and current are transformed to axial forces to the land abutments[10][11]. The second floating bridge in Norway is Nordhordland Bridge, north of Bergen, and is seen in figure 6. Nordhordland Bridge was opened for traffic in 1994, and is designed as a steel box girder supported by ten concrete pontoons[12]. Small boats can pass between the pontoons, while ship traffic uses the 50 metres wide and 32 metres height ship channel[12]. To date, it has two traffic lanes and one sidewalk, but with a possibility to upgrade to three traffic lanes and two sidewalks[12].

Figure 5: Bergøysund Bridge[6]

Figure 6: Nordhordland Bridge[6]

In London, a 94-metres-long pedestrian pontoon floating bridge, West India Quay Footbridge, was completed in 1997[13] and is seen in figure 7.

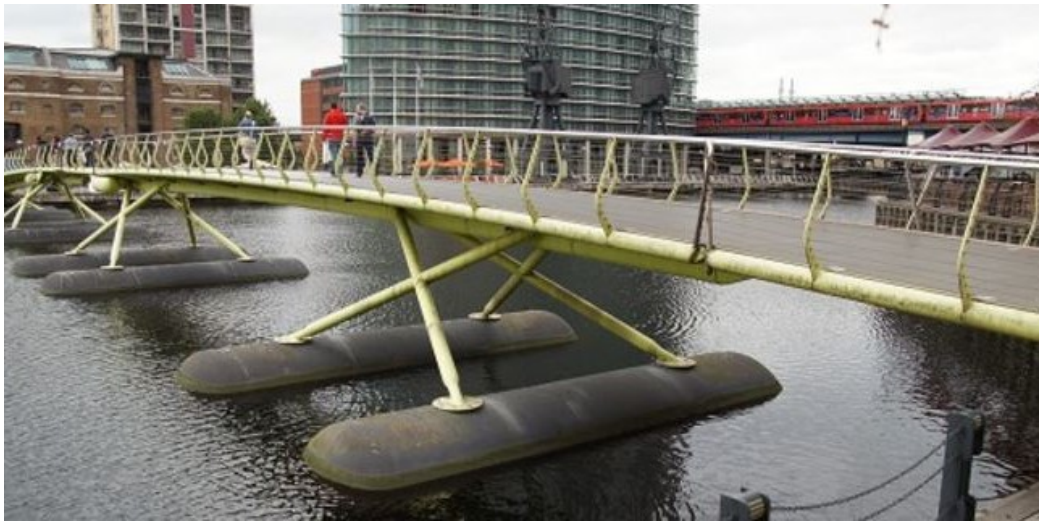

Figure 7: West India Quay Footbridge[14]

Ford Island Bridge, also known as Admiral Clarey Bridge, was open for traffic in 1997 at Pearl Harbour in Hawaii, where pontoons support the 457-meter-long concrete bridge[13] and is seen in figure 8.

Figure 8: The Ford Island Bridge[15]

The first floating swing bridge in the world, the Yumemai Bridge in Japan, was completed in 2001[16]. It has a 410-metre floating part resting on two hollow steel pontoons with cathodic protection.[16], as seen in figure 9.

Figure 9: The Yumemai Bridge[16]

In 2007, Bur Dubai and Deira section of Dubai was connected by a floating concrete bridge[4], and the bridge is seen in figure 10.

Figure 10: Dubai Floating Bridge[17]

The five-lane floating bridge William R. Bennett Bridge, seen in figure 11, opened to traffic across Lake Okanagan in Canada in 2008[2]. The bridge was built to improve safety and mitigate the increased traffic, and replaced an existing bridge.

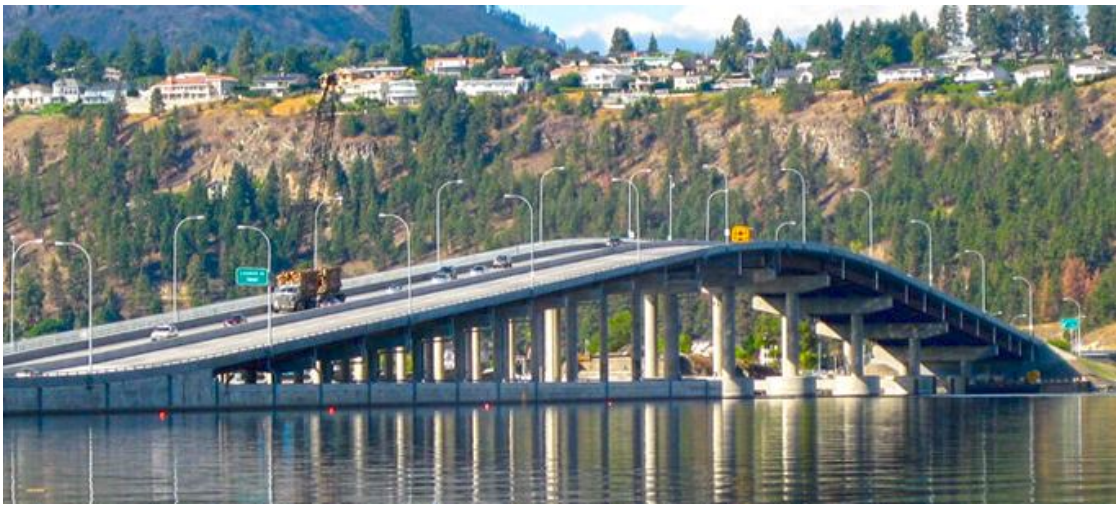

Figure 11: William R. Bennett Bridge[18]

Submerged floating tunnel

The second concept is the submerged floating tunnel which has never been constructed before. Yet, it was considered and approved for the Høgsfjord project[19]. Cars are driving through a submerged tube, and the tube is either supported by pontoons or tethers, see figure 12. The tether stabilization will not influence the ship traffic since it has no element close to the sea surface. Since the tethers are dependent of the condition to the seabed, there is a need of seabed investigation and satisfying seabed condition[20]. On the other hand, the pontoon stabilization is not dependent on the seabed, but the pontoons will influence the ship traffic. In addition, there is a weak connection between the tube and the pontoons, so further experimental testing and documentation are required[20].

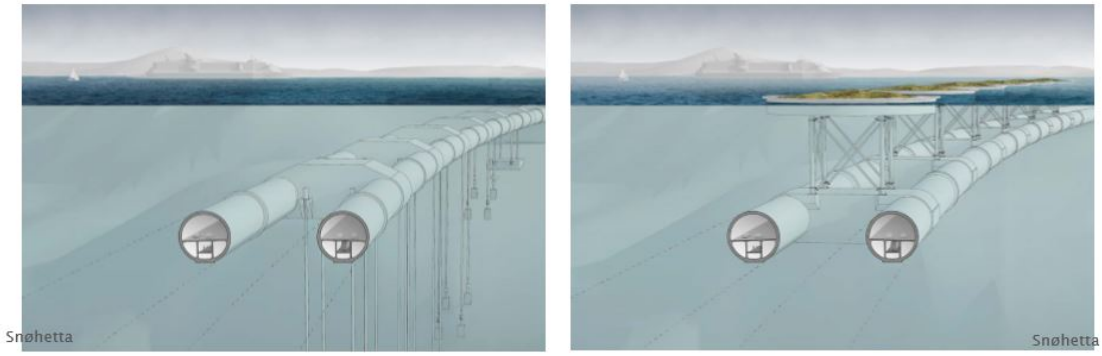

Figure 12: Tether supported, left, and pontoon supported, right, submerged floating tunnel[20]

Suspension bridge

The third concept is the suspension bridge, where the largest existing main span belongs to Akashi Kaikyo Bridge in Japan, which is 1991 metre[3]. However, the crossings investigated in the project Ferry-free E39, are considerable longer. One advantage of the suspension bridge, is that the ship traffic will be less influenced since there is a larger distance between the support, compared to floating bridges[3]. However, the complex cable system will be exposed for larger aerodynamic effects[3]. By applying TLPs instead of pontoons, the number of supports needed, decreases. TLPs are efficient for water depth of 300 to 600 metre[21]. It anchors the bridge to the seabed by pre-tensioned tethers, and introduce an additional stiffness[3]. Even though this is a familiar concept in the offshore industry, a TLP as support for a bridge has never been utilized before[22]. Figure 13 illustrates a bridge pillar supported by a TLP, and is a proposed crossing of Halsafjorden.

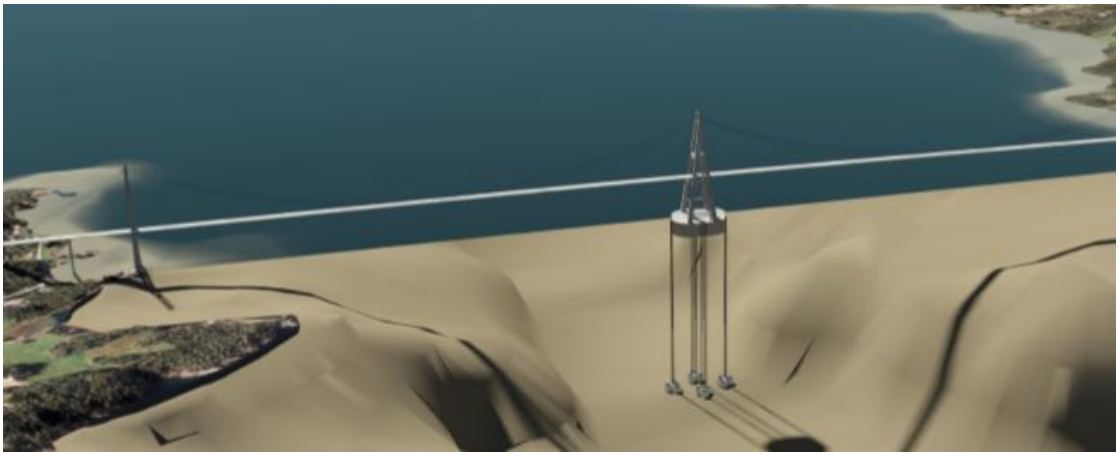

Figure 13: TLP as bridge supporting[23]

1.5 Bjørnafjorden

Bjørnafjorden is located south of Bergen, as seen in figure 14.

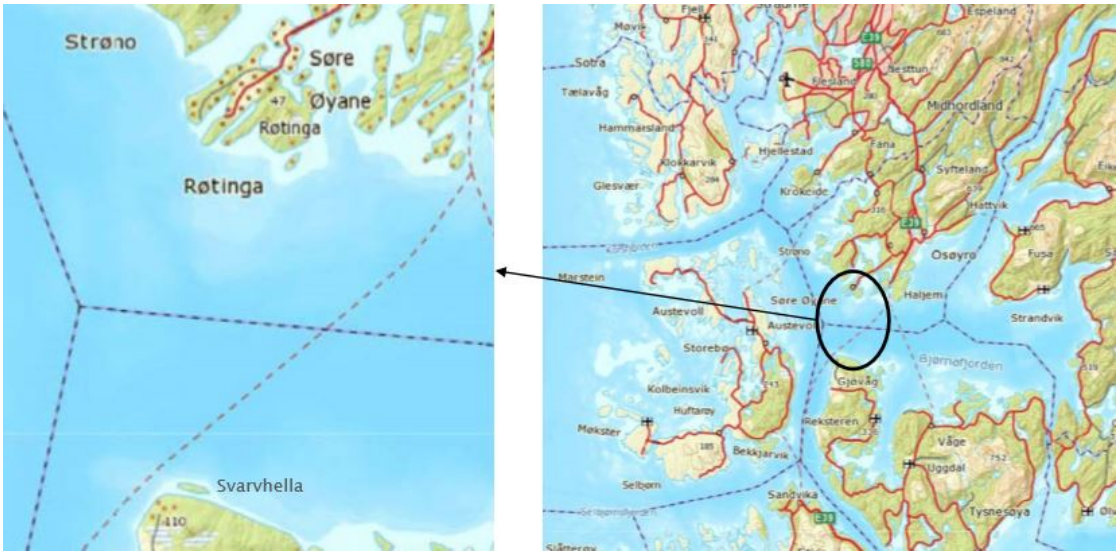

Figure 14: Bjørnafjorden[20]

Three concepts have been considered for this crossing, a submerged floating tunnel, a suspension bridge and a floating bridge[3]. One of the concepts is a multi-span suspension bridge supported by two TLPs as seen in figure 15. In this thesis, a

simplified model of this proposed concept is utilized to illustrate static and dynamic analyses.

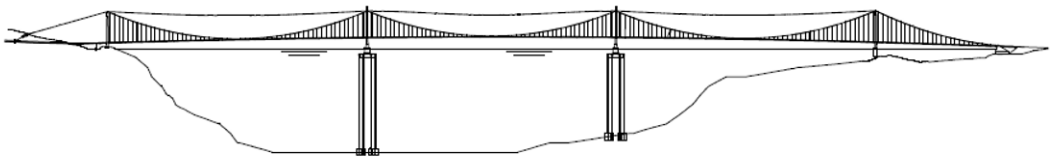

Figure 15: Bjørnafjorden Bridge with modifications[24]

The width of Bjørnafjorden is more than 5000 metres and the depth is 550 metres at the deepest[24]. The main dimensions for the proposed crossing are given in table 1.

Table 1: Main dimensions to the suspension bridge[24]

Item		Size
Span length	[m]	1385 + 1325 + 1385
Total length	[m]	> 5000
Fjord depth	[m]	550
Length of tethers to TLP1	[m]	500
Length of tethers to TLP2	[m]	400
Bridge girder width	[m]	30.6
Bridge deck height	[m]	3.92

2 Theory

Loads acting on a floating structure can be divided into functional loads, environmental loads, accidental functional loads, deformation loads, and if the floating bridge has mooring, mooring forces are included. Functional load is dead and live load, which is the weight of the structure and weight of equipment respectively[25]. Environmental load is forces due to wind, wave, current, ice and earthquake[26], where wind and waves are the major contributor[2]. Further, snow, temperature, current, tidal and the effects of marine growth, corrosion and friction, seaquake, and tsunami should be considered[13]. Accidental functional loads are forces due to explosion and fire, collision and dropped objects, while deformation loads are due to thermal load[25]. Figure 16 illustrates how current, traffic, wave and wind can act on a floating bridge.

Figure 16: Loads on Lacey V. Murrow Memorial Bridge and Homer M. Hadley Bridge[27]

A floating bridge must be comfortable and safe to use during a normal storm, i.e. environmental loads with 1-year return period. In addition, undesirable structural effects should be avoided when the bridge is exposed for environmental loads with a return period of 100-years[2]. In this thesis, current, wave and wind, is applied on the model, in addition to traffic. And in this chapter, the theory behind the estimation and calculation of these loads are explained.

2.1 Current load

The current is vital for mainly five reasons. It can cause large steady state excursions and slow drift motions of moored platforms. Secondly, it can give rise to drag and lift forces on submerged structures. Current can also give rise to vortex induced vibrations of slender structural elements and vortex induced motions of large volume structures. Finally, an interaction between strong currents and waves will lead to change in wave height and wave period, and currents can create seabed scouring around bottom mounted structures[28]. Hence, the effect of current must be considered when designing ships and offshore structures. The current is applied as a concentrated force acting on the floaters, and is estimated by equation 2.1[29].

$$F_{current} = \frac{1}{2} \cdot \rho \cdot C_d \cdot A \cdot v_c^2 \tag{2.1}$$

Where ρ is the sea density, C_d is the drag coefficient, A is the projected area of the floater, and v_c is the current velocity. The current velocity varies in space and time, where the time-dependence is due to flow fluctuation caused by turbulence[28]. The current velocity vector, $\mathbf{v}_c$, is given by equation 2.2.

$$\mathbf{v}_c = \mathbf{v}_c\,(x, y, z; t) \tag{2.2}$$

Total current velocity at location (x,y) should be taken as equation 2.2, mean-

ing, total current velocity is the sum of each current contributor, such as wind, $\mathbf{v}_{c,wind}(\mathbf{z})$, tidal, $\mathbf{v}_{c,tide}(\mathbf{z})$ and circulation, $\mathbf{v}_{c,circ}(\mathbf{z})$ and so on.

$$\mathbf{v}_c(\mathbf{z}) = \mathbf{v}_{c,wind}(\mathbf{z}) + \mathbf{v}_{c,tide}(\mathbf{z}) + \mathbf{v}_{c,circ}(\mathbf{z}) + \dots \tag{2.3}$$

The tidal components is assumed to be given as equation 2.4 where d is the water depth to still water level, and z is the distance from still water level, and is positive upwards[28]. The exponent α typically has a value of 1/7.

$$v_{c,tide}(z) = v_{c,tide}(0)\left(\frac{d+z}{d}\right)^{\alpha} \quad \text{for} \quad z \leq 0 \tag{2.4}$$

The wind velocity can be estimated from equation 2.5 or equation 2.6 when it has a slab profile[28]. The parameter d_0 is the reference depth for wind generated current, and can be set to 50 metre[28].

$$v_{c,wind}(z) = v_{c,wind}(0)\left(\frac{d_0+z}{d_0}\right) \quad \text{for} \quad -d_0 \leq z \leq 0 \tag{2.5}$$

$$v_{c,wind}(z) = v_{c,wind}(0) \quad \text{for} \quad -d_0 \leq z \leq 0 \tag{2.6}$$

The profiles which gives the highest loads for the specific application, should be applied. The wind generated current is assumed to vanish at a distance below still water. In deep water along an open coastline, the wind-generated current velocities at the still-water level can be simplified to equation 2.7.

$$v_{c,wind}(0) = k \cdot U_{1hour,10min} \quad \text{where} \quad k = 0.015\text{–}0.03 \tag{2.7}$$

Finally, the wind generated current is given by equation 2.8.

$$v_{c,wind}(z) = k \cdot U_{1hour,10min} \left(\frac{d_0 + z}{d_0} \right) \quad \text{for} \quad -d_0 \leq z \leq 0 \tag{2.8}$$

2.2 Traffic load

The traffic load can be estimated from rules and regulation given in Eurocode 1[30], and this procedure is described in this section. The width to the carriageway, w, is the distance between kerbs, or between the inner limits of vehicle restraint systems, which is seen in figure 17. The distance between the inner limits of vehicle restraint systems and kerbs of central reservation, are not included in the carriageway width.

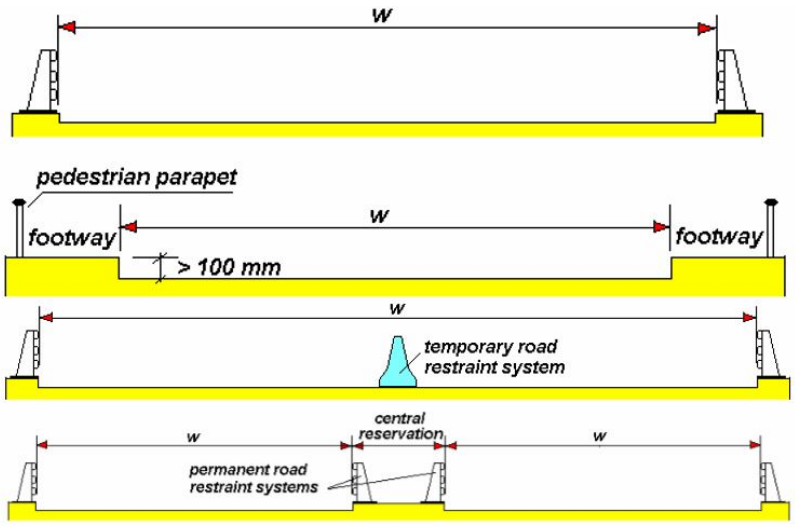

Figure 17: Carriageway width w[31]

The carriageway are divided into notional lanes, where the definition of the width to each notional lane, w_l and greatest possible integer number of such lanes, n_l, are given in figure 18 and illustrated in figure 19. In the latter figure, number 1, 2, 3 and 4 represent notional lane number 1, 2, and 3, and the remaining area,

respectively. The lane that gives the most unfavourable effect is numbered as 1, the second most unfavourable effect as 2, and so on.

Carriageway width w	**Number of notional lanes**	**Width of a notional lane** w_l	**Width of the remaining area**
$w < 5{,}4$ m	$n_1 = 1$	3 m	w - 3 m
5,4 m $\leq w < 6$ m	$n_1 = 2$	$\frac{w}{2}$	0
6 m $\leq w$	$n_1 = Int\left(\frac{w}{3}\right)$	3 m	$w - 3 \times n_1$
NOTE For example, for a carriageway width equal to 11m, $n_1 = Int\left(\frac{w}{3}\right) = 3$, and the width of the remaining area is 11 - 3×3 = 2m.			

Figure 18: Number and width of notional lanes[30]

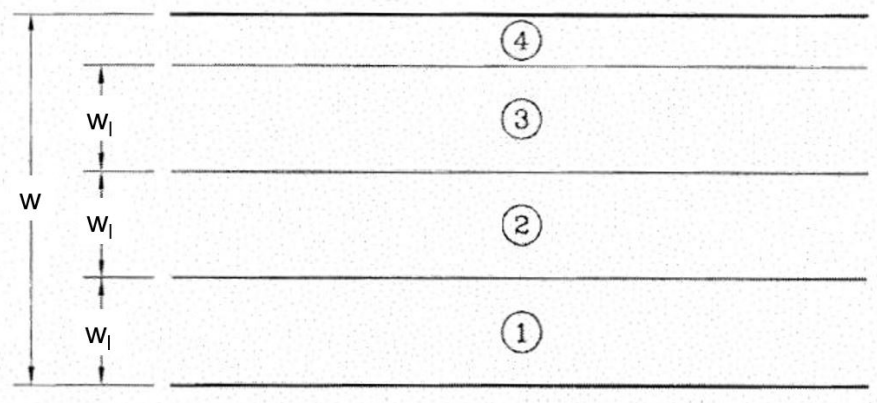

Figure 19: The carriageway width divided into notional lanes and remaining area, with modification[30]

The concentrated load, Q_i, and uniformly distributed load, q_i, for notional lane number i, and load magnitude for the remaining area, $q_{remaining}$, are estimated as

$$Q_i = \alpha_{Qi} Q_{ik}$$

$$q_i = \alpha_{qi} q_{ik}$$

$$q_{remaining} = \alpha_{qr} q_{rk}$$

Where α_{Qi}, α_{qi} and α_{qr} are adjustment factors. Examples of α-factors are given in figure 20 for two classes, 1^{st} class and 2^{nd} class, where the former means international heavy vehicle traffic and the latter, normal heavy vehicle traffic.

Classes	α_{Q1}	α_{Qi} $i \geq 2$	α_{q1}	α_{qi} $i \geq 2$	α_{qr}
1st class	1	1	1	1	1
2nd class	0,9	0,8	0,7	1	1

Figure 20: Example for α-factors[31]

The characteristic values for Q_{ik}, q_{ik} and q_{rk} are given in figure 21.

Location	Tandem system *TS*	*UDL* system
	Axle loads Q_{ik} (kN)	AC1 q_{ik} (or q_{rk}) (kN/m^2) AC1
Lane Number 1	300	9
Lane Number 2	200	2,5
Lane Number 3	100	2,5
Other lanes	0	2,5
Remaining area (q_{rk})	0	2,5

Figure 21: Characteristic loads[30]

2.3 Linear wave theory

When estimating the dynamic wave load, potential theory is assumed valid. By applying potential theory, the sea water is assumed to be incompressible and in-

viscid, and the fluid motion is irrotational[32][33]. Incompressible sea water means that the water has nearly a constant density throughout, hence, small viscous effects can be neglected, and the fluid is assumed to be inviscid[34]. Irrotational fluid motion means that the fluid particles do not rotate[34]. Further, it is assumed that the waves are linear since an analysis for irregular sea is more complex compared to for regular waves. It is adequate to perform an analysis for a structure in regular sinusoidal waves, and by a linearly superposing for small wave components, the results can be viewed as if they were obtained from an analysis in irregular sea[32].

The deriving of equations presented in this section are given in appendix A. The velocity potential, ϕ, for infinite water depth with propagating regular sinusoidal waves with frequency ω and amplitude ζ_a, is given by equation 2.9.

$$\phi = \frac{g\zeta_a}{\omega} e^{kz} \cos(\omega t - kx) \tag{2.9}$$

Where z is the water depth. Equation 2.10 gives the relation between the wave number k, acceleration due to gravity, g, and the wave frequency.

$$\omega^2 = kg \tag{2.10}$$

For finite water depth and regular sinusoidal propagating wave, the velocity potential and the relation between the wave number and wave frequency, are given by equation 2.11 and 2.12, respectively, where h is the water depth.

$$\phi = \frac{g\zeta_a}{\omega} \frac{\cosh k(z+h)}{\cosh(kh)} \cos(\omega t - kx) \tag{2.11}$$

$$\omega^2 = kg \tanh(kh) \tag{2.12}$$

For both infinite and finite water depth, the wave period, T, is given by equation 2.13.

$$T = \frac{2\pi}{\omega} \tag{2.13}$$

To define whether the water depth as infinite or finite, table 2 can be used as a reference where h is the water depth and λ is the wavelength.

Table 2: Limits for water depths[35]

Shallow water	Intermediate water	Deep water
$h/\lambda < 1/25$	$1/25 < h/\lambda < 1/2$	$h/\lambda > 1/2$

2.4 Response in regular waves

The response for irregular sea could be estimated by performing an analysis for regular waves and then by linear superposing, the response can be viewed as if it was found through an analysis for irregular waves. To be able to do this simplification, steady-state must be assumed so there are no transient effects presents due to the initial condition[32]. When transient effects are neglected, linear dynamic motions and loads on the structure are harmonically oscillating with the same frequency, ω_i, as the wave loads[32].

To estimate total hydrodynamic forces, two assumptions are made. First, it is assumed that the structure is restrained, thus it cannot oscillate with the same frequency as incoming waves, ω_i. Second it is assumed that the structure is forced to oscillate with frequency ω_i when there is no incident regular waves[32][33]. For

the first assumption, the wave excitation loads can be found, which consists of Froude-Krilov and diffraction forces and moments. For the second assumption, the hydrodynamic loads are estimated, which consist of the added mass, damping, and restoring problem. By summarizing these two, total hydrodynamic forces are obtained[32], which is illustrated in figure 22.

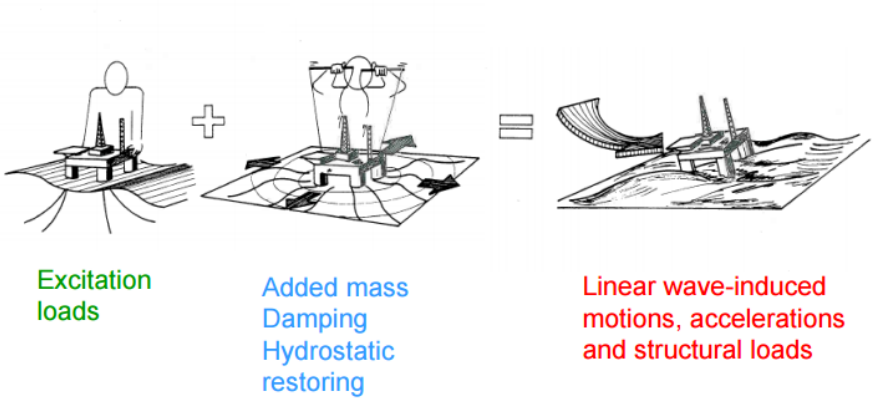

Figure 22: Superposition of excitation loads and hydrodynamic loads to estimate the hydrodynamic problem[32]

2.4.1 Froude-Krilov and diffraction forces

Forces obtained from the first assumption are divided into Froude-Krilov forces and diffraction forces, given by equation 2.14. The first term explains how the pressure from the incoming wave will act on the body, while the second term explains how the pressure field will change due to the inserted body.

$$F_i = F_{FK,i} + F_{diff,i} = -\iint_S p\mathbf{n_i} dS + A_{i1}a_x + A_{i2}a_y + A_{i3}a_z \qquad i = 1,2,3 \quad (2.14)$$

Froude-Krilov forces is obtained by integrating the pressure from the incoming waves, p, over the wet surface, S, seen in equation 2.15.

$$F_{FK,i} = -\iint_S p\mathbf{n_i} dS \qquad i = 1, 2, 3 \tag{2.15}$$

Where $\mathbf{n_i}$ is the unit vector normal to the body surface and positive into the fluid[32]. The sea pressure acting on the body is given by equation 2.16.

$$p = -\rho\frac{\delta\phi}{\delta t} = \rho g\zeta_a e^{kz}\sin(\omega t - kx) \tag{2.16}$$

By inserting equation 2.16 in equation 2.15, the Froude-Krilov force can be estimated.

$$F_{FK,i} = \rho g\zeta_a \iint_S e^{-kz}\cos(\omega t - kx)\mathbf{n_i} dS \tag{2.17}$$

The body cause changes in the pressure field resulting in diffraction forces, given by equation 2.18.

$$F_{diff,i} = A_{i1}a_x + A_{i2}a_y + A_{i3}a_z = m_{added,i} \cdot a_i \qquad i = 1, 2, 3 \tag{2.18}$$

Where $m_{added,i}$ is added mass in x-, y- and z-direction. For a three-dimensional body the added mass is given as

$$m_{added,i} = \rho C_{a,i} V_R \tag{2.19}$$

Where ρ is the sea density, $C_{a,i}$ is added mass coefficient and V_R is the reference

volume. For a two-dimensional body, the added mass is given by equation 2.20 where A_s is the cross-sectional area.

$$m_{added,i} = \rho C_{a,i} A_s \tag{2.20}$$

The added mass coefficient is dependent of the structures shape and it is given in different tables. The acceleration in x-, y- and z- direction for deep sea, is given as

$$a_x = \frac{\delta^2 \phi}{\delta x \delta t}$$

$$a_y = \frac{\delta^2 \phi}{\delta y \delta t}$$

$$a_z = \frac{\delta^2 \phi}{\delta z \delta t}$$

Thus, horizontal and vertical diffraction force is given by equation 2.21 and 2.22 respectively.

$$F_{diff,1} = \rho C_{a,1} V_R \omega^2 \zeta_a e^{-kz} \cos(\omega t - kx) \tag{2.21}$$

$$F_{diff,3} = -\rho C_{a,3} V_R \omega^2 \zeta_a e^{-kz} \sin(\omega t - kx) \tag{2.22}$$

2.4.2 Added mass, damping and restoring forces

Assuming that the body is forced to move with frequency ω_i and there is no incoming waves. A floating structure has six degrees of freedom which is shown in figure 23.

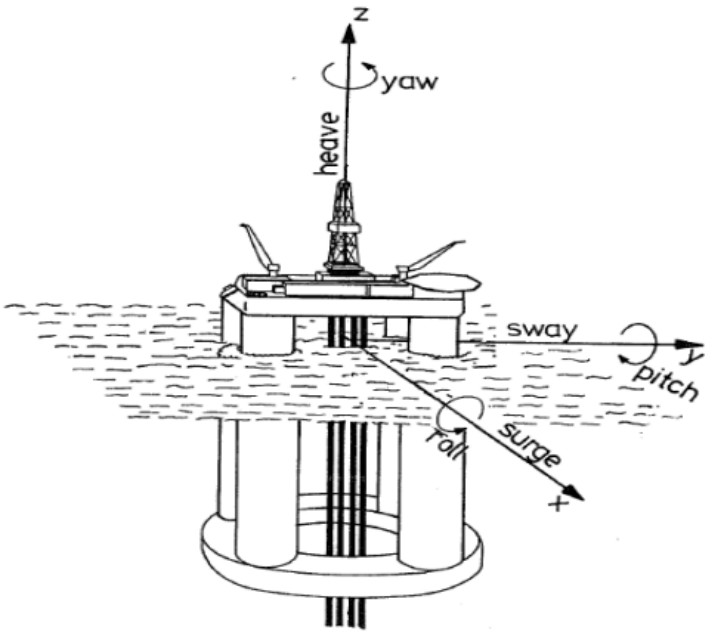

Figure 23: Degrees of freedom for a floating structure[32]

There are three translatory motions and three rotational motions, where surge, η_1, sway, η_2 and heave, η_3 are translatory motions while roll, η_4, pitch, η_5 and yaw, η_6 are rotational motions[32]. Since the body is forced to oscillate, there will be oscillating pressure on the body surface[32], where forces on the body surface is given by equation 2.23. F_1, F_2 and F_3 are forces in x-, y- and z-direction.

$$\mathbf{F} = F_1\mathbf{i} + F_2\mathbf{j} + F_3\mathbf{k} \tag{2.23}$$

By defining the moments as F_4, F_5 and F_6[32], added mass and damping is given by equation 2.24[32].

$$F_i = -A_{i,j}\ddot{\eta}_j - B_{i,j}\dot{\eta}_j \tag{2.24}$$

Where $A_{i,j}$ is added mass in i-direction caused by acceleration in j-direction, $\ddot{\eta}_j$, and $B_{i,j}$ is damping in i-direction caused by velocity in j-direction, $\dot{\eta}_j$. When the body is forced to oscillate with frequency ω_i and an amplitude equal to 1, the added mass is defined as the part of the force that acts from the water to the structure and is in antiphase with the acceleration[33], while damping is the part of the force that is in antiphase with the velocity[33]. Added mass and damping are functions of body shape, frequency of oscillation and forward speed[32].

Restoring force is defined as the force that tries to get the system back to equilibrium[33], and is given by equation 2.25.

$$F_i = -C_{i,j}\eta_j \tag{2.25}$$

Thus, the force occurring when the body is forced to oscillate, is given by equation 2.26.

$$F_i = -A_{i,j}\ddot{\eta}_j - B_{i,j}\dot{\eta}_j - C_{i,j}\eta_j \qquad i,j = 1,2,...,6 \tag{2.26}$$

2.5 Wind load

To determine the wind load, rules and regulations given by DNV[28] are utilized. The wind force acting normal to members or surfaces, is given by equation 2.27 where C is a shape factor and S is projected area of the member normal to the direction of the force.

$$F_{wind} = C \cdot q \cdot S \cdot \sin(\alpha) = C \cdot q \cdot S \tag{2.27}$$

α is the angle between the direction of the wind and the axis of the exposed member or surface, and the most unfavourable wind direction is when $\sin(\alpha) = 1$. The wind pressure, q, is given by equation 2.28 where ρ_a is the mass density of air and $U_{T,z}$ is the wind velocity averaged over a time interval T at a height z metre above the mean water level or onshore ground.

$$q = \frac{1}{2}\rho_a U_{T,z}^2 \tag{2.28}$$

The wind speed varies with time and height above either the ground or the sea surface. The 10-minute mean wind speed with return period, T_R, is expressed by equation 2.29.

$$U_{10,T_R} = F^{-1}_{U_{10,max},1year}\left(1 - \frac{1}{T_R}\right) \quad \text{for} \quad T_R > 1year \tag{2.29}$$

Where the annual maximum of the 10-minutes mean wind speed, $U_{10,max}$ is assumed to be Gumbel distributed, and can be expressed as equation 2.30 with the site- and height-dependent distribution parameters a and b.

$$F_{U_{10,max},1year}(u) = \exp\{-\exp\left[-a(u-b)\right]\} \tag{2.30}$$

2.6 Tension leg platform

A TLP can be considered as a buoyant unit connected to the seabed by pre-tensioned tethers[36]. The tethers are in pre-tension since the platforms buoyancy is larger than its weight[32]. The tether tension force, T_n, for tether n is given by equation 2.31 where B and W is the buoyance and weight of the platform.

$$\sum_{n=1}^{N} T_n = B - W \tag{2.31}$$

The TLP is restricted to move in heave, roll and pitch[36]. Total stiffness, K_p, is given by equation 2.32 where K^C is conventional axial stiffness, C is the platform hydrostatic stiffness with influence of tethers included, and K^G is geometrical stiffness[37].

$$K_p = K^C + C + K^G \tag{2.32}$$

By neglecting the vertical displacement of the floater, also known as setdown, linear stiffness is assumed. The different stiffness term act on the floater as is seen in figure 24.

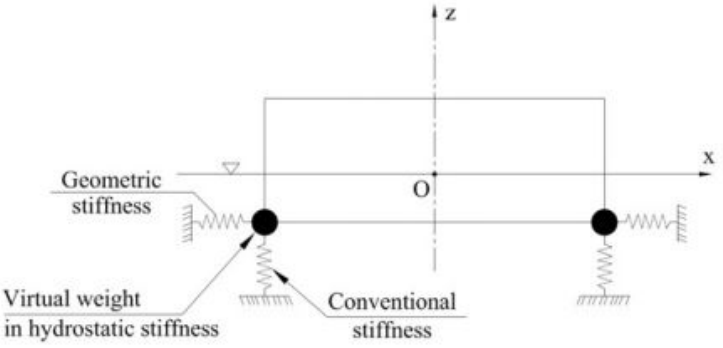

Figure 24: Stiffness contribution of TLP[37]

Conventional stiffness

The tethers are built in steel, and its bending stiffness is negligibly small. Heave, roll and pitch will have an influence on the tethers. The stiffness is the relation between vertical force and displacement, and between moment and angle of rotation[37]. The conventional stiffness are given in equation 2.33 where k_{33}^c, k_{44}^c and k_{55}^c is stiffness due to heave, roll and pitch, respectively.

$$\begin{aligned} k_{33}^C &= \frac{EA}{L} \\ k_{44}^C &= \frac{EI_x}{L} \\ k_{66}^C &= \frac{EI_y}{L} \end{aligned} \tag{2.33}$$

E, A, L, I_x and I_y is the Young's modulus, cross-section, length, and moments of inertia about x-axis and y-axis to all tethers, respectively.

Hydrostatic stiffness

The hydrostatic stiffness are given by equation 2.34 where C_{33}, C_{44} and C_{55} is the hydrostatic stiffness coefficients in heave, roll and pitch.

$$\begin{aligned} C_{33} &= \rho g A_{wp} \\ C_{44} &= \rho g I_{wpx} + B z_B – W z_G - \sum_{n=1}^{N} T_n z_t \\ C_{55} &= \rho g I_{wpy} + B z_B – W z_G - \sum_{n=1}^{N} T_n z_t \end{aligned} \tag{2.34}$$

Where A_{wp}, I_{wpx} and I_{wpy} is the waterplane area and its moment of inertia, respectively. The vertical coordinates z_B, z_G and z_t are the distance from buoyancy centre, gravity centre and tether top, to the waterplane.

Geometric stiffness

As mentioned, the TLP is compliant in surge, sway, and yaw, and the geometric stiffness are given in equation 2.35, where k_{11}^G, k_{22}^G and k_{66}^G are the geometric stiffness in surge, sway and yaw[37].

$$\begin{aligned} K_{11}^G &= \sum_{n=1}^{N} \frac{T_n}{L} \\ K_{22}^G &= \sum_{n=1}^{N} \frac{T_n}{L} \\ K_{66}^G &= \sum_{n=1}^{N} \frac{T_n \left(x_n^2 + y_n^2\right)}{L} \end{aligned} \tag{2.35}$$

Since the TLP modelled is assumed to be circular, the distance from the midpoint of the floater in x- and y-direction will be equal, x_n and y_n is equal to the radius to the TLP.

Total stiffness

Summarising the conventional, hydrostatic, and geometric stiffness, the total translational stiffness is given by equation 2.36.

$$
\begin{aligned}
K_{11} &= \sum_{n=1}^{N} \frac{T_n}{L} \\
K_{22} &= \sum_{n=1}^{N} \frac{T_n}{L} \\
K_{33} &= \rho g A_{wp} + \frac{EA}{L}
\end{aligned}
\tag{2.36}
$$

Morison's equation

Horizontal force per unit length on a strip, dF is given by equation 2.37 where C_d and C_m are drag- and mass coefficients, D and A are the diameter and cross-section to the floater, and u and $\dot{u}$ are the fluid velocity and fluid acceleration[32].

$$
dF = \frac{1}{2}\rho C_d D u|u| + \rho C_m A \dot{u} \tag{2.37}
$$

By integrating equation 2.37 over the draught z, Morison's equation is written as equation 2.38.

$$
F = \frac{1}{2}\rho C_d D u|u|z + \rho C_m A \dot{u} z \tag{2.38}
$$

3 Analysis

Analyses are executed on a floating bridge to study its behaviour during its lifetime. A floating bridge should be comfortable during a normal storm, meaning for environmental loads with a 1-year return period. In addition, undesirable structural effects should be avoided for an extreme storm, meaning for 100-year return period[2]. To ensure that the floating bridge is safe and its design is applicable, these analyses are performed. In this chapter, the procedure for eigenvalue analysis, static analysis and dynamic analysis are described.

3.1 Eigenvalue analysis

An eigenvalue analysis is executed to avoid resonance, meaning the eigenfrequency of the model is equal or close to the frequency of the incoming wave. In addition, this analysis is performed in this thesis to ensure similar stiffness and mass of the models as Bjørnafjorden Bridge. To solve the eigenvalue problem, eigenfrequency and its modeshape are calculated[38]. The classical eigenvalue problem is given by equation 3.1 where $\mathbf{M}$ is the mass-matrix, $\mathbf{C}$ is damping-matrix, $\mathbf{K}$ is the stiffness-matrix, $\mathbf{F}(t)$ is the force acting on the structure, $\ddot{\mathbf{r}}$ is the acceleration, $\dot{\mathbf{r}}$ is the velocity while $\mathbf{r}$ is the displacement.

$$\mathbf{M}\ddot{\mathbf{r}} + \mathbf{C}\dot{\mathbf{r}} + \mathbf{K}\mathbf{r} = \mathbf{F}(t) \tag{3.1}$$

Since the mass and damping matrices are non-linear functions of the frequency, the eigenvalue becomes non-linear and must be solved in an iterative manner. By assuming no damping and the structure are oscillating freely, the equation of motion can be simplified and is given by equation 3.2.

$$\mathbf{M}\ddot{\mathbf{r}} + \mathbf{K}\mathbf{r} = 0 \tag{3.2}$$

By assuming a harmonic oscillation with frequency ω, the displacement and acceleration is given as

$$\mathbf{r} = \phi \sin(\omega t)$$
$$\ddot{\mathbf{r}} = -\phi\omega^2 \sin(\omega t)$$

where ϕ is the eigenvector. By inserting the equations for acceleration and displacement into equation 3.2, the eigenvalue problem on general form is obtained, see equation 3.3.

$$\left(\mathbf{K} - \omega^2\mathbf{M}\right)\phi = 0 \tag{3.3}$$

To obtain other eigenvalues, a shift μ can be introduced. Then, the eigenvalue λ is given by equation 3.4, which says that the eigenvalue will converge to the eigenvalue closest to the introduced shift. The deviation of equation 3.4 is given in appendix B.

$$\lambda_i = \mu + \bar{\lambda_i} = \mu + \frac{\mathbf{z}_k^T\mathbf{M}\mathbf{z}_{k-1}}{\mathbf{z}_k^T\mathbf{M}\mathbf{z}_k} \tag{3.4}$$

3.2 Static analysis

A static analysis, is an analysis independent of time, meaning that the load applied is constant throughout time. Assuming a floating bridge can be simplified to a beam, static load can be calculated by using classical beam theory. When a con-

centrated load P is applied to the system, maximum shear force, V_{max}, maximum moment, M_{max}, and maximum deflection, y_{max} can be found by using equation 3.5, 3.6 and 3.7, respectively[2].

$$V_{max} = \frac{P}{2} \tag{3.5}$$

$$M_{max} = \frac{P}{4\lambda} \tag{3.6}$$

$$y_{max} = \frac{P\lambda}{2k} \tag{3.7}$$

Where k is the modulus of foundation and the stiffness ratio λ is given as equation 3.8.

$$\lambda = 4\sqrt{\frac{k}{4EI}} \tag{3.8}$$

3.3 Dynamic analysis

When introducing the response due to wind and waves, the response analysis is more complex because of the random nature of these environmental loads [2]. To be able to calculate these responses more realistic, it should be done by a dynamic analysis. The dynamic response analysis is achieved by solving the equation of motion, given by equation 3.9.

$$\mathbf{M\ddot{r}} + \mathbf{C\dot{r}} + \mathbf{Kr} = \mathbf{F}(t) \tag{3.9}$$

$\mathbf{M}$, $\mathbf{C}$ and $\mathbf{K}$ are the mass-inertia matrix, damping matrix and damping coefficients respectively, and $\ddot{\mathbf{r}}$, $\dot{\mathbf{r}}$ and $\mathbf{r}$ are the generalized acceleration, velocity and displacement at each degree of freedom. The effects of incoming waves are included in the equation of motion by introducing hydrodynamic effects characterized in terms of added mass and damping coefficients. For a floating structure, the equation of motion is given by equation 3.10 where the mass-term, damping-term and restoring-term are increased since added mass, $\mathbf{A}$, hydrodynamic damping coefficient $\mathbf{C_2}$, and hydrostatic restoring force, $\mathbf{k}$, are added.

$$(\mathbf{M} + \mathbf{A})\,\ddot{\mathbf{r}} + (\mathbf{C} + \mathbf{C_2})\,\dot{\mathbf{r}} + (\mathbf{K} + \mathbf{k})\,\mathbf{r} = \mathbf{F}(t) \tag{3.10}$$

The structural damping is an important contributor of damping in the structure, and a structural coefficient of 2-5 % of critical damping can generally be assumed in the analysis. Equation 3.10 is either solved in time-domain or frequency-domain analysis[2]. It will be efficient to utilize the frequency-domain approach and time-consuming and complex to utilize the time-domain approach since the coefficients are frequency-dependent. Nevertheless, the analysis must be executed in time-domain because frequency-domain is only applicable for linear system[39]

3.3.1 Time-domain analysis

When solving for time-domain, the most common approaches for very large floating structures is either by utilizing the direct time integration method or Fourier transform[39]. For the first method, the equation of motion is discretized for both the structure and for the fluid domain, while for the method including Fourier transform, the frequency-domain solutions are first obtained for the fluid domain. By utilizing Fourier transform, the results are transformed into differential equations for elastic motions. Finally, the equations can be solved directly in the time-domain, either by finite element method or other suitable computational methods.

3.4 Non-linear analysis

Theory in this section is based on Finite Element Modelling and Analysis of Marine Structures written by T. Moan[40]. Linear theory is based on three main principles which are equilibrium, kinematic compatibility, and stress-strain relationship. Further, small displacement and linear and elastic material is assumed. These assumptions must be modified when, i.e. ultimate strength is considered. In non-linear theory, the stiffness $\mathbf{K}$ dependency of displacement $\mathbf{r}$ is seen in equation 3.11 where $\mathbf{R}$ is external load.

$$\mathbf{K_I}\,(\mathbf{r})d\mathbf{r} = d\mathbf{R} \tag{3.11}$$

Three solution techniques for non-linear problems are described in this section. These are load incremental procedures, iterative procedures, and a combination.

3.4.1 Load incremental method − Euler-Cauchy method

The external load is applied stepwise where the displacement incremental is determined by equation 3.11. By adding the displacement increment, total displacement is obtained. The incremental stiffness matrix $\mathbf{K_I}$, is calculated by utilizing the known displacement and stress condition, and is kept constant during the load increment. The procedure is shown for step number $m+1$ in equation 3.12 where the initial condition $\mathbf{r}_0$ is equal to zero.

$$\begin{aligned}
\Delta\mathbf{R}_{m+1} &= \mathbf{R}_{m+1} - \mathbf{R}_m, \\
\Delta\mathbf{r}_{m+1} &= \mathbf{K_I}(\mathbf{r}_m)^{-1}\Delta\mathbf{R}_{m+1}, \\
\mathbf{r}_{m+1} &= \mathbf{r}_m + \Delta\mathbf{r}_{m+1}
\end{aligned} \tag{3.12}$$

In figure 25, the Euler-Cauchy method and the true variation for a single degree of freedom system is compared where the deviation is equal $\mathbf{K}(\mathbf{r})\mathbf{r} = \mathbf{R}$. The gap

occurs since the method don't fulfil the total equilibrium equation and to mitigate the error, the load increment can be reduced or adjusted according to the degree on non-linearity.

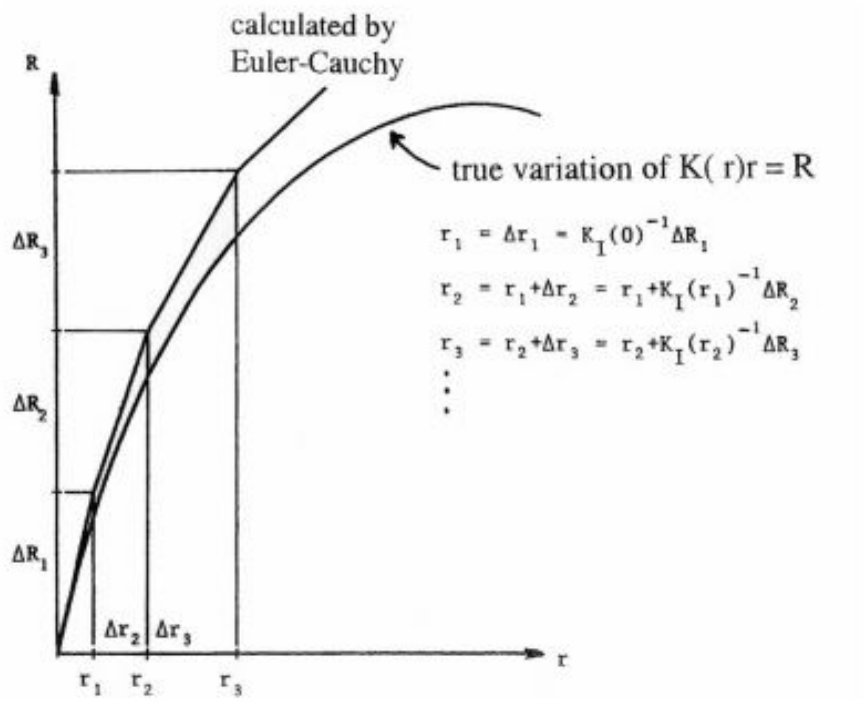

Figure 25: The Euler-Cauchy incremental method[40]

3.4.2 Iterative method – Newton-Raphson method

The most common iterative method, is the Newton-Raphson method[41], and its algorithm to solve x for the problem $f(x) = 0$ is given by equation 3.13 where $f'(x_n)$ is the derivative of $f(x)$ with respect to x at $x = x_n$.

$$x_{n+1} = x_n - \frac{f(x_n)}{f'(x_n)} \tag{3.13}$$

If $\mathbf{R}$ and $\mathbf{R_{int}}$ are known and $\mathbf{K}_I(\mathbf{r})$ is established, $\Delta\mathbf{r}_{m+1}$ is solved by equation

3.14 for each step and then $\mathbf{r}_{m+1}$ is determined by equation 3.15.

$$\mathbf{R} - \mathbf{R_{int}} = \mathbf{K_{I(n)}} \Delta \mathbf{r_{m+1}} \tag{3.14}$$

$$\mathbf{r}_{m+1} = \mathbf{r}_m + \mathbf{K}_I^{-1}(\mathbf{r}_m)\,(\mathbf{R_{int}} - \mathbf{R}) \tag{3.15}$$

The procedure is described in figure 26 for a single degree of freedom system.

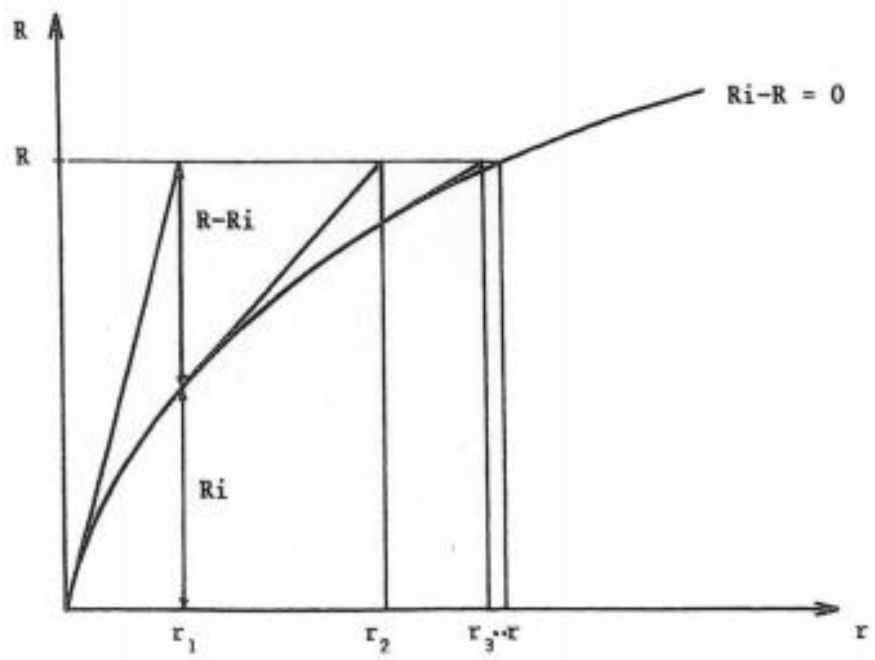

Figure 26: The Newton-Raphson iterative method[40]

Since the incremental stiffness and displacement are determined for each iteration step, the procedure is time-consuming. The modified Newton-Raphson method update the incremental stiffness less frequently which is convenient. In figure 27, two alternatives for a modified Newton-Raphson method is shown. The first is with no updates of $\mathbf{K}_I$ and the second is where $\mathbf{K}_I$ is updated after the first iteration.

Figure 27: The Newton-Raphson iterative method with no update, left, and one update, right[40]

3.4.3 Combined method

By a combined procedure, the external load is incremental applied, and for each increment, iteration achieves equilibrium. The procedure is seen in figure 28.

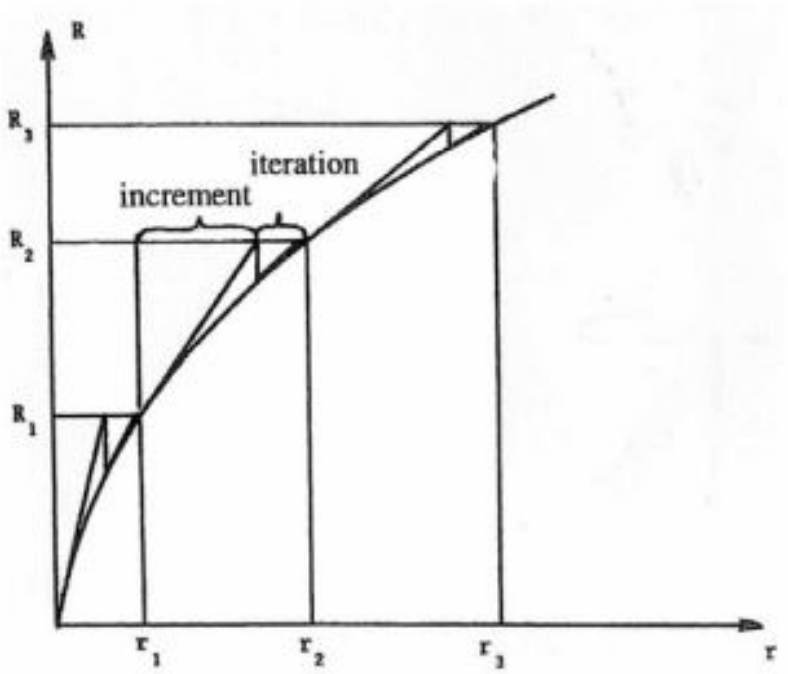

Figure 28: Combined incremental and iterative method[40]

The modified Newton-Raphson method is utilized to keep the gradient $\mathbf{K}_I$ constant during several iterations cycles.

4 Analysing tools

The analyses are executed in the hydrodynamic design tool HydroD and in Abaqus/CAE, which are briefly explained in this chapter.

4.1 HydroD and Wadam

To estimate the frequency-dependent added mass and damping, a panel model of the floater, was first built in the pre-processor GeniE. It was then imported into the hydrodynamic analysing program, Wadam, an integrated part of the SESAM system, and generated by the hydrodynamic design tool HydroD[42]. The results obtained in Wadam, can either be presented directly as complex transfer functions or converted into time-domain results[42].

4.2 Abaqus/CAE

The simplified models are created and analysed in Abaqus/CAE. Abaqus/CAE is a licence based program for finite element modelling. It is flexible since the user can step through the history of the analysis. It divides the problem history into steps and for each step, the user chooses a procedure and thereby defines the type of analysis that should be performed during the step. Any choice can be changed, and the effects of previous history are included in the response in each new step[43].

Eigenvalue problem

By neglecting the damping matrix $\mathbf{C}$ and assume symmetric stiffness matrix $\mathbf{K}$, the system has real squared eigenvalues, μ^2, and real eigenvectors[43]. In addition, by assuming positive semidefinite stiffness matrix, the eigenvalue becomes an imaginary eigenvalue, $\mu = i\omega$, and the eigenvalue problem is given as described in section 3.1

$$\left(\mathbf{K} - \omega^2 \mathbf{M}\right) \phi = 0$$

For structural eigenvalue problems, Abaqus/CAE utilize Lanczos eigensolver when the extreme eigenvalues and its belonging eigenvectors are estimated. For each step Lanczos run, the spectral transformation given by equation 4.1 is applied, where θ is the eigenvalue.

$$\mathbf{M}\left(\mathbf{K} - \mu\mathbf{M}\right)^{-1} \mathbf{M}\phi = \theta \mathbf{M}\phi \tag{4.1}$$

This transformation allows a rapidly convergence to the desired eigenvalues[43]. The eigenvalue for equation 4.1 is given by equation 4.2

$$\lambda = \omega^2 = \frac{1}{\theta} + \mu \tag{4.2}$$

Implicit dynamic analysis

The implicit method was used for solving dynamic analysis. This means that dynamic quantities for time step $t + \Delta t$ are not only solved for values at time step t, but also for values for time step $t + \Delta t$. Since they are implicit, nonlinear equations must be solved[43]. If NLGEOM, a shortened form of geometric non-linearity[44], is allowed, geometric non-linearity is accounted for.

Non-linear solution techniques

Abaqus/CAE combines incremental and iterative procedure when solving non-linear problems[45]. The simulation is divided into several load increments, and for each increment, equilibrium is estimated. To determine an acceptable solution for the given load increments, several iterations are needed and the sum of all incremental responses, is the approximated solution to the non-linear problem.

5 Simplified models and analyses procedure

In this chapter, four different models of the proposed crossing of Bjørnafjorden are described. In addition, the procedure of how to obtain added mass and damping, how the eigenmode analysis is performed and the static and dynamic loads are described.

5.1 Simplified models

The correlation between the structural response and the design of the bridge, were studied by creating four simplified models. The dimensions and design of the models were determined with inspiration from the proposed crossing of Bjørnafjorden. At an early stage of modelling, it was clear that Model 1 had some difficulties to resist the applied vertical loads, especially between the TLPs. Consequently, the vertical stiffness was changed for the other models, either by reducing span length or adjusting the cross-section. By comparing the results for Model 2, Model 3, and Model 4 to Model 1, it can be studied how the changes of the models' characteristic affect the responses.

All models have the same material properties, and it is assumed that the bridge girder and tethers are built in steel, while the floaters are built in concrete. By choosing steel, the building time and cost are reduced[1]. The material characteristics utilized, are given in table 3, where ν_{steel} is Poisson's ratio.

Table 3: Material properties

Item		Size
E	[GPa]	210
$\rho_{concrete}$	$[kg/m^3]$	2 400
ρ_{steel}	$[kg/m^3]$	7 850
ν_{steel}	[-]	0.3

The models are created by a B31 element, a two-node linear beam element in three-dimensional space[46]. The end-nodes are fixed, meaning no translational and rotational movements are allowed. The bridge girder designed by NPRA, is a closed steel box with four traffic lanes and one footpath, as seen in figure 29. The simplified cross-section is seen in figure 30, and the vertical and horizontal beams have different thickness.

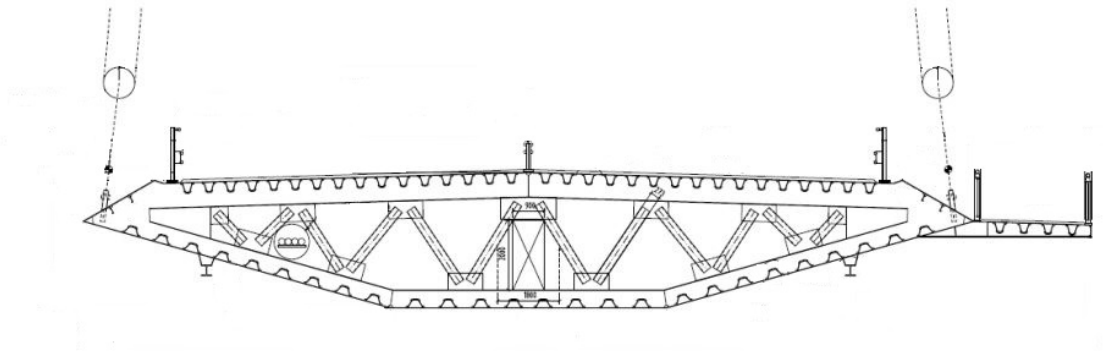

Figure 29: Bridge girder for Bjørnafjorden Bridge, with modifications[21]

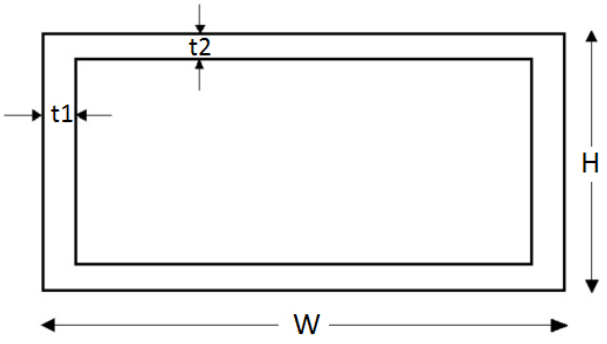

Figure 30: Cross-section for the models

5.2 Model 1, 2 and 3 – Simplified model supported by two TLPs

The first three simplified models consist of two TLPs, where the TLPs are modelled as point masses. The difference between the three first models are the cross-section characteristics, where the dimensions are given in table 4.

Table 4: Model dimensions

Item		Model 1	Model 2	Model 3
t_1	[m]	0.4	0.4	0.4
t_2	[m]	0.9	0.9	0.7
W	[m]	30.6	30.6	30.6
H	[m]	6	5	6

The applied translational stiffness was calculated from equation 2.32, where subscript 11, 22 and 33 represent displacement in x-, y- and z-direction, respectively. Since the TLPs have different length, the applied vertical and lateral stiffness for the two TLPs are different. Nevertheless, the shape of the floater is the same, so the hydrostatic stiffness is equal for the two TLPs. Table 5 gives vertical and lateral stiffness for TLP1 and TLP2, which is for water depth 550 metre and 450 metre, respectively. The calculations are given in appendix C.

Table 5: Vertical, lateral and longitudinal stiffness for TLP1 and TLP2

Stiffness		TLP1	TLP2
K_{11}	[N/m]	6.00E5	7.50E5
K_{22}	[N/m]	6.00E5	7.50E5
K_{33}	[N/m]	8.66E8	1.08E9
C_{33}	[N/m]	7.89E6	7.89E6

The tethers are applied as spring-elements, represented by the purple circle in figure 31.

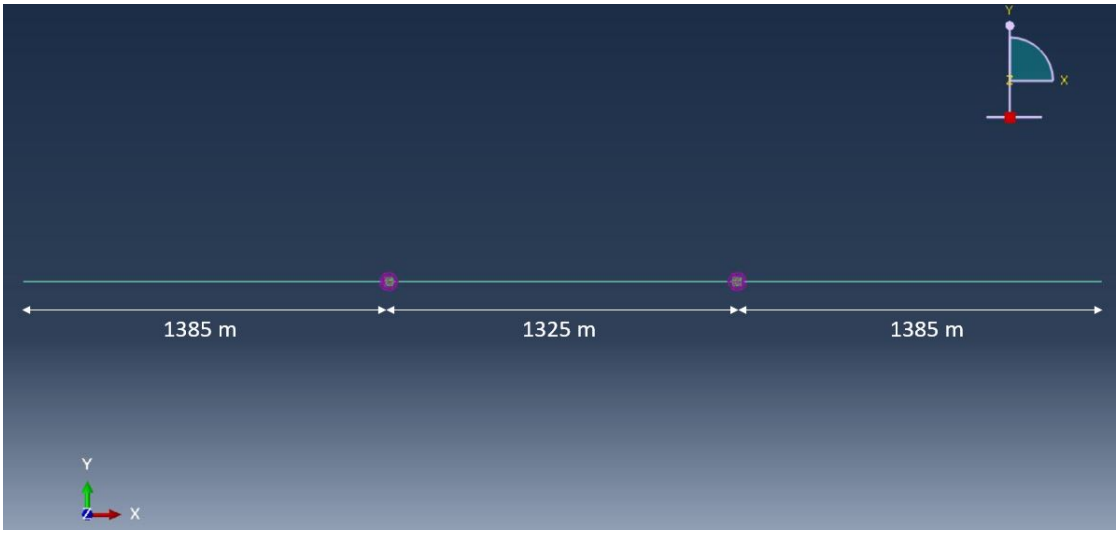

Figure 31: Simplified Model 1, Model 2 and Model 3

5.3 Model 4 – Simplified model supported by three TLPs

The fourth simplified model consist of three TLPs as illustrated in figure 32. The tethers are applied in the model as spring-elements, represented by the purple circles.

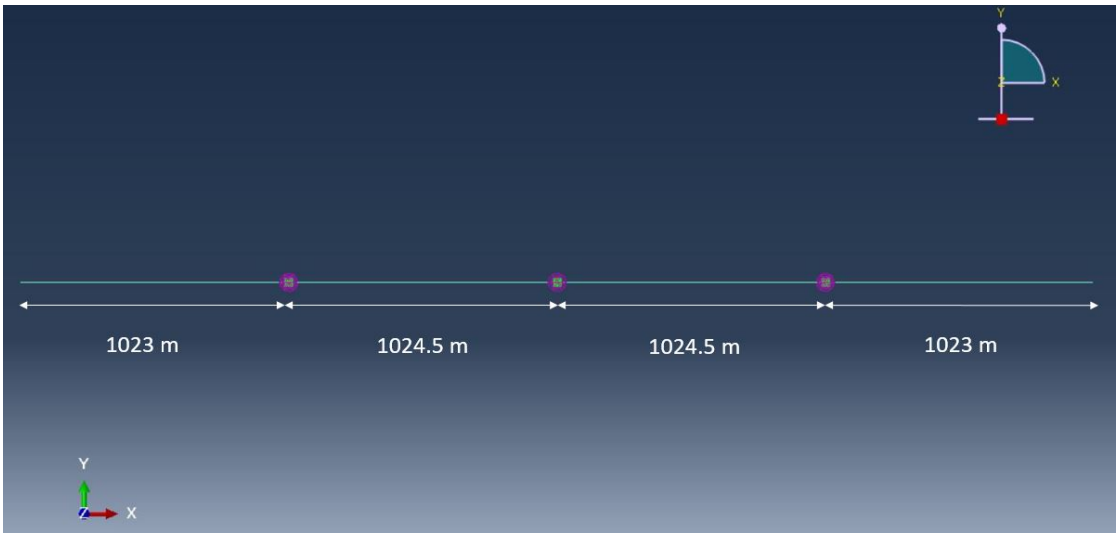

Figure 32: Simplified Model 4

The water depth for the three TLPs are estimated based on figure 15, and the values utilized when calculating the spring-elements, are given in table 6.

Table 6: Water depth for the TLPs for Model 4

TLP no.	Water depth [m]
TLP1[4]	550
TLP2[4]	550
TLP3[4]	450

Calculated vertical and lateral stiffness for the three TLPs are given in table 7. The applied stiffness for TLP1[4] is the same as for the previous models, since the water depth is the same. This is also true for the applied stiffness for TLP3[4]. The applied stiffness for TLP1[4] and the mid-TLP, TLP2[4], are equal. The calculations are given in appendix C.

Table 7: Vertical, lateral and longitudinal stiffness for the TLPs

Stiffness		TLP1[4]	TLP2[4]	TLP3[4]
K_{11}	[N/m]	6.00E5	6.00E5	7.50E5
K_{22}	[N/m]	6.00E5	6.00E5	7.50E5
K_{33}	[N/m]	8.66E8	8.66E8	1.08E9
C_{33}	[N/m]	7.89E6	7.89E6	7.89E6

5.4 Added mass and damping

Two floaters are suggested by NPRA, a concrete floater and a steel floater. The shape, dimensions and number of attached tethers are different between them. For steel, the number of tethers are 12, while for concrete the number of tethers are 16[21]. The shape and dimension have a significant influence on the added mass, and it is important to create a floater as similar as possible to the concrete floater. In this thesis, it was chosen to model the concrete floater, where the real floater constructed by NPRA and the simplified model are seen in figure 33a and 33b.

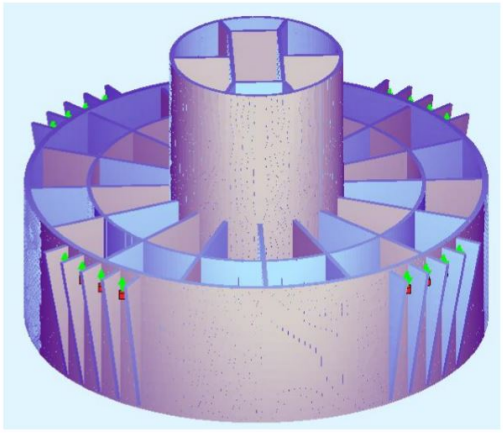

(a) Concrete floater[21]

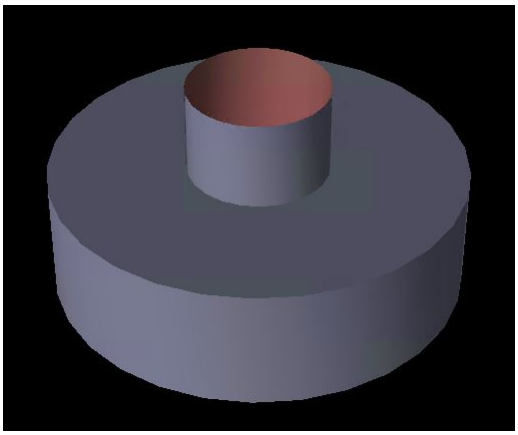

(b) Simplified concrete floater

Figure 33: The concrete floater created by NPRA and the simplified floater modelled in GeniE

In HydroD, the distance between the centre of buoyancy, COB, and centre of gravity, COG, was needed, and it was found from calculations that COB = COG, as can be seen in appendix C. The dimensions for the simplified floater are given in table 8, where r_1 and h_1 are the radius and the height of the caisson, i.e. the lower part, and r_2 and h_2 are the radius and the height of the cylinder, i.e. the upper part.

Table 8: Geometry for simplified floater

Item		Size
r_1	[m]	42.1
h_1	[m]	27.5
r_2	[m]	15.8
h_2	[m]	20

Added mass and damping for the floater were obtained by the hydrodynamic design tool HydroD. The maximum number of elements HydroD can handle, is 15 000, which limits how fine the mesh size can be. The mesh size was determined by executing several analyses for a reduced mesh size, and a possible convergence was studied. However, since the relation was linear, the finest possible mesh size was chosen, which is 1.25 metre. In appendix C, all obtained results are given.

The simplified concrete floater in HydroD for a given sea state, is seen in figure 34. Since the hydrodynamic effects are of interest, only the part of the structure below sea surface was created in GeniE.

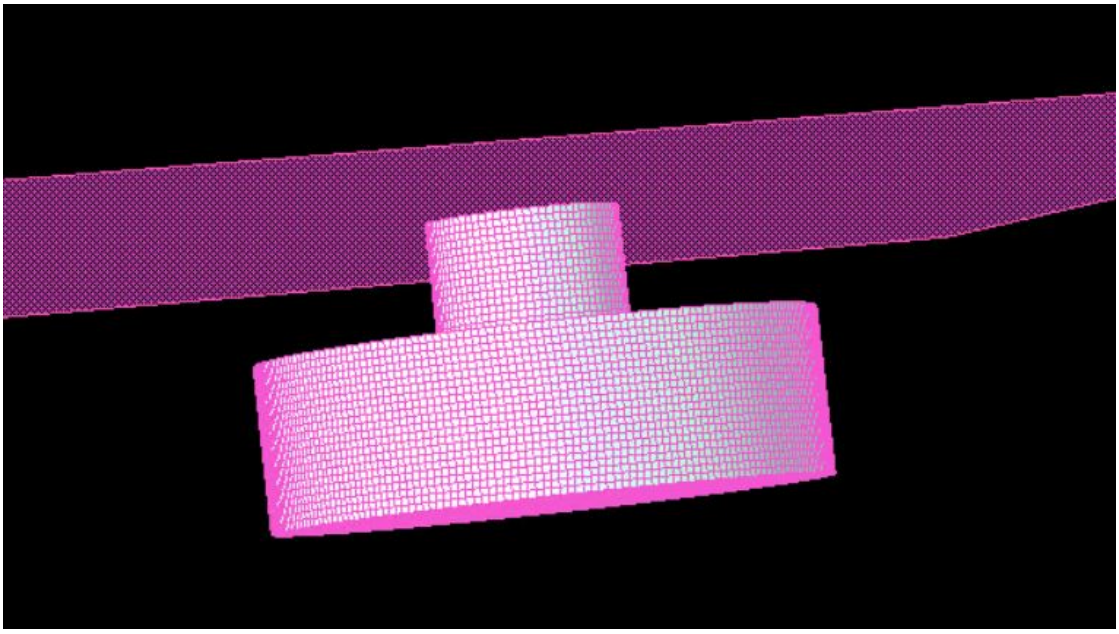

Figure 34: Simplified floater in HydroD

5.5 Eigenvalue

Equation 5.1 calculates the eigenfrequency ω, where K, M and A are the stiffness, mass and frequency-dependent added mass, respectively.

$$\omega = \sqrt{\frac{K}{M + A}} \tag{5.1}$$

To ensure that the mass and stiffness for the simplified models and Bjørnafjorden Bridge were similar, the eigenvalues obtained for the simplified models were compared to the eigenvalues from NPRA. The two smallest eigenfrequencies for the

model simulated by NPRA, are listed in table 9.

Table 9: Horizontal eigenfrequencies for Bjørnafjorden Bridge by NPRA[24]

Mode no.	Horizontal [Hz]
ω_1	9.09E-3
ω_2	1.67E-2

5.6 Static and dynamic loads

Static and dynamic loads are applied to the models, where current, traffic and wind are applied as static loads, and waves as a dynamic load. The environmental loads are determined for three return periods; 1-year return period, 50-year return period and 100-year return period. These were chosen since the bridge should be comfortable and safe for a 1-year storm, and undesirable structural effects should be avoided for a 100-year storm. The 50-year return period was chosen since missing data, such as wave height and wave period, are available from Sognefjorden for these three return periods. It is assumed that Bjørnafjorden is more exposed to environmental loads due to its location, and consequently, values employed from Sognefjorden are slightly increased. When determining environmental loads for a 100-year return period, a safety factor of 1.3 is included[47]. The traffic load is only applied in combination with environmental loads for 1-year return period, since it is assumed that the bridge is closed when environmental loads for higher return period are acting.

5.6.1 Current

The current is applied as a static concentrated load on the floaters, and as a simplification, the current velocity acting at the sea surface is utilized. The current velocities are available for 1-year return period, 10-year return period and 100-year

return period, and are given in table 10, for a decreasing water depth.

Table 10: Current velocity[48]

Depth [m]	1-year [m/s]	10-year [m/s]	100-year [m/s]
0 - 5	0.50	0.60	0.70
10	0.30	0.35	0.40
20	0.23	0.25	0.27
30	0.23	0.25	0.27
50	0.17	0.21	0.25
100	0.13	0.14	0.16
150	0.13	0.14	0.16

Given data for Bjørnafjorden is only available for 1-year return period and 100-year return period. According to table 10, the 10-year current velocity is about the average of the 1-year and the 100-year. The 50-year current velocity is set to 0.66 m/s, and is estimated as the average between the 10-year and 100-year return period, and then slightly increased. The fluid surrounding the concrete floater is in-between laminar and turbulent flow. In addition, the shape of the floater can be considered as a rectangular. From these assumption, the drag coefficient is assumed to be 1.14[34]. Calculated current load for the three current velocities are given in table 11. Calculations of the current load, is given in appendix C.

Table 11: The acting current force for the three return periods

Return period	$v_c\,[m/s]$	$F_{current}\,[N/m]$
1-year	0.50	93 253.6
50-year	0.66	162 483
100-year	0.70	237 608

5.6.2 Traffic load

The traffic load is applied as a static line load along the bridge deck. The traffic load is a combination of a uniformly distributed load and a concentrated load. The concentrated load is a fluctuating load, and it is neglected in this thesis as a simplification. This means that the traffic load only consists of the uniformly distributed load at the traffic lanes and the pedestrian lane. The models are assumed to have the same number of traffic lanes as the proposed crossing, which is four traffic lanes and one pedestrian lane. As a simplification, equal traffic is assumed in both directions. The traffic load is first determined for one direction and then multiplied with two. By assuming normal heavy vehicle traffic, the α-factors utilized are from the 2^{nd} class. The traffic load from cars are estimated to be $q_{traffic} = 65.3kN/m$, where the calculations are seen in appendix C. In addition to traffic weight, the load from the footpath must be included. According to Eurocode 1, the footpath uniformly distributed load is 15 kN/m, while the uniformly distributed load according to N400 is 6 kN/m. However, the bridge is more than 5000-metre-long, and it is unlikely that the bridge is fully loaded at the footpath in addition to be fully loaded with cars. Even during an emergency, this is unlikely, since the calculated traffic load includes passengers. The footpath load utilized in this thesis is the same as NPRA is assuming, which is 2 kN/m[21]. Total uniformly distributed traffic and pedestrian load is then estimated to be $q_{traffic} = 67.3kN/m$.

5.6.3 Wind

When estimating the wind force, the shape factor must be determined, and according to DNV, the shape coefficient for the bridge girder is 1.2[28]. Calculated wind force for the different return periods and wind velocities, are given in table 12, where the utilized wind velocities are obtained from the report Design Basis from NPRA[48]. The calculations can be seen in appendix C.

Table 12: Acting wind force

Return period	$U_w\,[m/s]$	$F_{wind}\,[N/m]$
1-year	19.4	1661.10
50-year	26.0	2983.59
100-year	27.0	4182.77

5.6.4 Waves

The incoming wave is assumed to be concentrated and act horizontally and vertically on the floaters. To determine the significant wave height, H_s, data were taken from Nordhordland Bridge[12] and Sognefjorden[49] as a first estimate. For Sognefjorden, only values for H_{mo} are available. Since the significant wave height is calculated from the spectre, H_{mo} is equal to H_s[50]. A range for the wave period, T_p, was given, where the longest period was chosen as a conservative assumption. The wave-characteristic for the three return periods are given in table 13.

Table 13: Characteristics for incoming wave for three return periods

		1-year	50-year	100-year
H_s	[m]	1.1	2.1	2.6
T_p	[s]	4.5	5.1	5.5

Summarizing equations 2.17 and 2.22, the vertical force is estimated. To be able to determine the diffraction forces, the added mass coefficient had to be decided. When determining the added mass, m_a, in heave, the floater is regarded as a three-dimensional body, and the reference volume must be determined. Since the floaters can be viewed as circular discs[24], the added mass coefficient for vertical motion, $C_{a,3}$, is set to 0.637[29], and the reference volume is given by equation 5.2 where D is the diameter of the floater.

$$V_R = \frac{\pi}{6} D^3 \tag{5.2}$$

The calculated vertical forces are given in table 14, and the calculations are given in appendix C.

Table 14: Vertical forces due to incoming wave

			1-year	50-year	100-year
F_{FK}	$\cos(\omega t)$	[N]	-279 993	-684 601	-763 737
F_{Diff}	$\cos(\omega t)$	[N]	-937.175	11 266.9	-33 600.6
F_{tot}	$\cos(\omega t)$	[N]	-280 930	-695 868	-1 036 539

To determine the horizontal force, equation 2.17 and 2.21 are summarized. However, the reference volume is replaced by the section area given by equation 5.3, and then integrated over the depth, and the added mass coefficient is set to 1. The horizontal forces are given in table 15 and the calculations are given in appendix C.

$$A_s = \frac{\pi D^2}{4} \tag{5.3}$$

Table 15: Horizontal forces due to incoming wave

			1-year	50-year	100-year
F_{FK}	$\sin(\omega t)$	[N]	-279 993	-684 601	-763 737
F_{Diff}	$\sin(\omega t)$	[N]	-8 782 597	-13 016 146	-10 735 407
F_{tot}	$\sin(\omega t)$	[N]	-9 062 591	-13 700 747	-14 948 886

In addition, the first obtained horizontal and vertical eigenfrequencies were utilized as the wave frequency. The procedure to determine the horizontal and vertical wave load, is the same as described above.

6 Results

In this chapter, the results for added mass and damping caused by the floaters are first presented, then the results from the eigenvalue analysis is presented. Finally, the results from the static and dynamic analysis is presented. In the dynamic analysis, the longitudinal and vertical displacement of the TLPs are presented for the models.

6.1 Added mass and damping

The added mass and damping are equal for all models, since it is assumed that the same floater support all models. The added mass for the floaters in heave, is seen in figure 35. As the period increases, the added mass converges. Since it is expected that the eigenfrequencies are small for the structure, a constant added mass of 3.52E8 kg is applied in the analyses.

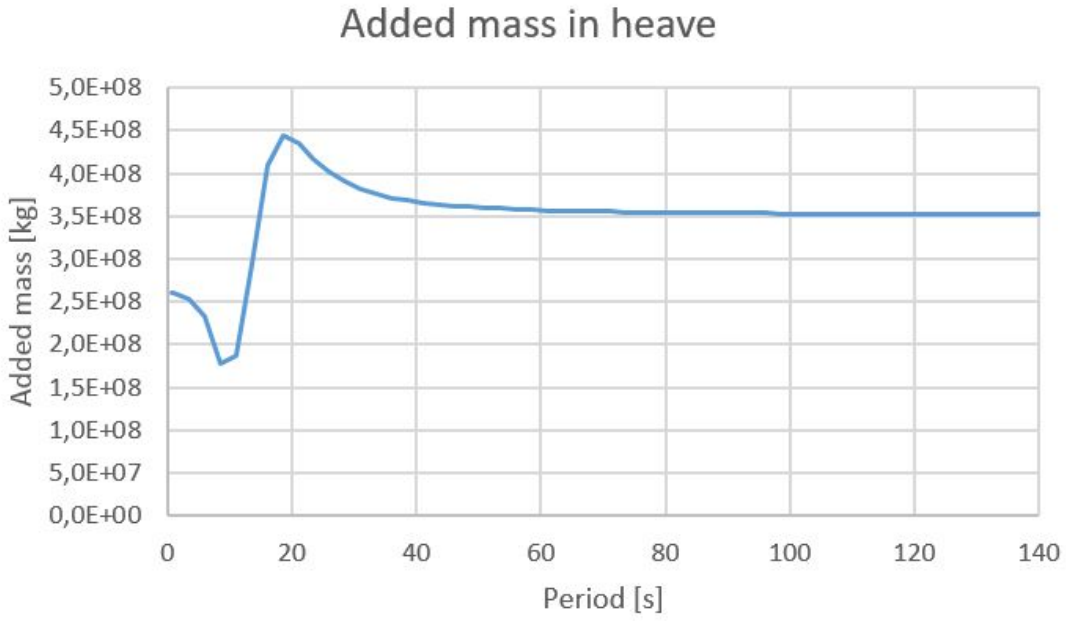

Figure 35: Added mass of the floater in heave

Due to the symmetry of the floater, it is expected that the added mass in sway and surge are similar, which also the analysis confirmed. The obtained added mass for the floaters in sway, is given in figure 36.

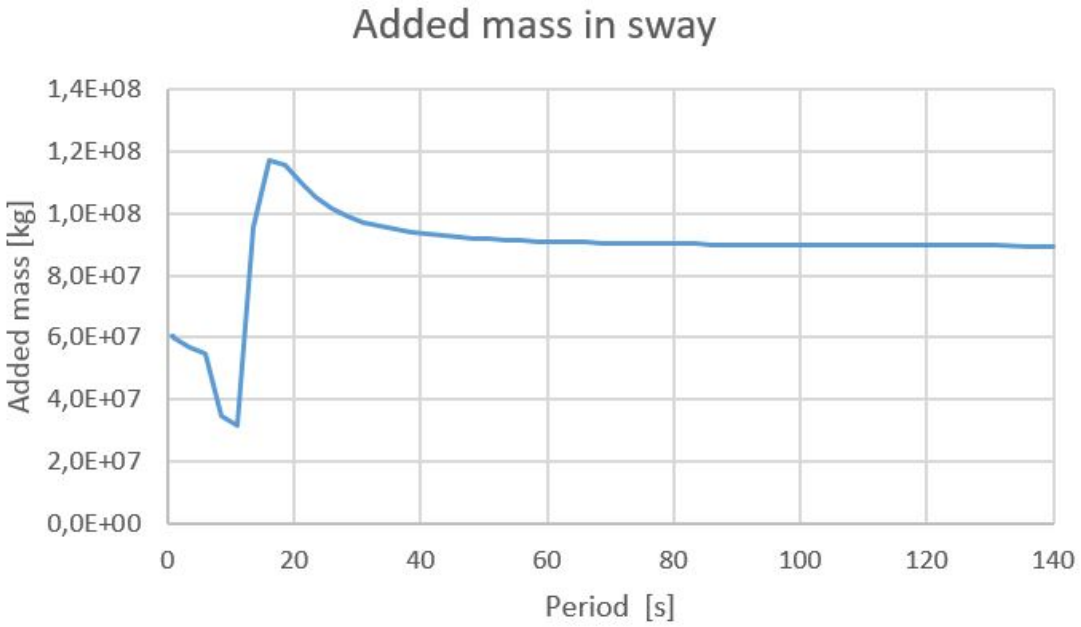

Figure 36: Added mass of the floater in sway

According to figure 36, the added mass converges to 9E7 kg after a period of 50 seconds, and this constant added mass is applied in the analyses. The obtained damping in heave and sway are seen in figure 37 and figure 38. The damping has a peak from about 10 seconds to 15 seconds, and after 30 seconds, the damping is close to zero. This is true for all degrees of freedom. The damping is neglected in the analyses, since the value for higher period are of interest, and in this area, damping is negligible.

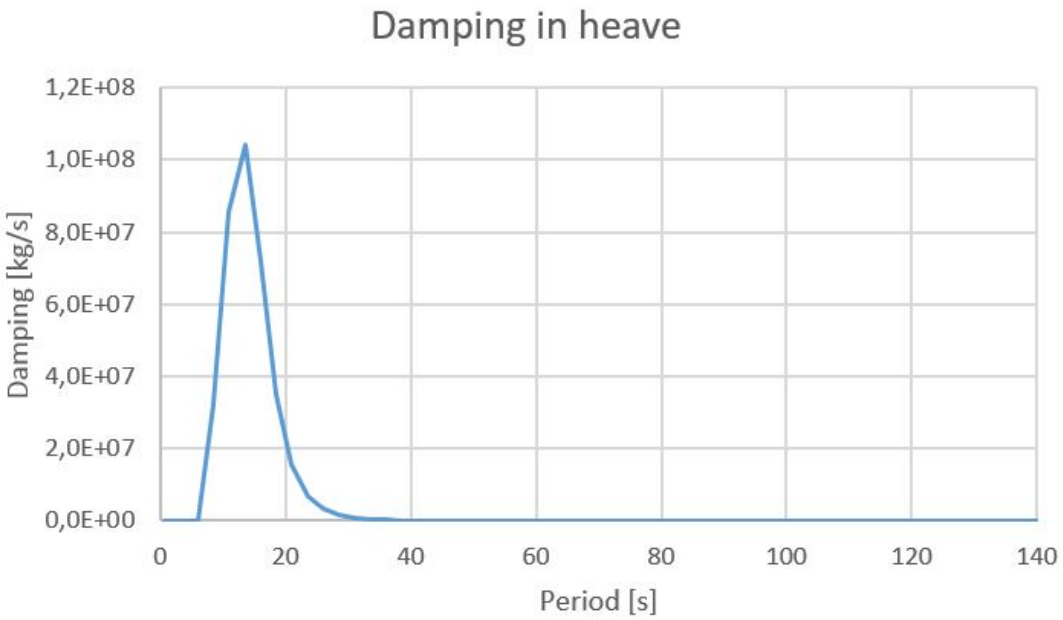

Figure 37: Damping of the floater in heave

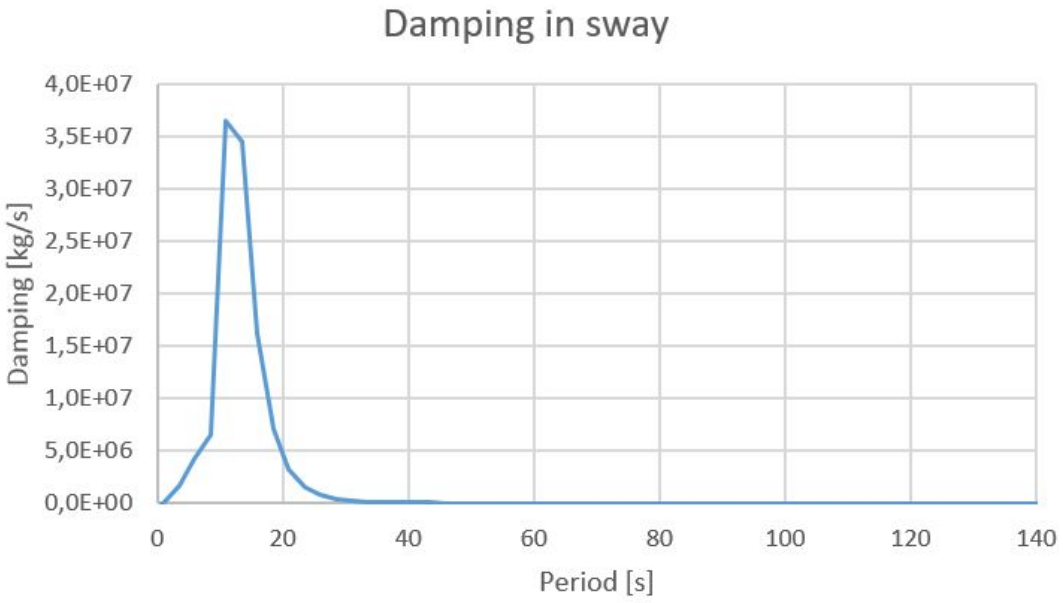

Figure 38: Damping of the floater in sway

6.2 Eigenmode

By performing an eigenvalue analysis, the behaviour of the models is studied. When the eigenfrequencies and belonging eigenperiods to the models are revealed, it can be determined in an early stage if the incoming wave frequency for the location might causes difficulties, such as resonance. In addition to the first ten eigenfrequencies for the models, the first ten resulting eigenmode are given for each model to illustrate their behaviour.

Model 1

In table 16, the first ten obtained eigenfrequencies and belonging eigenperiods, T, for Model 1, are presented, where f and ω are the eigenfrequency measured in Hz and rad/s, respectively. In addition, the direction of motion for the eigenmodes are given.

Table 16: The first ten eigenfrequencies and eigenperiods for Model 1

Mode no.	f [Hz]	ω [rad/s]	T [s]	Motion
1	1.01E-02	0.0634	99.18	Horizontal
2	1.42E-02	0.0893	70.40	Vertical
3	1.98E-02	0.125	50.41	Vertical
4	2.43E-02	0.153	41.09	Horizontal
5	2.46E-02	0.154	40.69	Vertical
6	5.03E-02	0.316	19.86	Vertical
7	5.46E-02	0.343	18.30	Horizontal
8	5.91E-02	0.372	16.91	Vertical
9	6.73E-02	0.423	14.87	Vertical
10	8.45E-02	0.531	11.83	Horizontal

The first ten eigen shapes for Model 1 are seen in figure 39. For horizontal displacement, the eigenmode is pictured from plan view, and for vertical displacement, the eigenmode is pictured from side view.

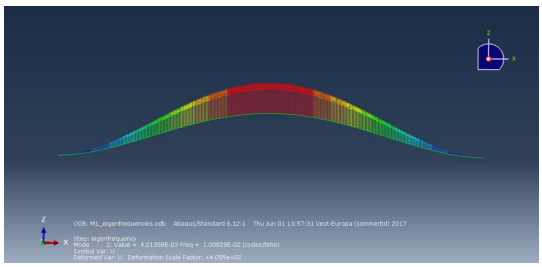

(a) First eigenmode, $\omega_1 = 0.0634$

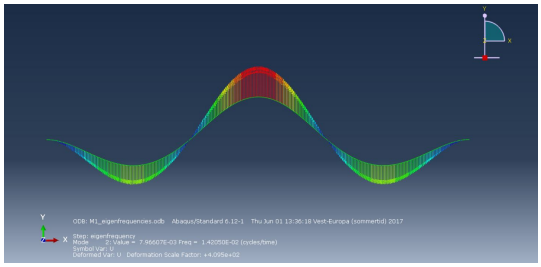

(b) Second eigenmode, $\omega_2 = 0.0893$

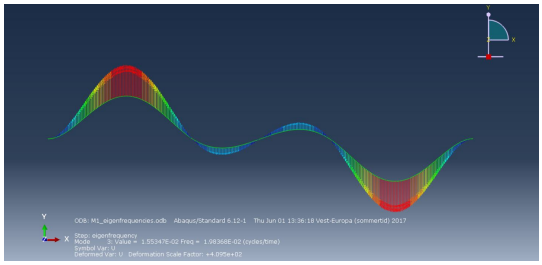

(c) Third eigenmode, $\omega_3 = 0.125$

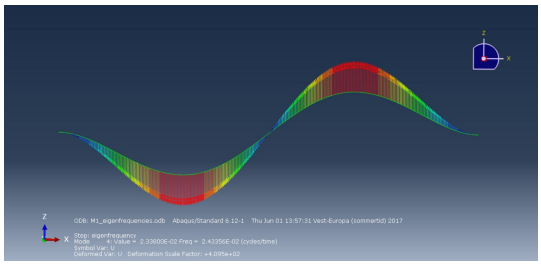

(d) Fourth eigenmode, $\omega_4 = 0.153$

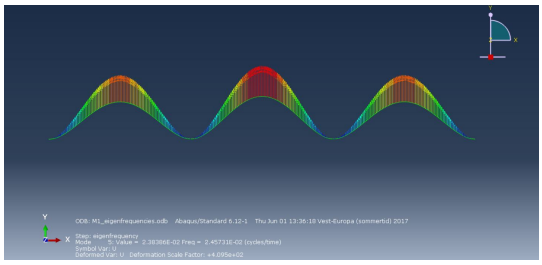

(e) Fifth eigenmode, $\omega_5 = 0.154$

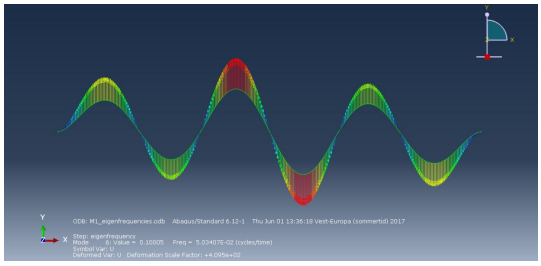

(f) Sixth eigenmode, $\omega_6 = 0.316$

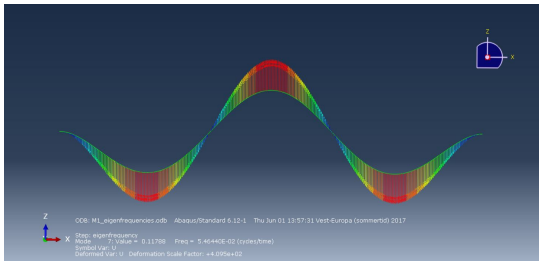

(g) Seventh eigenmode, $\omega_7 = 0.343$

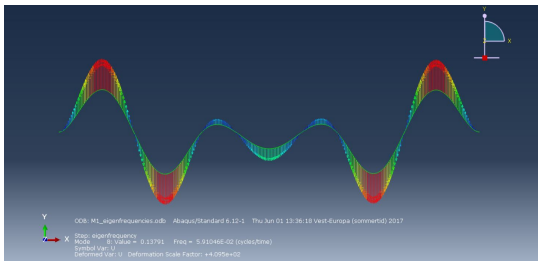

(h) Eight eigenmode, $\omega_8 = 0.372$

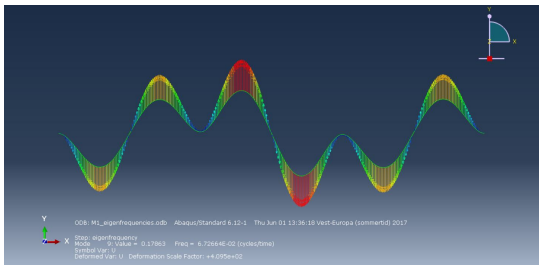

(i) Ninth eigenmode, $\omega_9 = 0.423$

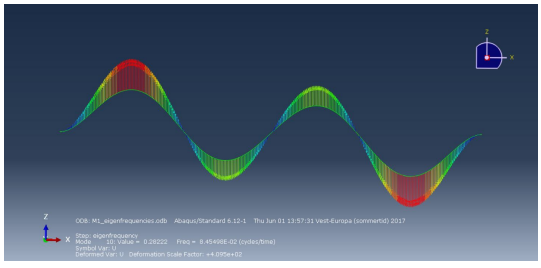

(j) Tenth eigenmode, $\omega_{10} = 0.531$

Figure 39: The first ten eigenmodes for Model 1

Model 2

In table 17, the first ten obtained eigenfrequencies and belonging eigenperiods for Model 2, are presented. In addition, the direction of motion for the eigenmodes are given.

Table 17: The first ten eigenfrequencies and eigenperiods for Model 2

Mode no.	f [Hz]	ω [rad/s]	T [s]	Motion
1	9.99E-03	0.0628	100.1	Horizontal
2	1.15E-02	0.0721	87.16	Vertical
3	1.60E-02	0.101	62.39	Vertical
4	1.99E-02	0.125	50.32	Vertical
5	2.40E-02	0.151	41.61	Horizontal
6	4.07E-02	0.256	24.59	Vertical
7	4.78E-02	0.300	20.92	Vertical
8	5.40E-02	0.339	18.51	Horizontal
9	5.46E-02	0.343	18.32	Vertical
10	8.35E-02	0.525	11.97	Horizontal

The eigenmodes belonging to the first ten eigenfrequencies for Model 2 are seen in figure 40. The first three eigenmodes have similar displacement as Model 1, but the first eigenmode occur for a smaller eigenfrequency, while the second and third eigenmodes occur for a significant smaller eigenfrequency. This trend continues for the vertical eigenmodes; they generally occur for smaller eigenfrequencies compared to Model 1. The direction of motion for Model 1 is first horizontal, then two eigenmodes with vertical displacement, then one eigenmode with horizontal displacement before two eigenmodes with vertical displacement. For Model 2, the first eigenmode has horizontal displacement, then three eigenmodes occur with vertical displacement, before one horizontal eigenmode occur. Then, two vertical eigenmodes occur before a horizontal eigenmode. Eigenmode number nine has vertical displacement and the tenth has horizontal. This means that the first three eigenmodes and the sixth and the two last eigenmodes have similar shapes when comparing Model 1 and Model 2.

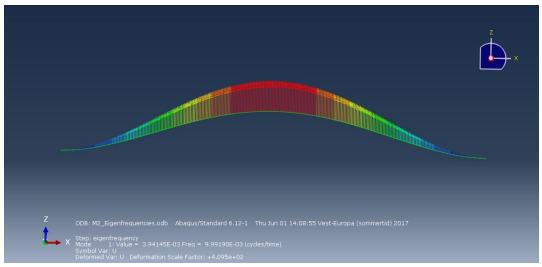

(a) First eigenmode, $\omega_1 = 0.0628$

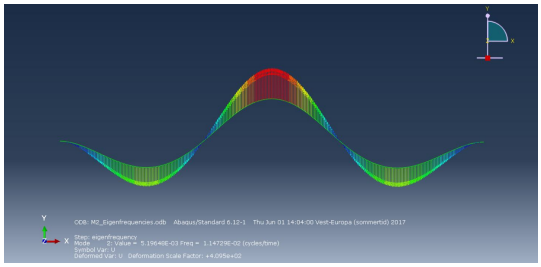

(b) Second eigenmode, $\omega_2 = 0.0721$

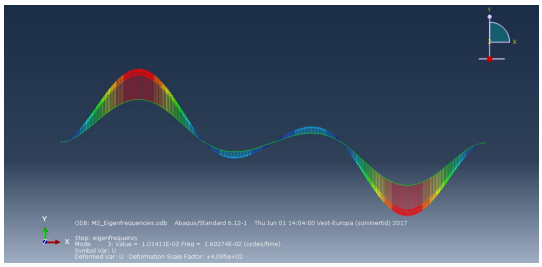

(c) Third eigenmode, $\omega_3 = 0.101$

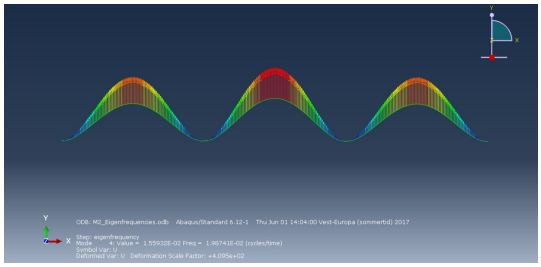

(d) Fourth eigenmode, $\omega_4 = 0.125$

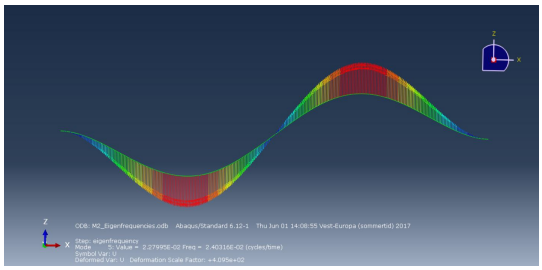

(e) Fifth eigenmode, $\omega_5 = 0.151$

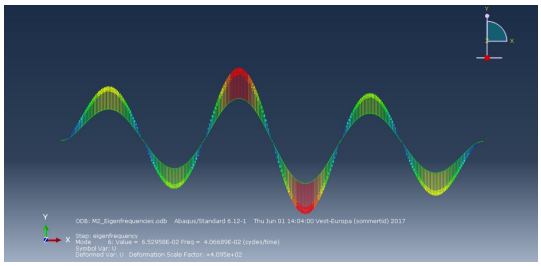

(f) Sixth eigenmode, $\omega_6 = 0.256$

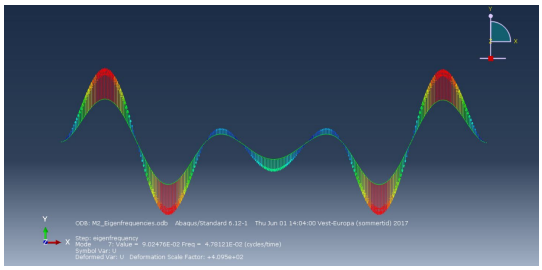

(g) Seventh eigenmode, $\omega_7 = 0.300$

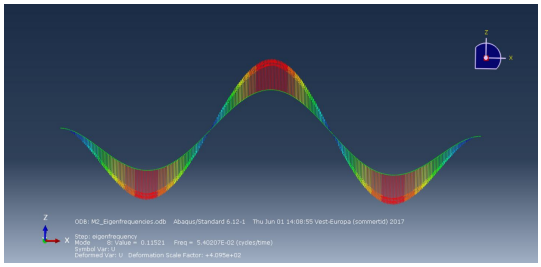

(h) Eight eigenmode, $\omega_8 = 0.339$

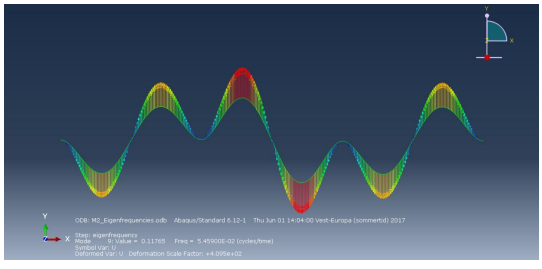

(i) Ninth eigenmode, $\omega_9 = 0.343$

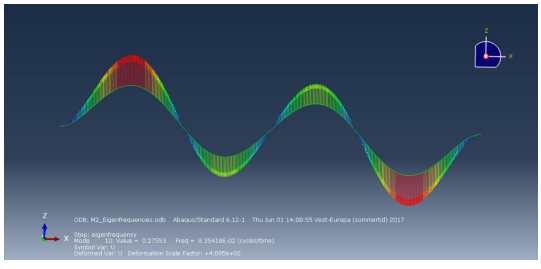

(j) Tenth eigenmode, $\omega_{10} = 0.525$

Figure 40: The first ten eigenmodes for Model 2

Model 3

In table 18, the first ten obtained eigenfrequencies and belonging eigenperiods for Model 3, are presented. In addition, the direction of motion for the eigenmodes are given.

Table 18: The first ten eigenfrequencies and eigenperiods for Model 3

Mode no.	f [Hz]	ω [rad/s]	T [s]	Motion
1	1.02E-02	0.0641	98.07	Horizontal
2	1.47E-02	0.0921	68.25	Vertical
3	2.05E-02	0.129	48.87	Vertical
4	2.40E-02	0.151	41.61	Horizontal
5	2.54E-02	0.159	39.43	Vertical
6	5.19E-02	0.326	19.26	Vertical
7	5.56E-02	0.349	18.00	Horizontal
8	6.10E-02	0.383	16.40	Vertical
9	6.95E-02	0.437	14.39	Vertical
10	8.51E-02	0.535	11.75	Horizontal

The first ten eigenmodes for Model 3 are seen in figure 41. The distribution between horizontal and vertical displacement, are similar as for Model 1, and the shape is similar. The horizontal displacement occurs for a smaller eigenfrequency than for Model 1, but the deviation for vertical displacement are clearer between these models; the vertical eigenmodes occurs for a smaller eigenfrequency for Model 3.

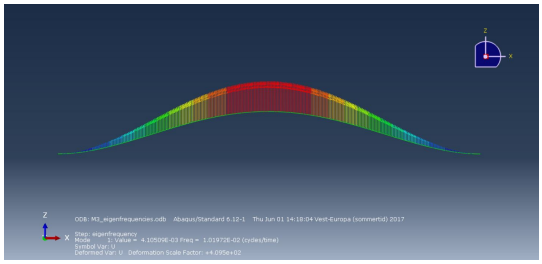

(a) First eigenmode, $\omega_1 = 0.0641$

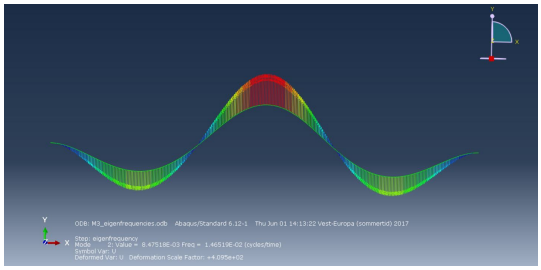

(b) Second eigenmode, $\omega_2 = 0.0921$

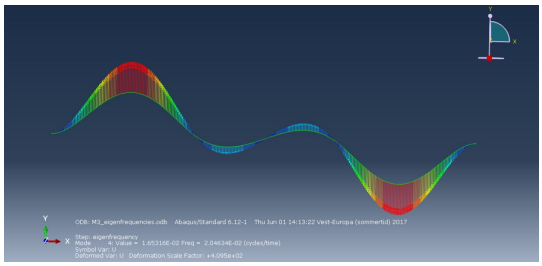

(c) Third eigenmode, $\omega_3 = 0.129$

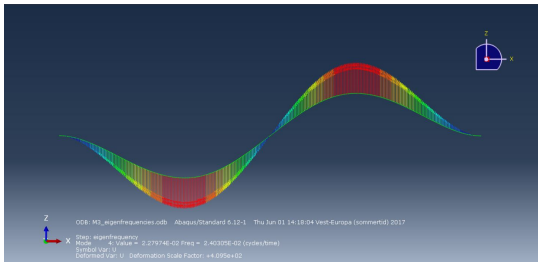

(d) Fourth eigenmode, $\omega_4 = 0.151$

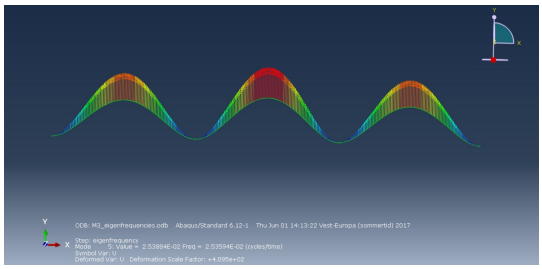

(e) Fifth eigenmode, $\omega_5 = 0.159$

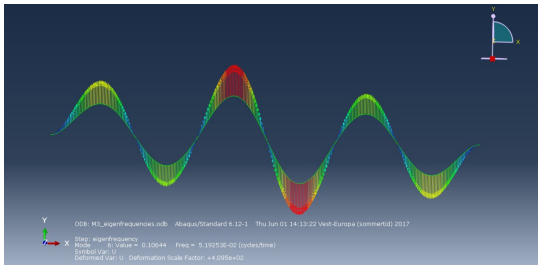

(f) Sixth eigenmode, $\omega_6 = 0.326$

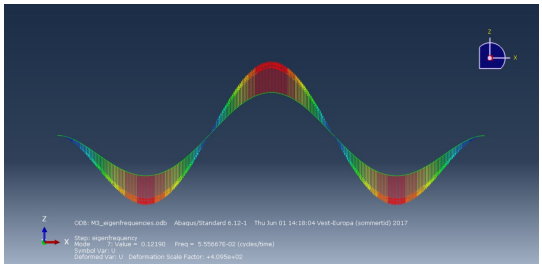

(g) Seventh eigenmode, $\omega_7 = 0.349$

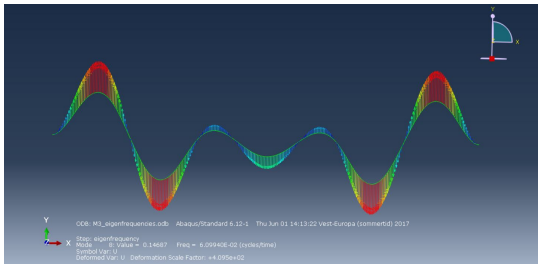

(h) Eight eigenmode, $\omega_8 = 0.383$

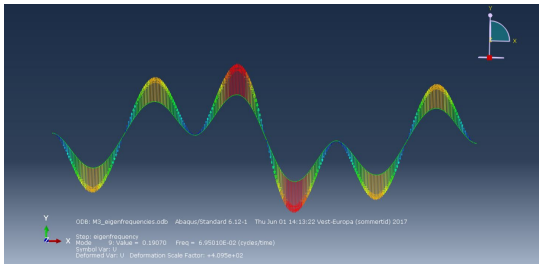

(i) Ninth eigenmode, $\omega_9 = 0.437$

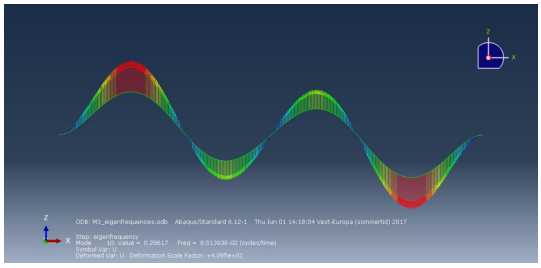

(j) Tenth eigenmode, $\omega_{10} = 0.535$

Figure 41: The first ten eigenmodes for Model 3

Model 4

In table 19, the first ten obtained eigenfrequencies and belonging eigenperiods for Model 4, are presented. In addition, the direction of motion for the eigenmodes are given.

Table 19: The first ten eigenfrequencies and eigenperiods for Model 4

Mode no.	f [Hz]	ω [rad/s]	T [s]	Motion
1	9.97E-03	0.0626	100.3	Horizontal
2	2.25E-02	0.141	44.50	Vertical
3	2.42E-02	0.152	41.26	Horizontal
4	3.01E-02	0.189	33.27	Vertical
5	3.88E-02	0.244	25.79	Vertical
6	4.33E-02	0.272	23.11	Vertical
7	4.42E-02	0.278	22.61	Horizontal
8	8.33E-02	0.524	12.00	Vertical
9	8.88E-02	0.558	11.26	Horizontal
10	9.65E-02	0.606	10.37	Vertical

The first ten eigenmodes for Model 4 are seen in figure 42. From the first ten eigenmodes, four have horizontal displacement while six have vertical displacement. The horizontal eigenmodes have similar shapes as Model 1, with exception of the fourth horizontal eigenmode. The horizontal eigenmodes occur for a slightly smaller eigenfrequency for Model 4 compared to Model 1. The vertical eigenmodes for Model 4 have different shape than for Model 1, which is because Model 4 has three TLPs compared to the two for the previous models. The first vertical eigenmode occur for a significantly higher eigenfrequency, while the second vertical eigenmode for Model 4 occurs for a smaller eigenfrequency.

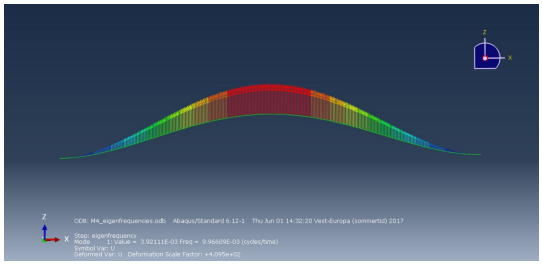

(a) First eigenmode, $\omega_1 = 0.0626$

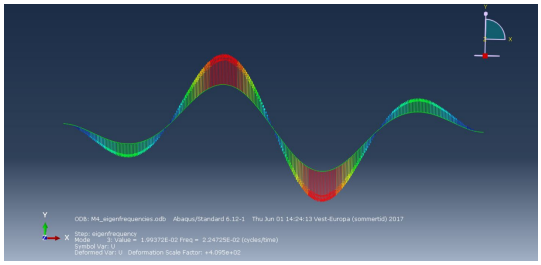

(b) Second eigenmode, $\omega_2 = 0.141$

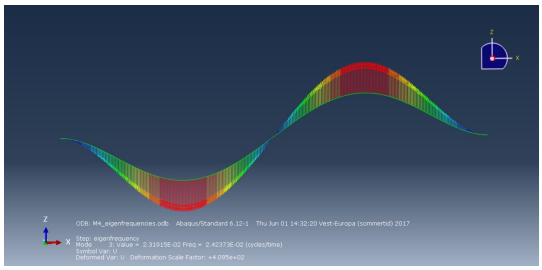

(c) Third eigenmode, $\omega_3 = 0.152$

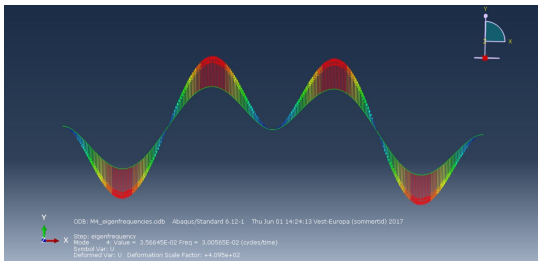

(d) Fourth eigenmode, $\omega_4 = 0.189$

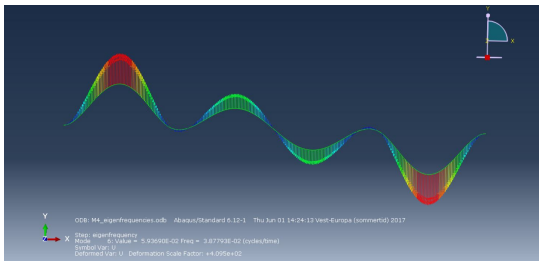

(e) Fifth eigenmode, $\omega_5 = 0.244$

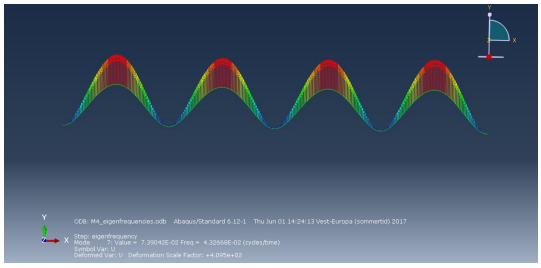

(f) Sixth eigenmode, $\omega_6 = 0.272$

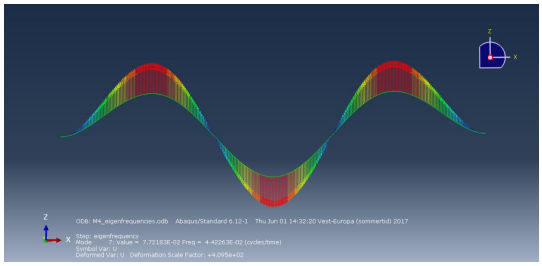

(g) Seventh eigenmode, $\omega_7 = 0.278$

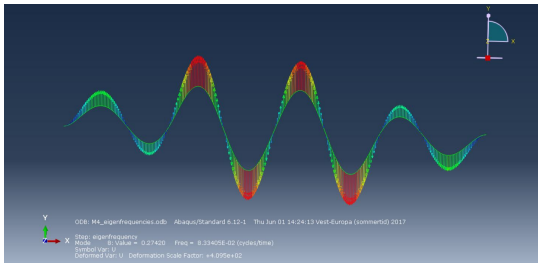

(h) Eight eigenmode, $\omega_8 = 0.524$

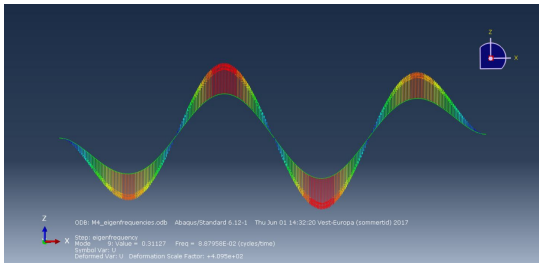

(i) Ninth eigenmode, $\omega_9 = 0.558$

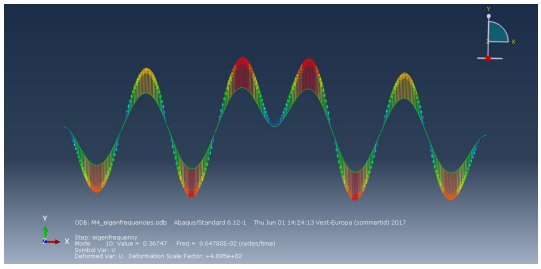

(j) Tenth eigenmode, $\omega_{10} = 0.606$

Figure 42: The first ten eigenmodes for Model 4

6.3 Static results

In this section, the static results are given for each model. The static load contributors are current, traffic and wind, and figure 43 illustrates how the static loads are acting on Model 1, Model 2 and Model 3. Model 4 has an extra TLP, but the loads are applied at this model in the same manner as for the previous models. The current is applied as a concentrated load acting horizontally on the TLPs. The traffic load is applied as a vertical line load and the wind as a horizontal line load. The static response for this return period, are longitudinal and vertical displacement, U3 and U2, along the bridge, in addition to the bending moment, M2. However, traffic is only acting in combination with the 1-year static loads. Since current and wind, have nearly no displacement in vertical direction, only the longitudinal displacement and the bending moment along the bridge, are presented for the 50-year and 100-year return period. For all return periods, the magnitude of the bending moment is on the left axis and the magnitude for longitudinal and vertical displacement are on the right axis.

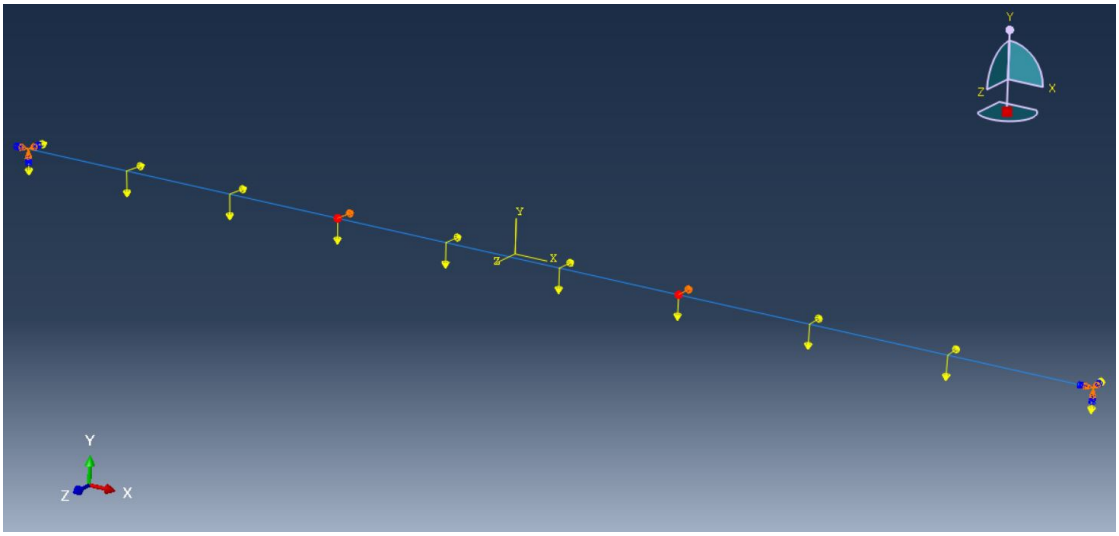

Figure 43: How the static loads are applied in the models

6.3.1 Model 1

In figure 44, the static responses caused by 1-year static loads are illustrated. The maximum positive and negative bending moment occur at the end-nodes and at the mid-point of Model 1, with the values 1.69E9 Nm and -7.92E8 Nm. The largest vertical displacement is -6.45 metres, and occur between the end-nodes and the TLPs, where the TLPs are positioned at 1385 metres and 2710 metres in figure 44. The maximum longitudinal displacement occurs at the mid-point of Model 1 with a value of -0.795 metres.

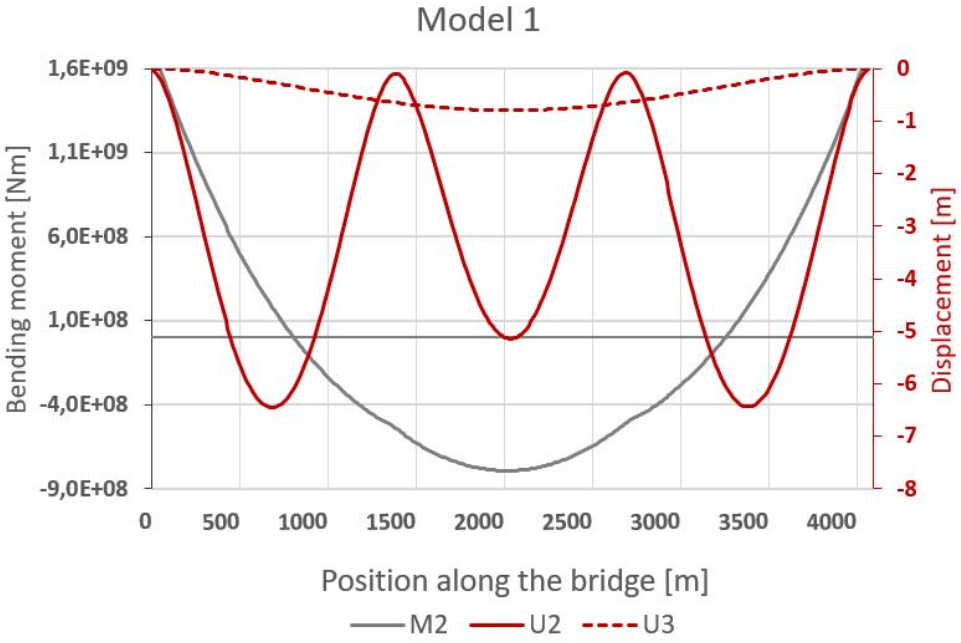

Figure 44: Static response for Model 1 for 1-year static loads

In figure 45 and figure 46, the static response for 50-year and 100-year loads, are illustrated. The behaviour is similar, but the 100-year static loads give larger responses. The maximum positive and negative bending moment for 50-year static loads are 3.36E9 Nm and -1.73E9 Nm. For the 100-year static loads, the maximum positive and negative bending moment increases to 4.68E9 Nm and -2.41E9 Nm. The largest longitudinal displacement is -1.68 metres for 50-year static loads, and for -2.33 metres for 100-year static loads.

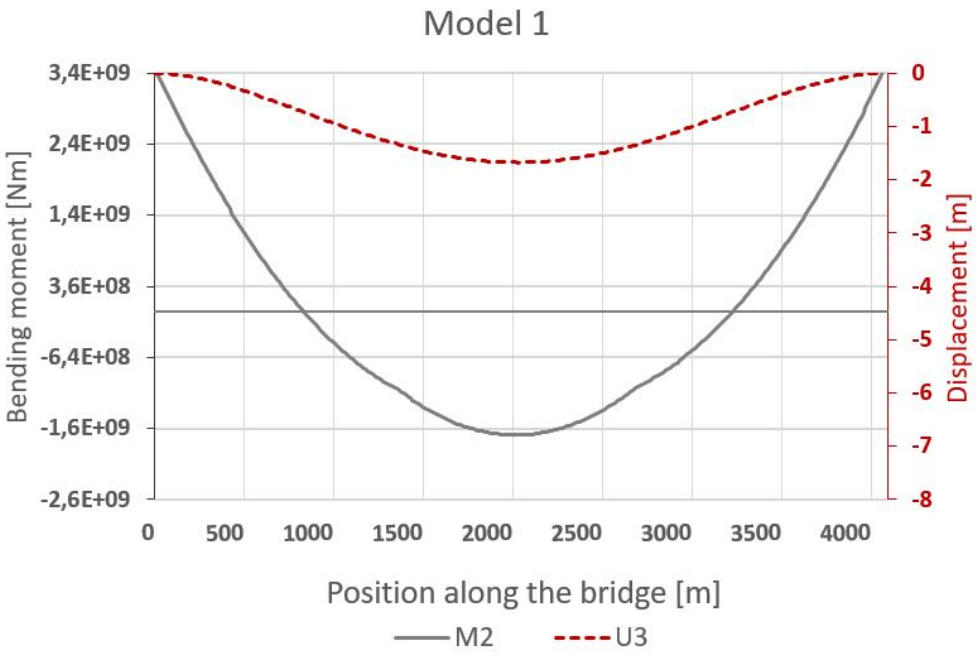

Figure 45: Static response for Model 1 for 50-year static loads

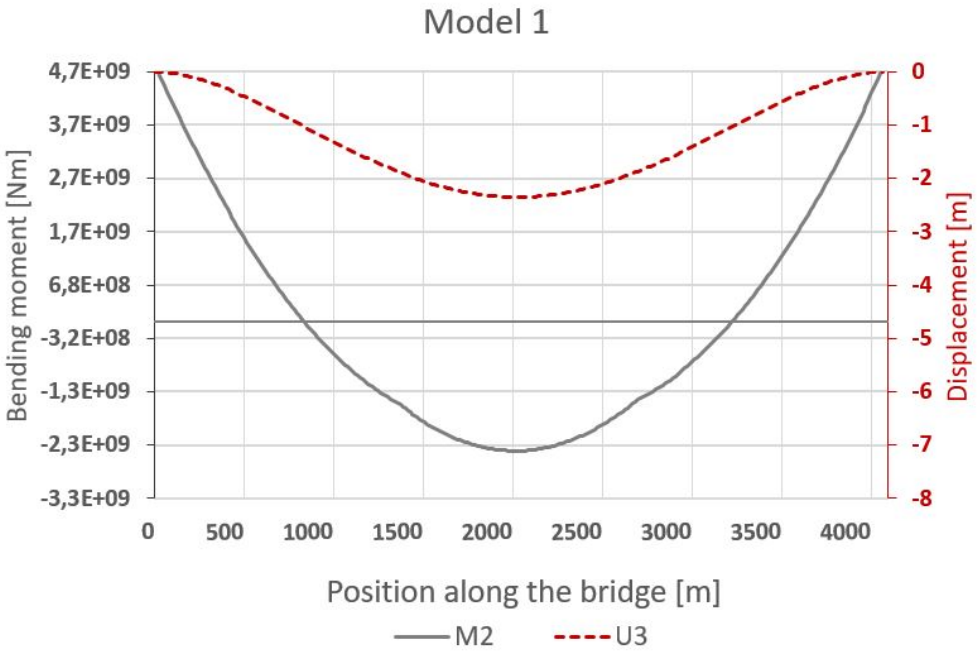

Figure 46: Static response for Model 1 for 100-year static loads

6.3.2 Model 2

In figure 47, the static response for Model 2 is illustrated. The bending moment has its largest positive and negative values at the end-nodes and at the mid-point, and have a magnitude of 1.62E9 Nm and -7.26E8 Nm. The vertical displacement has the largest value between the end-nodes and the TLPs, while the maximum longitudinal displacement occurs at the mid-point of the model. The largest longitudinal and vertical displacement are -0.768 metres and -7.57 metres.

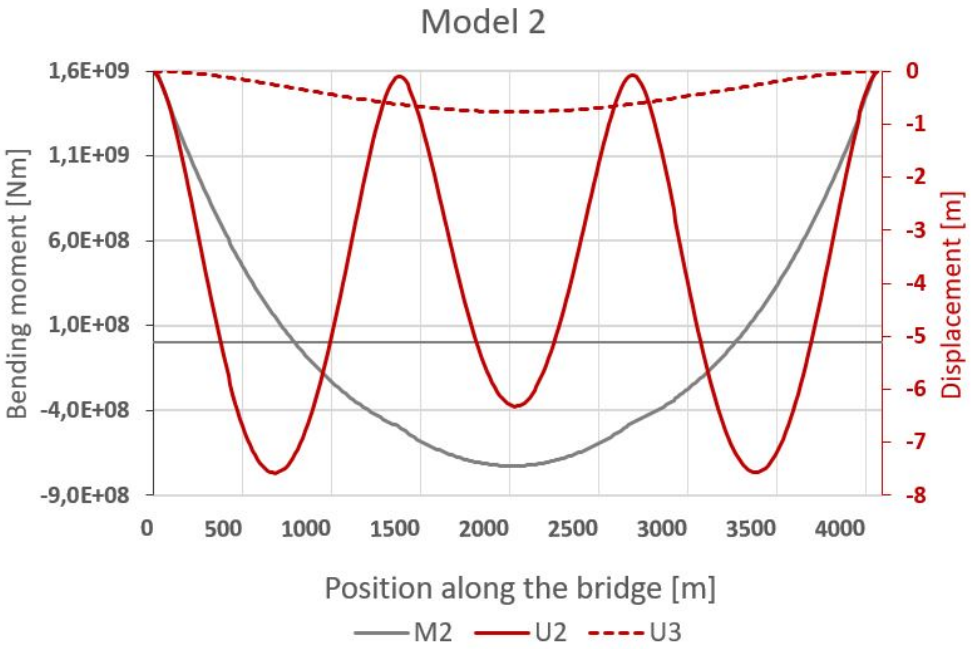

Figure 47: Static response for Model 2 for 1-year static loads

In figure 48 and figure 49, the static response caused by the 50-year static loads and 100-year static loads, are illustrated. The positive and negative maximum bending moment occur at the end-nodes and mid-point of Model 2, with the values 3.34E9 Nm and -1.72E9 Nm for the 50-year static loads. When the 100-year static loads are applied at the model, the maximum positive and negative bending moment is 4.68E9 Nm and -2.41E9 Nm. The largest longitudinal displacement occurs at the mid-point of Model 2 with a value of -1.73 metres for the 50-year static loads, and increases to -2.42 metres for the 100-year static loads.

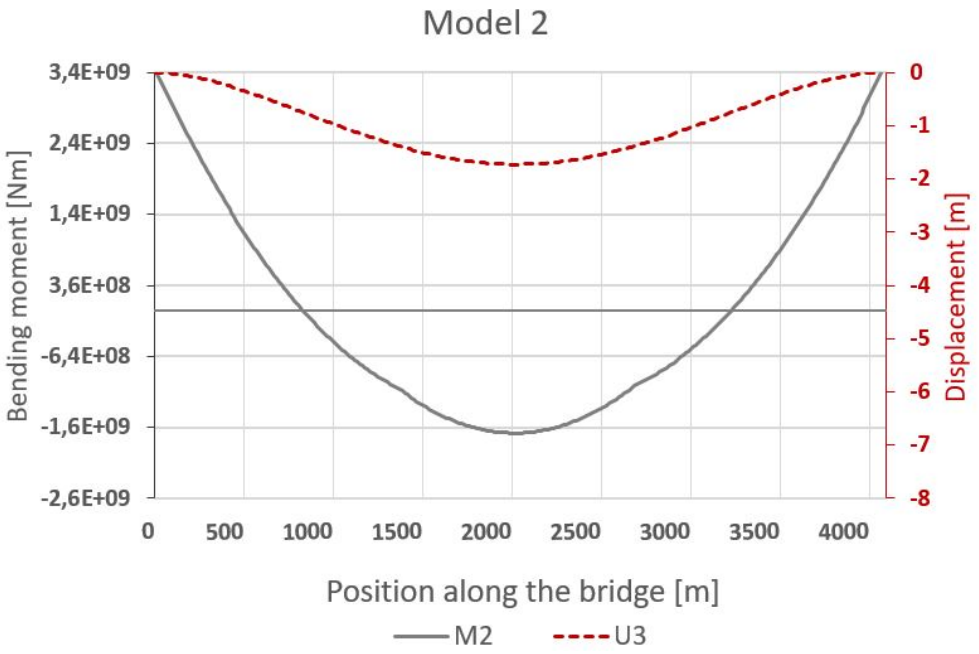

Figure 48: Static load for Model 2 for 50-year static loads

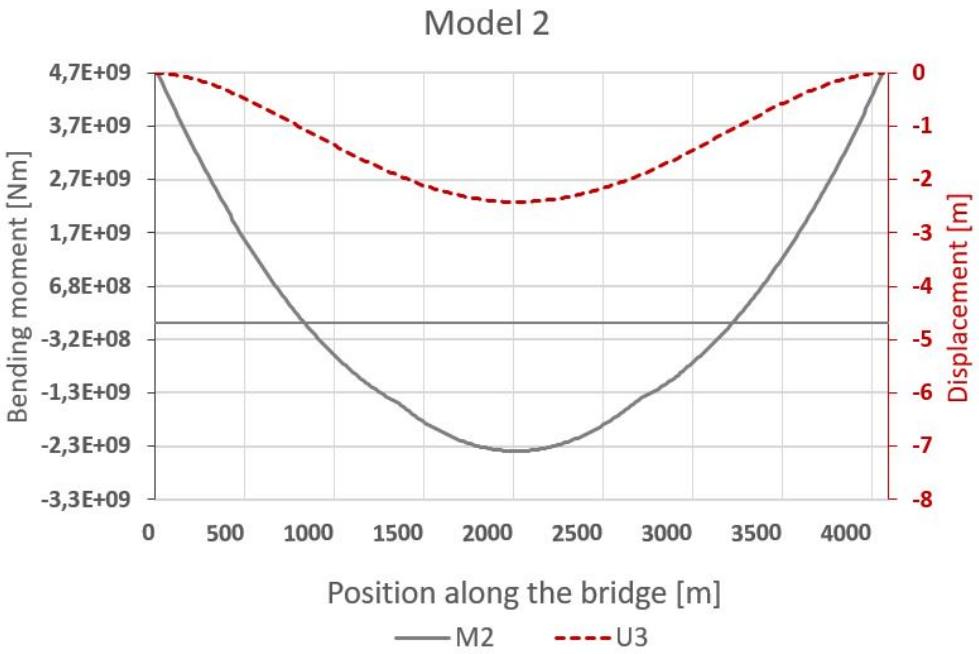

Figure 49: Static response for Model 2 for 100-year static loads

6.3.3 Model 3

In figure 50, the static response for Model 3 is illustrated. The bending moment has the largest positive and negative values at the end-nodes and at the mid-point, and have a magnitude of 1.61E9 Nm and -7.37E8 Nm. The vertical displacement has the largest value between the end-nodes and the TLPs, while the maximum longitudinal displacement occurs at the mid-point of the model. The largest longitudinal and vertical displacement are -0.899 metres and -7.23 metres.

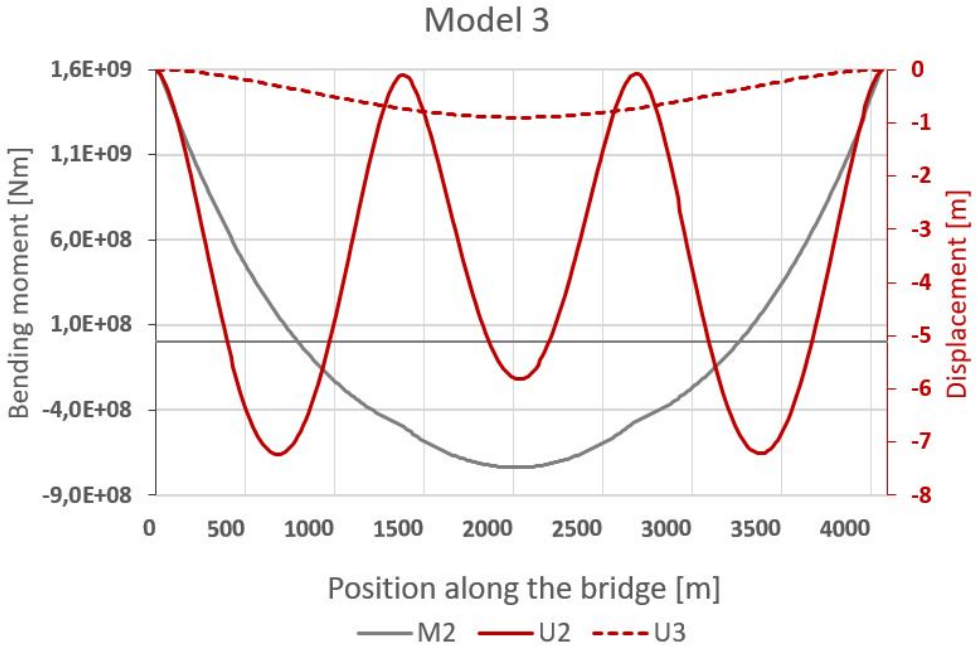

Figure 50: Static response for Model 3 for 1-year static loads

In figure 51 and figure 52, the static response caused by the 50-year and 100-year static loads, are illustrated. The maximum positive and negative bending moment occur at the end-nodes and mid-point of Model 3, and positive and negative maximum bending moment is 3.24E9 Nm and -1.67E9 Nm for the 50-year return period. When the 100-year static load are applied, the positive and negative maximum bending moment increases to 4.54E9 Nm and -2.33E9 Nm. The largest longitudinal displacement occurs at the mid-point of Model 3 with a value of -1.94 metre and -2.72 for the 50-year static loads and 100-year static loads.

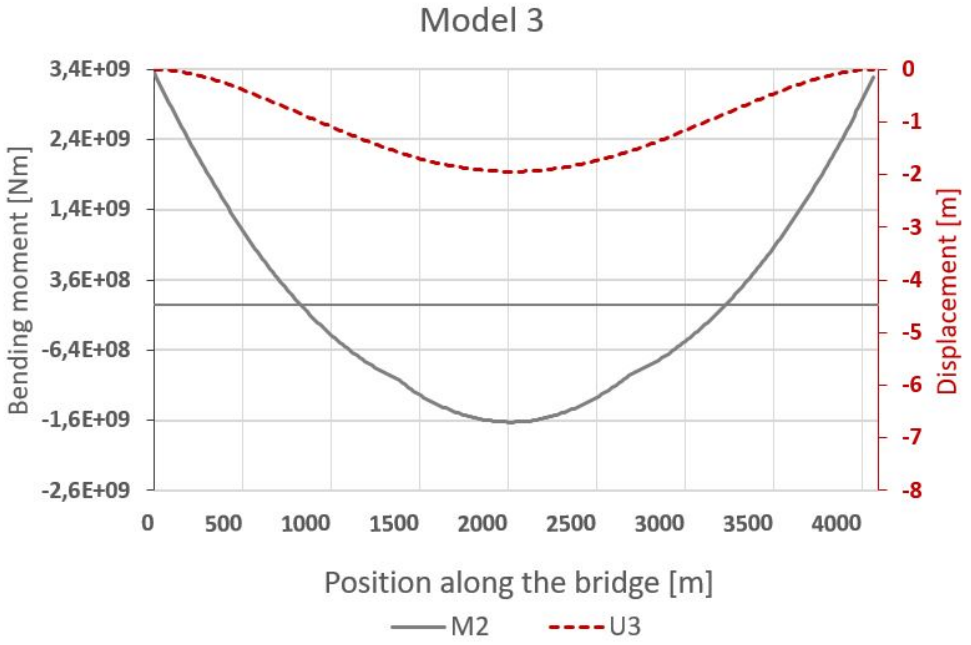

Figure 51: Static response for Model 3 for 50-year static loads

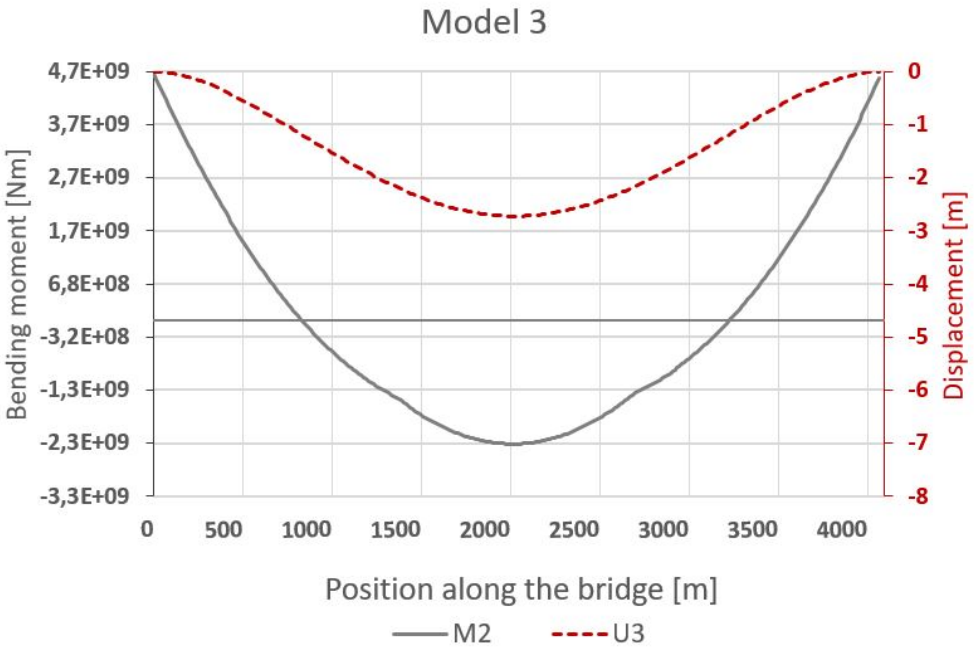

Figure 52: Static response for Model 3 for 100-year static loads

6.3.4 Model 4

In figure 53, the static response for Model 4 are illustrated. Maximum positive and negative bending moment occur at the end-nodes and right before and after the mid-TLP with the values 1.65E9 Nm and -8.31E8 Nm. Model 4 is supported by three TLPs and maximum vertical displacement is located between the TLPs. The longitudinal displacement has its maximum at the mid-point of the model. Largest longitudinal and vertical displacement are -0.866 metres and -2.50 metres.

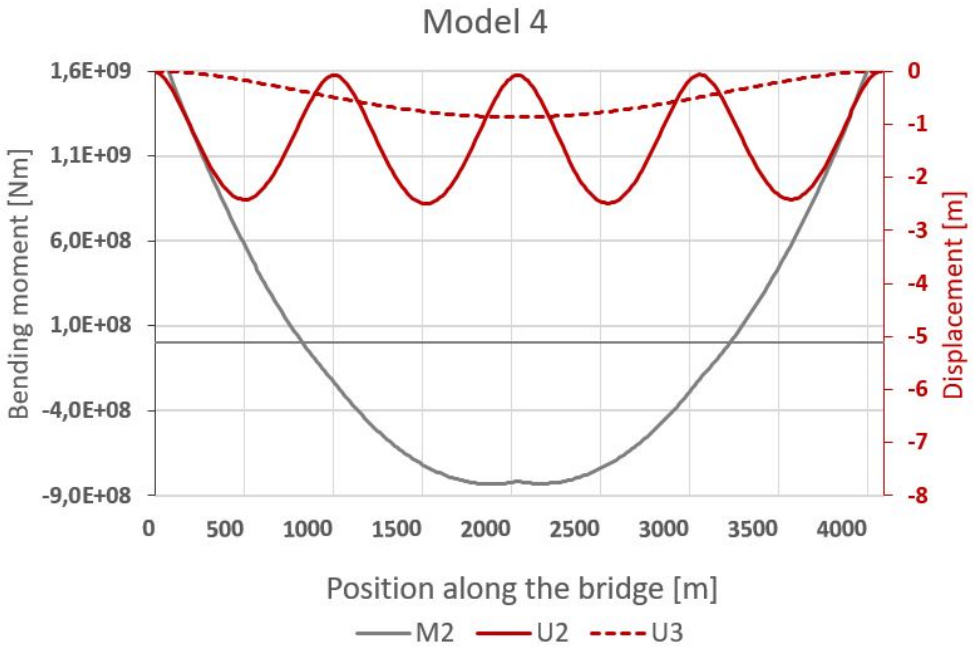

Figure 53: Static loads for Model 4 for 1-year static loads

In figure 54 and figure 55, the static response caused by the 50-year and 100-year static loads, are illustrated. Maximum positive and negative bending moment occurs at the end-node and right before and after the mid-TLP to Model 4. The positive and negative maximum bending moment is 3.06E9 Nm and 1.58E9 Nm for the 50-year static loads, and increases to 4.29E9 Nm and -2.21E9 Nm when the 100-year static loads are applied. The largest longitudinal displacement occurs at the mid-point of Model 4, with a value of -1.63 metre and -2.28 metre for the 50-year and 100-year static load.

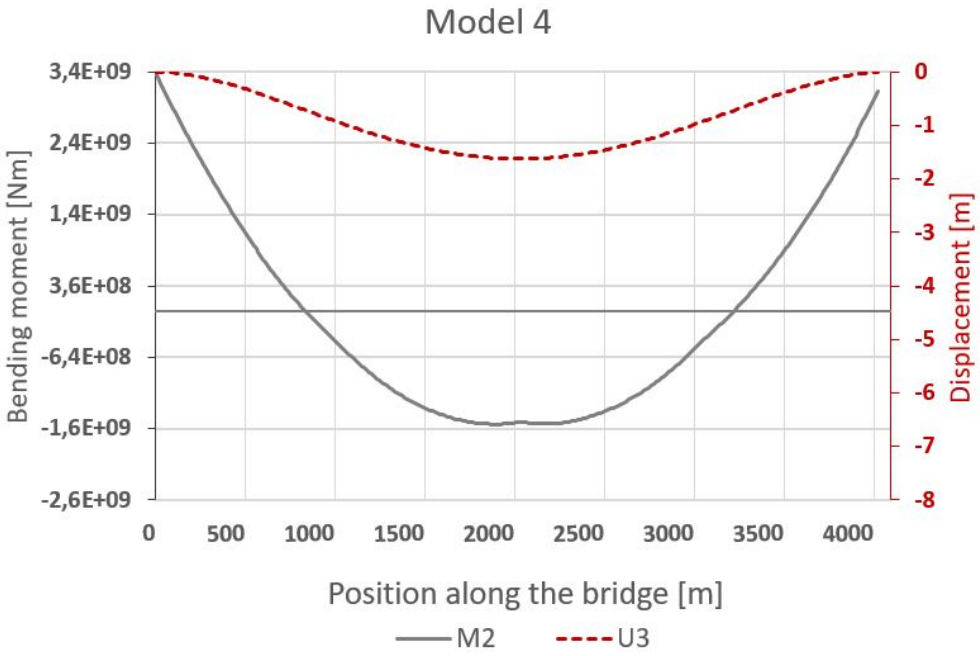

Figure 54: Static response for Model 4 for 50-year static loads

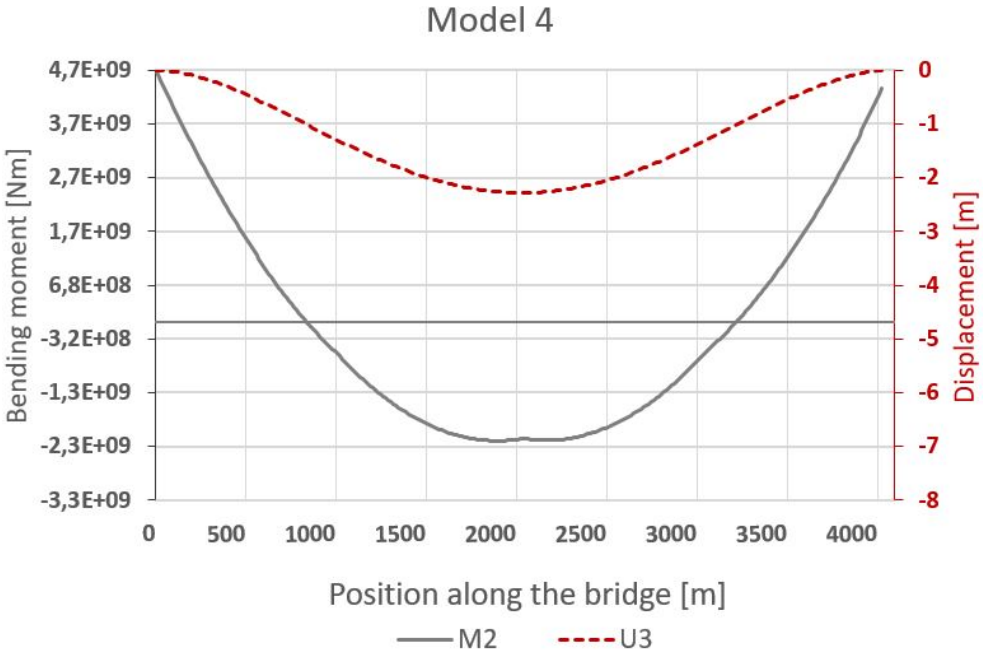

Figure 55: Static response for Model 4 for 100-year static loads

6.4 Dynamic results

In this section, the results from the dynamic analysis is presented. The vertical and longitudinal displacement of the TLPs for a period of 120 seconds for each model, are given. The vertical displacement, heave, results from the applied vertical wave force. When these motions are determined, added mass in heave for the floaters are applied. The longitudinal displacement, sway, develops when a horizontal wave load is applied, and added mass in heave are replaced by added mass in sway. The results from the dynamic analysis is presented for each model. In addition, a dynamic analysis was executed where the first horizontal eigenperiod, T_h, for each model were utilized as the wave period in sway, and the first vertical eigenperiod, T_v, as the wave period in heave. In table 20, the applied horizontal and vertical wave force, $F_{tot,h}$ and $F_{tot,v}$, estimated from the eigenperiods for each models, are given.

Table 20: Horizontal and vertical wave force achieved by the eigenperiods for each model

		Model 1	Model 2	Model 3	Model 4
T_h	[s]	99.00	100.1	98.04	100.3
T_v	[s]	70.42	86.96	68.03	44.44
$F_{tot,h}$	[N]	71 573 135.4	73 393 905.9	69 969 430.9	73 731 532.9
$F_{tot,v}$	[N]	635 041 423	974 733 720	591 750 183	245 563 450

The dynamic response is described for each model, first the heave response, then the sway response. The wave act as a concentrated force applied at the TLPs in vertical or longitudinal direction. The dynamic response during a period of 120 seconds, are presented for the four models. When the first horizontal and vertical eigenfrequency are utilized as the incoming wave, the applied wave load is a 1-year wave.

6.4.1 Model 1

When the dynamic vertical wave load is applied at Model 1, the heave response for TLP1 and TLP2, are seen in figure 56 for the three return periods. The response for TLP1 is illustrated by the red dotted line, and the response for TLP2 is illustrated by the blue line. The wave load is applied for three return periods, where figure 56a, illustrated the heave response when the 1-year dynamic wave load is applied. When the return period is increased to 50-year, the dynamic heave response is seen in figure 56b, and in figure 56c, the 100-year vertical wave force is applied at the TLPs. The shape to the heave displacement when the 1-year dynamic wave load is applied, is similar for both TLPs and the response acts for the same periods after 20 seconds. During the 20 first seconds, the displacement of TLP2 occur before the displacement of TLP1, and the displacement of TLP1 is slightly larger than the displacement of TLP2, which is the red peaks in the figure. For both TLPs, the response increases as the period increases, which can indicate that the maximum displacement have not been, or just been, reached.

The shape and magnitude for the heave response, when the 50-year dynamic wave load is applied, are similar for both TLPs during the first 15 seconds. After 15 seconds, the displacement of TLP2 occur before the displacement of TLP1. Throughout the period of 120 seconds, the heave responses for both TLPs are somewhat periodic, and the response increases for TLP2 while the response for TLP1 has reached its maximum.

When the 100-year dynamic wave load is applied, the response is similar and acts for the same period for both TLPs during the first 10 seconds. After 10 seconds, the displacement of TLP2 occur before the displacement of TLP1, and the response is larger for TLP1 compared to the displacement of TLP2. The displacement of TLP1 reaches its maximum after 80 seconds, and somewhat decreases after its peak is reached. The displacement of TLP2 reaches its maximum after 39 seconds and then decreases until it has nearly no displacement.

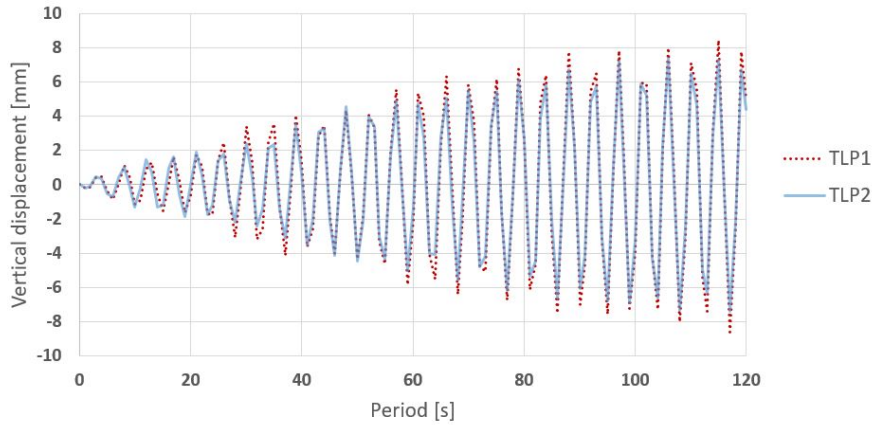

(a) 1-year return period wave

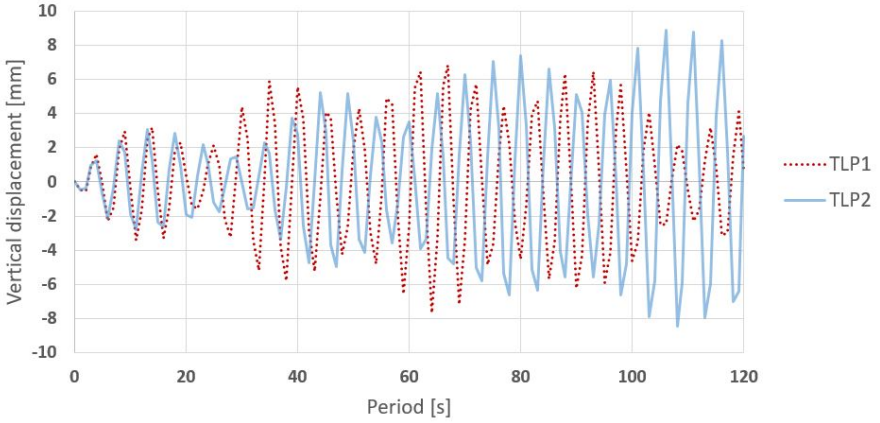

(b) 50-year return period wave

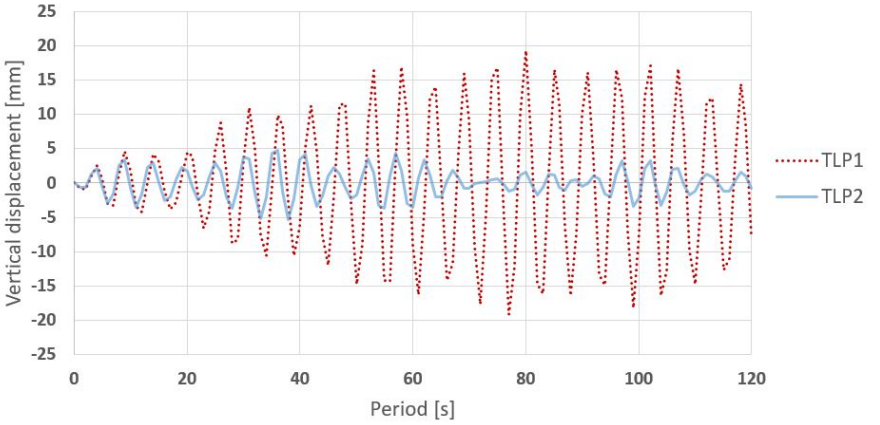

(c) 100-year return period wave

Figure 56: The heave response for Model 1

In figure 57, the sway response for both TLPs are illustrated for three return periods. In figure 57a, the 1-year dynamic horizontal displacement is illustrated, while the responses for both TLPs caused by the 50-year dynamic wave load, is given in figure 57b. The last figure, figure 57c, illustrates the sway response for both TLPs when the 100-year dynamic wave load is applied. The sway response for both TLPs are similar for each return period, as is indicated by no deviation between the sway response in the figures.

The shape and magnitude to the sway response is similar for both TLPs when the 1-year dynamic wave load is applied, and the response acts for the same periods. The positive maximum displacement is slightly larger than the negative maximum displacement, and has a value of 150.94 millimetres. The displacement is periodic, and maximum displacement occur about every 40 seconds.

When the 50-year dynamic wave load is applied, the shape and magnitude to the displacement is similar for both TLPs and the response acts for the same periods. The positive maximum displacement is slightly larger than the negative maximum displacement, and has a value of 267.14 millimetres. The displacement is periodic, and maximum displacement occur about every 40 seconds.

This is also true when the 100-year dynamic wave load is applied. The shape and magnitude to the displacement is similar for both TLPs and the response acts for the same periods. The positive maximum displacement is slightly larger than the negative maximum displacement, and has a value of 324.07 millimetres. The displacement is periodic, and the period between the maximum displacement, is increased from 40 seconds to about 50 seconds.

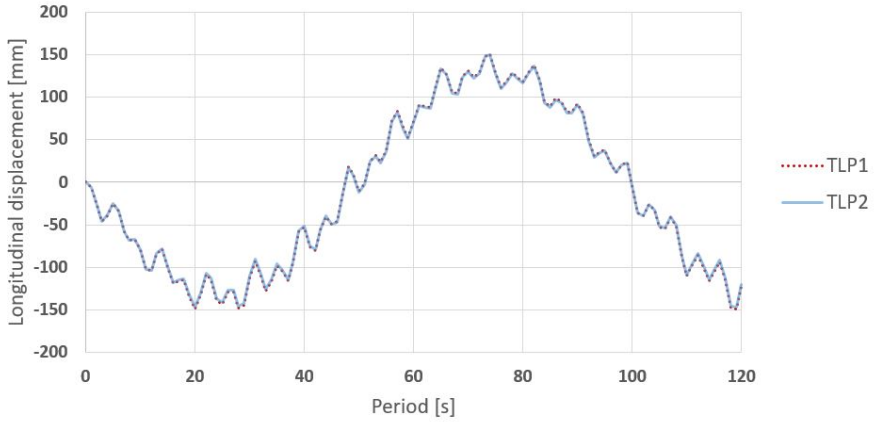

(a) 1-year return period wave

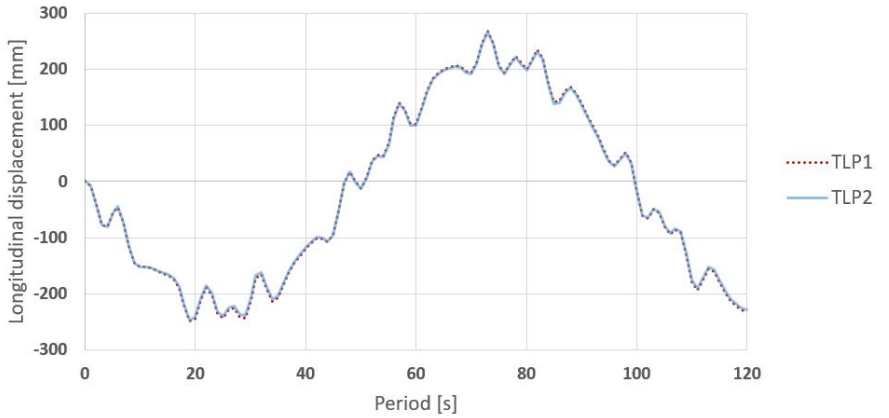

(b) 50-year return period wave

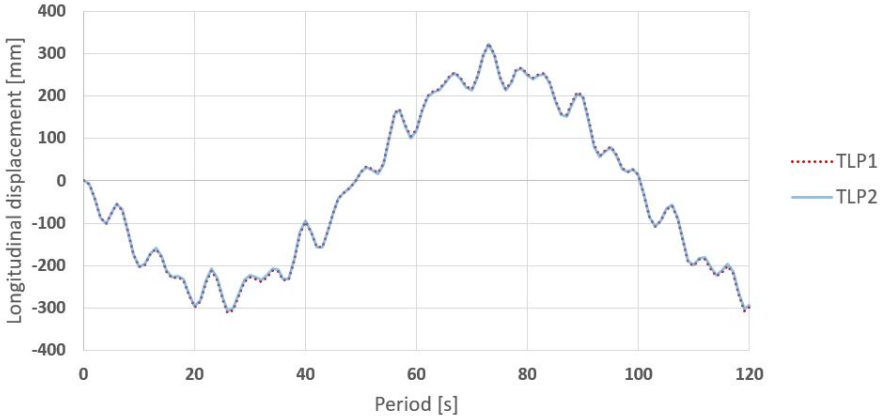

(c) 100-year return period wave

Figure 57: The sway response for Model 1

6.4.2 Model 2

When the dynamic vertical wave load is applied at Model 2, the heave response for TLP1 and TLP2, are seen in figure 58 for the three return periods. The wave load is applied for three return periods, where figure 58a, illustrated the heave response when the 1-year dynamic wave load is applied. When the return period is increased to 50-year, the dynamic heave response is seen in figure 58b, and in figure 58c, the 100-year vertical wave force is applied at the TLPs. When the 1-year dynamic wave load is acting, the response is similar for the TLPs, and acts for the same period during the first 15 seconds. After 15 seconds, the shape and magnitude of TLP1 and TLP2 deviates. The displacement of TLP2 occur before the displacement of TLP1 and the displacement of TLP2 increases as the period increases. The displacement to TLP1 reaches its maximum after 40 seconds, and decreases until the TLP has nearly no displacement. Then, the displacement increases and reaches its new maximum displacement, which is slightly larger than its first maximum.

The response is similar and acts for the same period for both TLPs during the first 15 seconds when the 50-year dynamic wave load is applied at the model. After 15 seconds, the response is largest for TLP1 which reaches its maximum after 40 seconds, where its largest response has a negative value. After the peak is reached, the response decreases until it has nearly zero displacement, and then increases again. The response for TLP2 reaches its first maximum after 40 seconds, then it is slightly reduced, before it increases again, where it reaches its second maximum value, which is its highest value during a period of 120 seconds.

The response for both TLPs are periodic for the 100-year dynamic wave load, and have three peaks during a period of 120 seconds. The response is similar and acts for the same period during the first 5 seconds. As both TLPs are reaching towards its maximum, the displacement of TLP1 is largest, while TLP2 has the largest displacement for the lower responses.

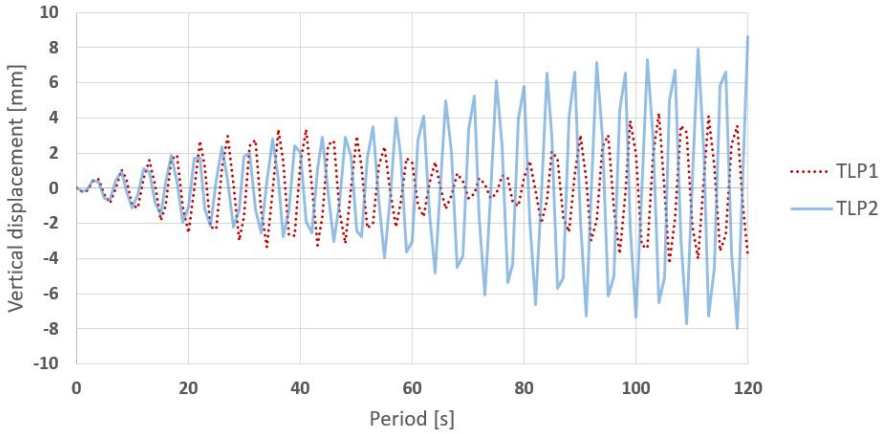

(a) 1-year return period wave

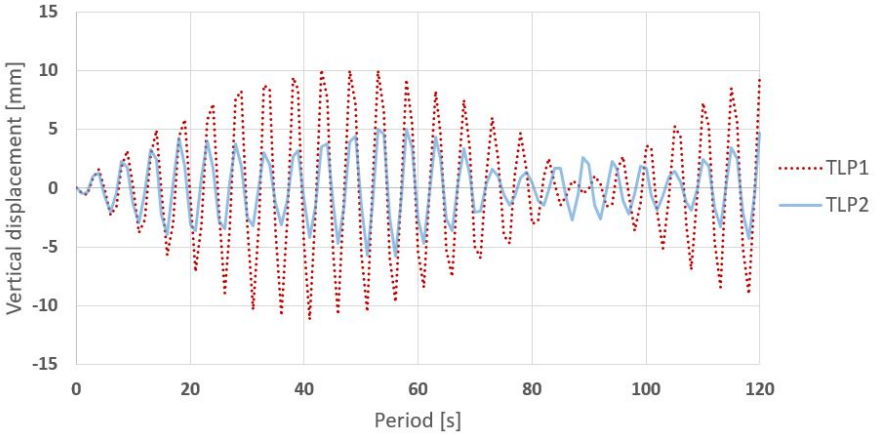

(b) 50-year return period wave

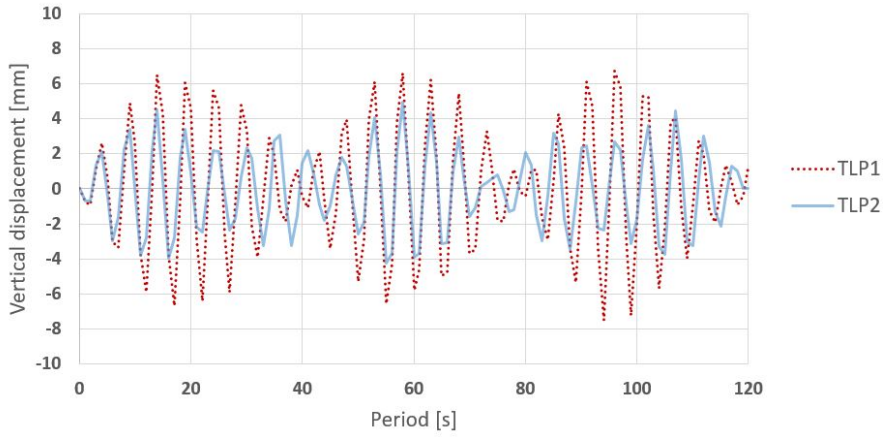

(c) 100-year return period wave

Figure 58: The heave response for Model 2

In figure 59, the sway response for both TLPs are illustrated for three return periods. In figure 59a, the 1-year dynamic horizontal displacement is illustrated, while the responses for both TLPs caused by the 50-year dynamic wave load, is given in figure 59b. The last figure, figure 59c, illustrates the sway response for both TLPs when the 100-year dynamic wave load is applied. The sway response for both TLPs are similar for each return period, as is indicated by no deviation between the sway response in the figures.

The shape and magnitude to the sway response is similar for both TLPs when the 1-year dynamic wave load is applied, and the response acts for the same periods. The positive maximum displacement is slightly larger than the negative maximum displacement, and has a value of 163.42 millimetres. The displacement is periodic, and maximum displacement occur about every 50 seconds.

The shape and magnitude to the displacement is similar for both TLPs when the 50-year dynamic wave load is applied, and the response acts for the same periods. The positive maximum displacement is slightly larger than the negative maximum displacement, and has a value of 257.62 millimetres. The displacement is periodic, and maximum displacement occur about every 40 seconds.

The shape and magnitude to the displacement is similar for both TLPs when the 100-year dynamic wave load is applied, and the response acts for the same periods. The positive maximum displacement is slightly larger than the negative maximum displacement, and has a value of 315.78 millimetres. The displacement is periodic, and maximum displacement occur about every 50 seconds.

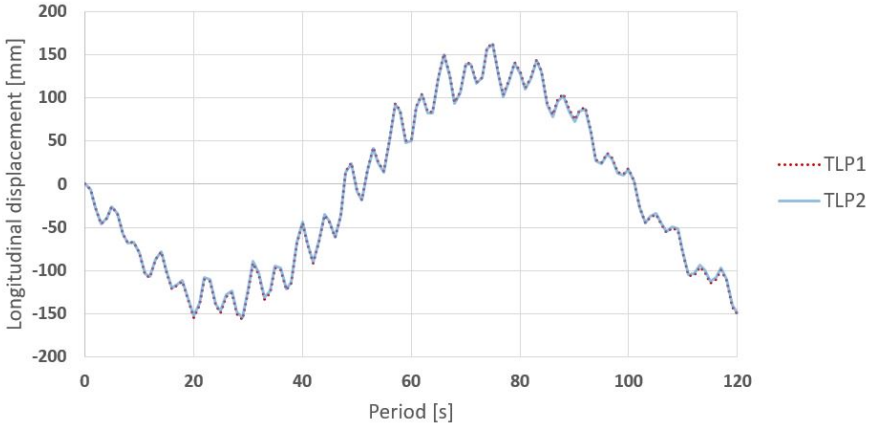

(a) 1-year return period wave

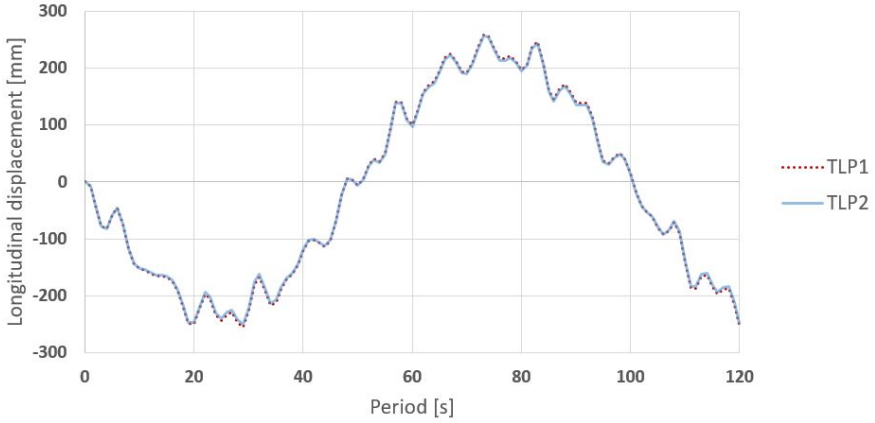

(b) 50-year return period wave

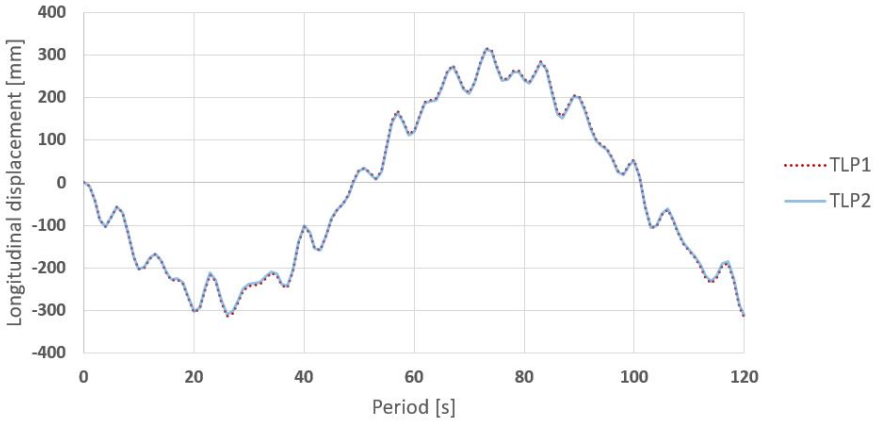

(c) 100-year return period wave

Figure 59: The sway response for Model 2

6.4.3 Model 3

When the dynamic vertical wave load is applied at Model 3, the heave response for TLP1 and TLP2, are seen in figure 60 for the three return periods. The wave load is applied for three return periods, where figure 60a, illustrated the heave response when the 1-year dynamic wave load is applied. When the return period is increased to 50-year, the dynamic heave response is seen in figure 60b, and in figure 60c, the 100-year vertical wave force is applied at the TLPs.

The shape of the heave response is similar for both TLPs when the 1-year dynamic wave load is applied, and the response acts for the same periods after 20 seconds. During the first 20 seconds, the displacement of TLP2 occur before the displacement of TLP1. The response is largest for TLP1 during the first 40 seconds and largest for TLP2 in a period of 40 to 60 seconds. The response for TLP1 is then larger than the response for TLP2 until 72 seconds is reached. The response is almost similar after this, and the largest response reached during a period of 120 seconds, is gained by TLP2.

When the 50-year dynamic wave load is applied, the response is similar for both TLPs during the first 20 seconds. After this, the displacement of TLP2 occur before the displacement of TLP1, and the response is largest for TLP1 throughout a period of 120 seconds. For both TLPs, the response increases as the period increases.

The response for both TLPs is similar and acts for the same period during the first 10 seconds when the 100-year dynamic wave load is applied. After 10 seconds, the displacement of TLP1 increases while the response for TLP2 is steadier. The maximum displacement of TLP1 is reached after 52 seconds. After its peak, the displacement decreases until the displacement is reduced to some millimetre displacement. Then, it increases again.

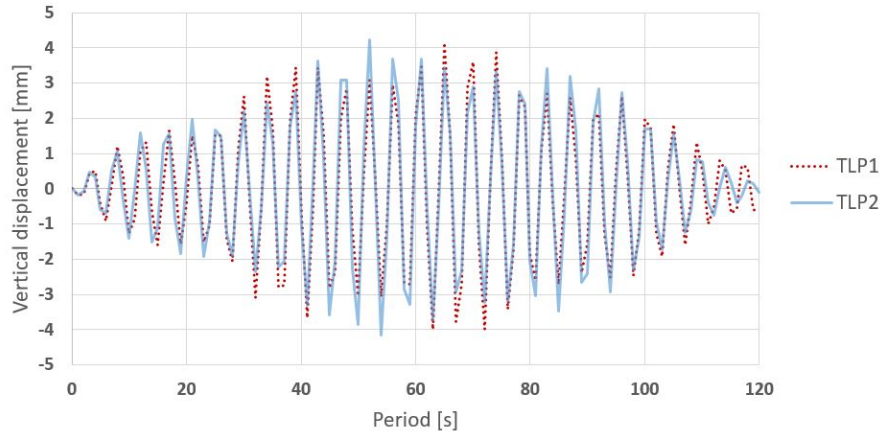

(a) 1-year return period wave

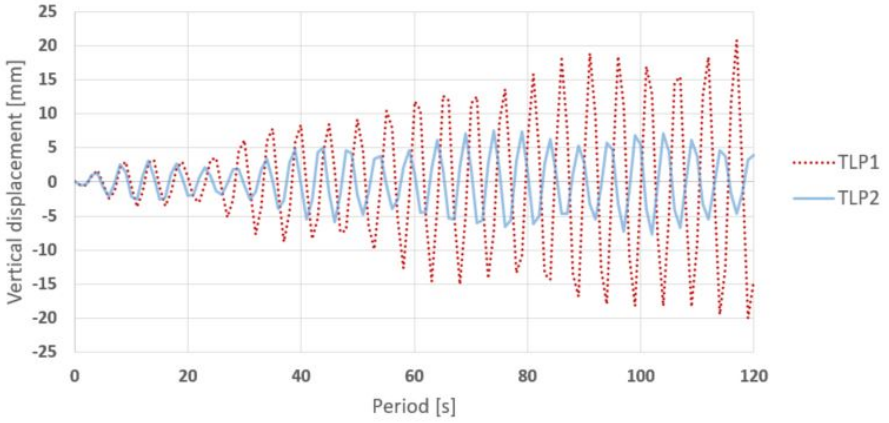

(b) 50-year return period wave

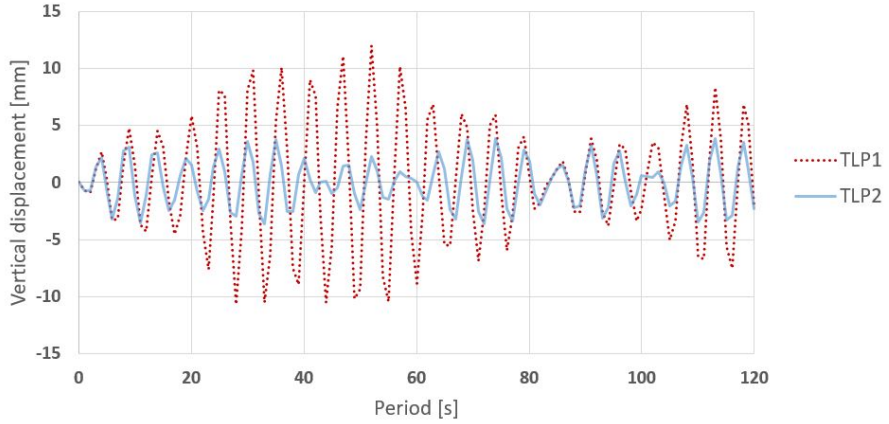

(c) 100-year return period wave

Figure 60: The heave response for Model 3

In figure 61, the sway response for both TLPs are illustrated for three return periods. In figure 61a, the 1-year dynamic horizontal displacement is illustrated, while the responses for both TLPs caused by the 50-year dynamic wave load, is given in figure 61b. The last figure, figure 61c, illustrates the sway response for both TLPs when the 100-year dynamic wave load is applied. The sway response for both TLPs are similar for each return period, as is indicated by no deviation between the sway response in the figures.

The shape and magnitude to the displacement is similar for both TLPs when the 1-year dynamic wave load is applied, and the response acts for the same periods. The positive maximum displacement is slightly larger than the negative maximum displacement, and has a value of 178.42 millimetres. The displacement is periodic, and maximum displacement occur about every 50 seconds.

The shape and magnitude to the displacement is similar for both TLPs when the 50-year dynamic wave load is applied, and the response acts for the same periods. The positive maximum displacement is slightly larger than the negative maximum displacement, and has a value of 312.55 millimetres. The displacement is periodic, and maximum displacement occur about every 40 seconds.

The shape and magnitude to the displacement is similar for both TLPs when the 100-year dynamic wave load is applied, and the response acts for the same periods. The positive maximum displacement is slightly larger than the negative maximum displacement, and has a value of 377.44 millimetres. The displacement is periodic, and maximum displacement occur about every 50 seconds.

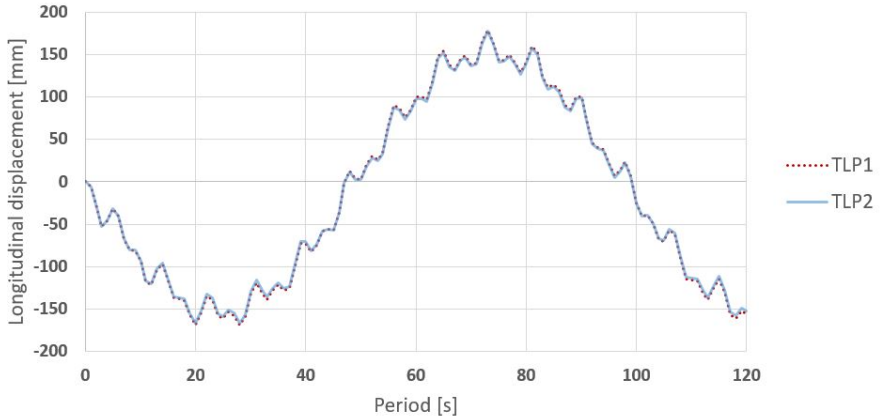

(a) 1-year return period wave

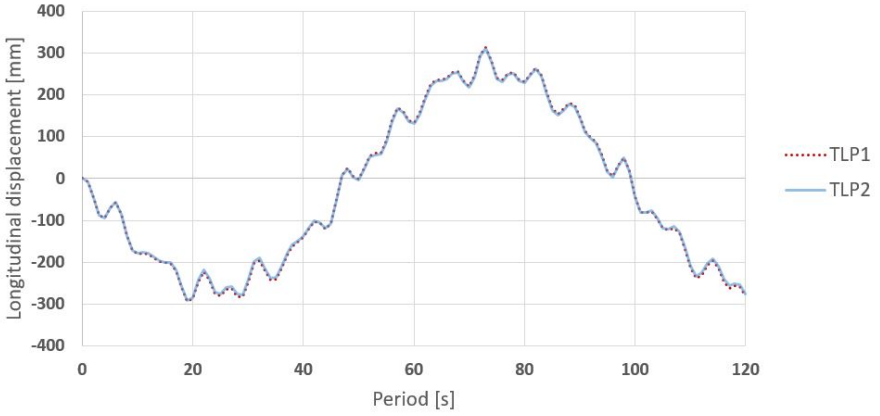

(b) 50-year return period wave

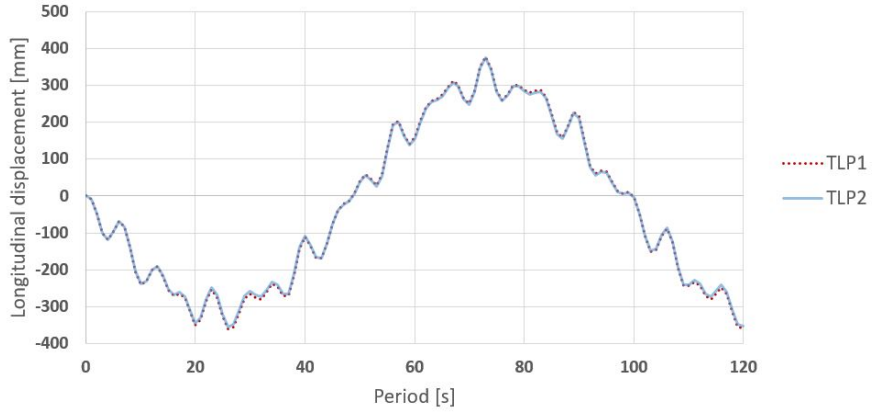

(c) 100-year return period wave

Figure 61: The sway response for Model 3

6.4.4 Model 4

When the dynamic vertical wave load is applied at Model 4, the heave response for the TLPs, are seen in figure 62 for three return periods. The wave load is applied for three return periods, where figure 62a, illustrated the heave response when the 1-year dynamic wave load is applied. When the return period is increased to 50-year, the dynamic heave response is seen in figure 62b, and in figure 62c, the 100-year vertical wave force is applied at the TLPs. When the 1-year dynamic wave load is applied, the shape and magnitude is similar during the first 10 seconds. The response for $TLP1^4$ has three peaks for 120 seconds and nearly no displacement between the peaks, while the $TLP2^4$ is steadier, and have a regular displacement throughout the period of 120 seconds. The response for $TLP3^4$ is more random. In figure 62a, the response seems chaotic, yet the response is for very small displacement, all TLPs have a smaller displacement than 1.5 millimetres.

When the 50-year dynamic wave load is applied, the shape and magnitude is similar during the first 20 seconds. After 20 seconds, the response occurs for $TLP3^4$ before the other TLPs. It reaches its maximum after 66 seconds, before it decreases again. After 90 seconds, it has nearly no displacement, but for a period between 100 and 120 seconds, it has some displacement. The displacement of $TLP2^4$ increases towards its first maximum which occurs after 44 seconds. After the first maximum, the displacement decreases until it has nearly no displacement, and then starts to increase again. The displacement for $TLP1^4$ increases as the period increases. When the 100-year dynamic wave load is applied, the shape and magnitude are similar during the first 20 seconds. After 20 seconds, the response occurs for $TLP3^4$ before the other TLPs. The response for $TLP1^4$ and $TLP3^4$ are close with some deviation. After the first maximum, which occurs at 30 seconds, the response decreases some, before the response for these TLPs increases again. The second maximum occurs about after 90 seconds, before the response decreases some. The displacement for $TLP2^4$ increases as the period increases.

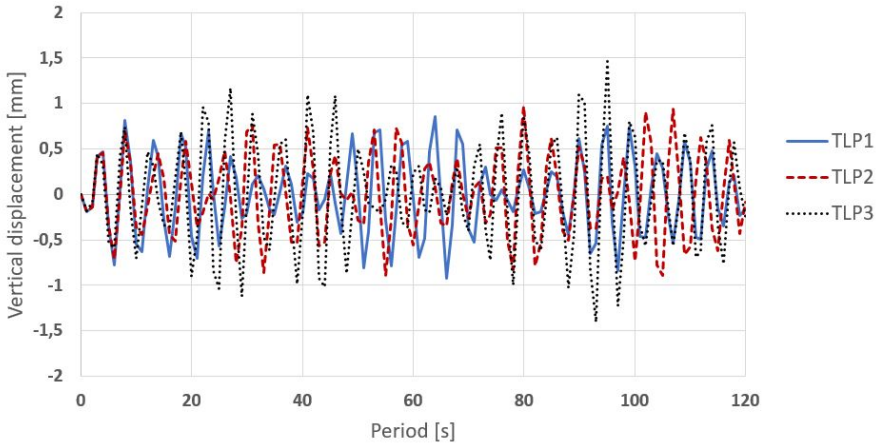

(a) 1-year return period wave

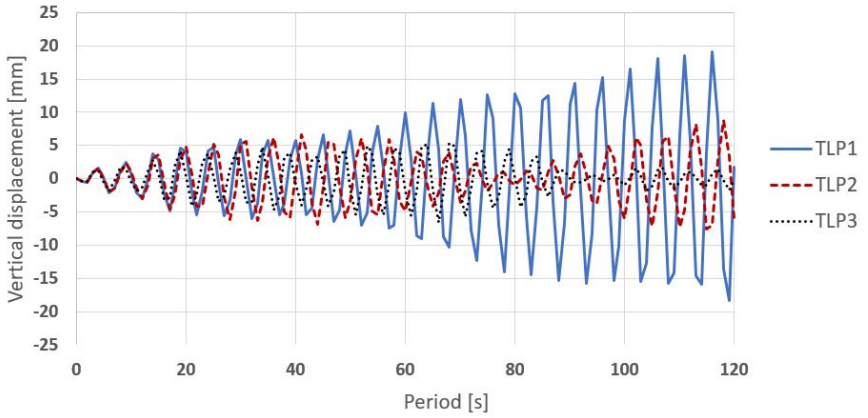

(b) 50-year return period wave

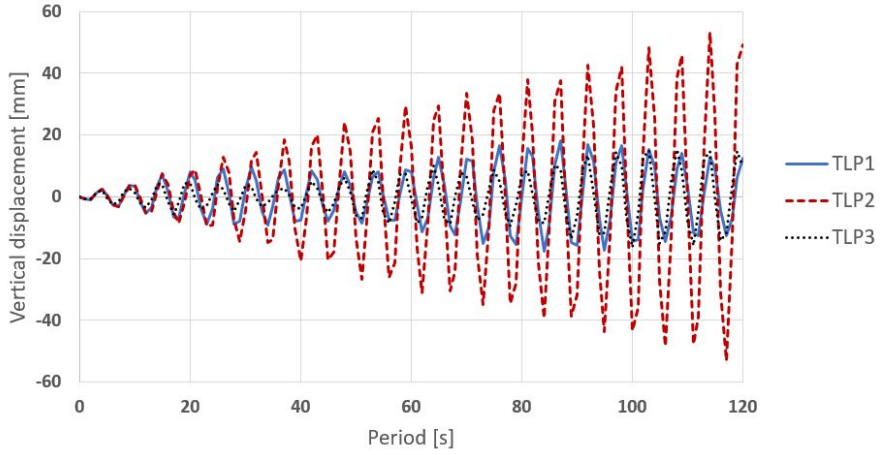

(c) 100-year return period wave

Figure 62: The heave response for Model 4

In figure 63, the sway response for all TLPs are illustrated for three return periods. In figure 63a, the 1-year dynamic horizontal displacement is illustrated, while the responses caused by the 50-year dynamic wave load is given in figure 63b. The last figure, figure 63c, illustrates the sway response for the TLPs when the 100-year dynamic wave load is applied.

The shape and magnitude to the sway response is similar for TLP1[4] and TLP3[4] when the 1-year dynamic wave load is applied, and the response acts for the same periods. The negative maximum displacement is slightly larger than the positive maximum displacement, and has a value of -221.45 millimetres. The response is periodic, and maximum displacement occur about every 30 seconds. This is also true for TLP2[4] which has a maximum value of -292.25 millimetres, and maximum displacement occur about every 44 seconds.

When the 50-year dynamic wave load is applied, the shape and magnitude to the sway response is similar for TLP1[4] and TLP3[4] and the response acts for the same periods. The negative maximum displacement is larger than the positive maximum displacement, and has a value of -317.21 millimetres. The response is periodic, and maximum displacement occur about every 55 seconds. This is also true for TLP2[4] which has a maximum value of -452.91 millimetres, and maximum displacement occur about every 55 seconds.

When the 100-year dynamic wave load is applied, the shape and magnitude to the sway response is similar for TLP1[4] and TLP3[4] and the response acts for the same periods. The negative maximum displacement is larger than the positive maximum displacement, and has a value of -280.22 millimetres. The response is periodic, and maximum displacement occur about every 50 seconds. The largest displacement for TLP2[4] is a positive value and has the value of 479.37 millimetres, and maximum displacement occur about every 60 seconds.

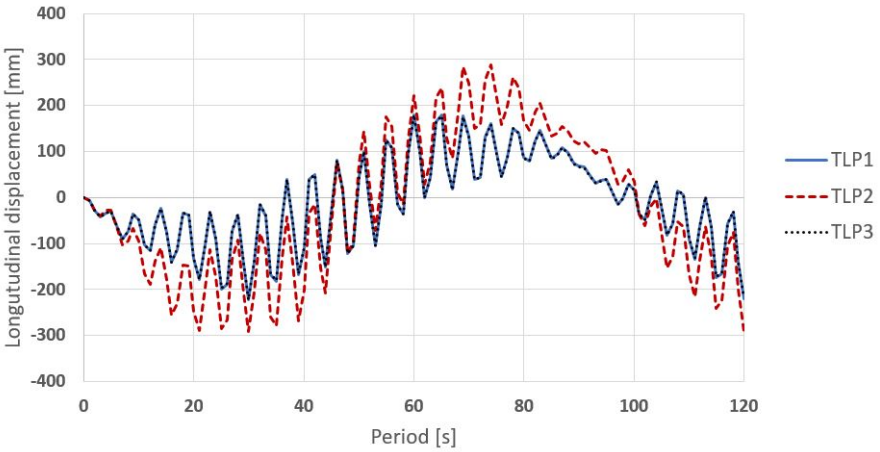

(a) 1-year return period wave

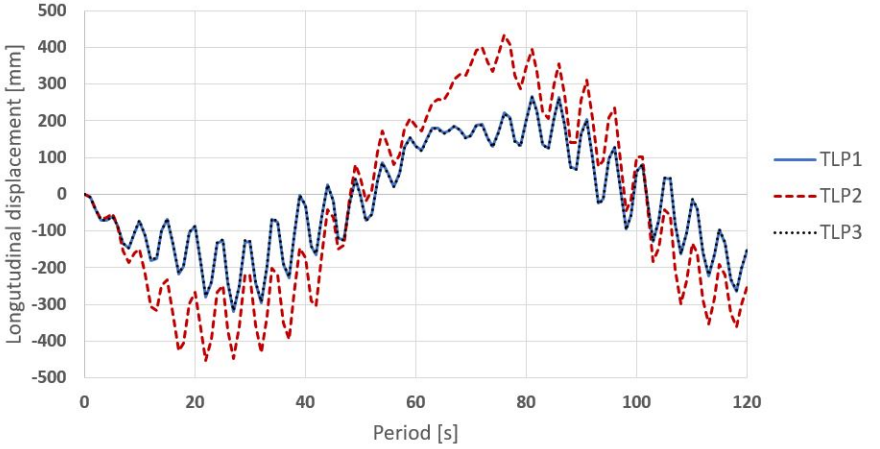

(b) 50-year return period wave

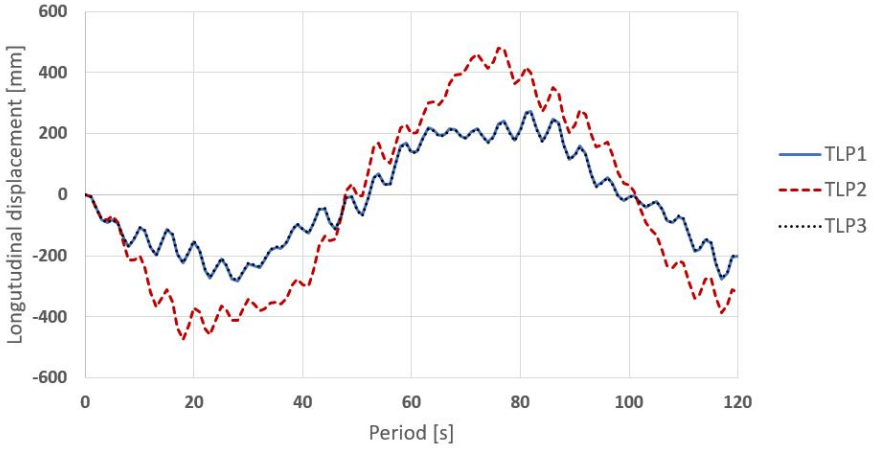

(c) 100-year return period wave

Figure 63: The sway response for Model 4

6.4.5 Eigenperiod utilized as the period for the incoming wave

In this section, the first obtained horizontal and vertical eigenfrequency, are utilized as the frequency of the incoming wave, applied in horizontal and vertical direction, respectively. This has been performed for each model since the eigenfrequency achieved, are different for every model. The magnitude for longitudinal and vertical displacement is in metres, since the applied load causes a dramatic increase in the displacements.

Model 1

When the eigenperiod is utilized as the period for the incoming wave, the response of TLP1 and TLP2 for Model 1, are seen in figure 64. The heave response is seen in figure 64a and sway response is seen in figure 64b.

According to figure 64a, the heave response is larger for TLP1 compared to TLP2, and the response occur for TLP1 before the displacement of TLP2 occur. The displacement of the TLPs are periodic, and maximum displacement occur about every 40 seconds. For both TLPs, the displacement changes its value dramatically every other second. During a period of 120 seconds, the response for both TLPs reaches a maximum three times.

The sway response indicates that the displacement of both TLPs are similar because of no deviation between the sway displacement for the TLPs in the figure. The first peak occurs after 38 seconds, while the next after 74 seconds, and the third after 105 seconds, which gives an increasing period between the peaks. In addition, the sway response increases as the period increases.

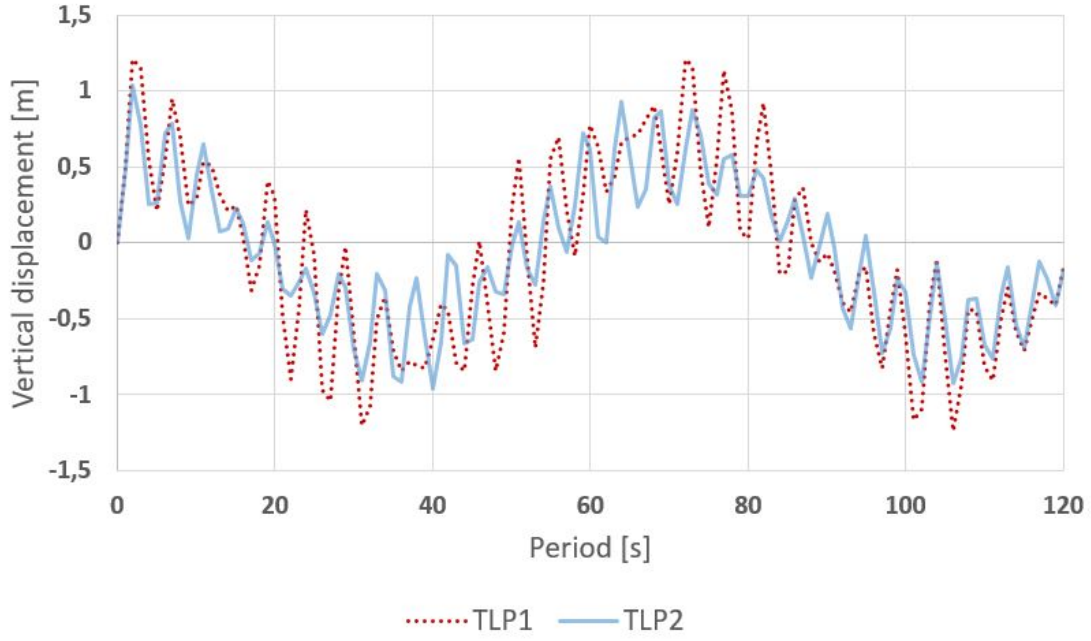

(a) Heave response

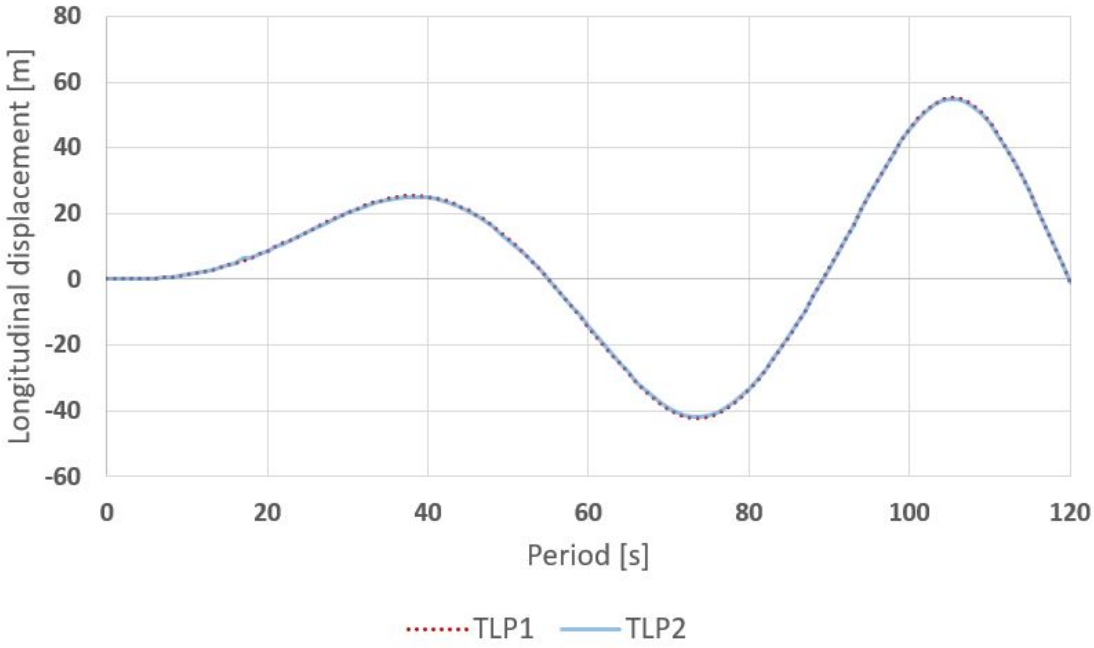

(b) Sway response

Figure 64: The dynamic response for Model 1

Model 2

When the eigenperiod is utilized as the period for the incoming wave, the response of TLP1 and TLP2 for Model 2, are seen in figure 65. The heave response is seen in figure 65a and sway response is seen in figure 65b.

According to figure 65a, the heave response is larger for TLP1 compared to TLP2, and the response occur for TLP1 before the displacement of TLP2 occur. The displacement of the TLPs are periodic, and maximum displacement occur about every 45 seconds. For both TLPs, the displacement changes its value dramatically every other second, yet they follow the periodic path. During a period of 120 seconds, the response for both TLPs reaches a maximum three times.

The sway response indicates that the displacement of both TLPs are similar because there is no deviation between the sway displacement for the TLPs in the figure. The first peak occurs after 42 seconds, while the next after 79 seconds, and the third after 113 seconds, which gives an increasing period between the peaks. In addition, the sway response increases as the period increases.

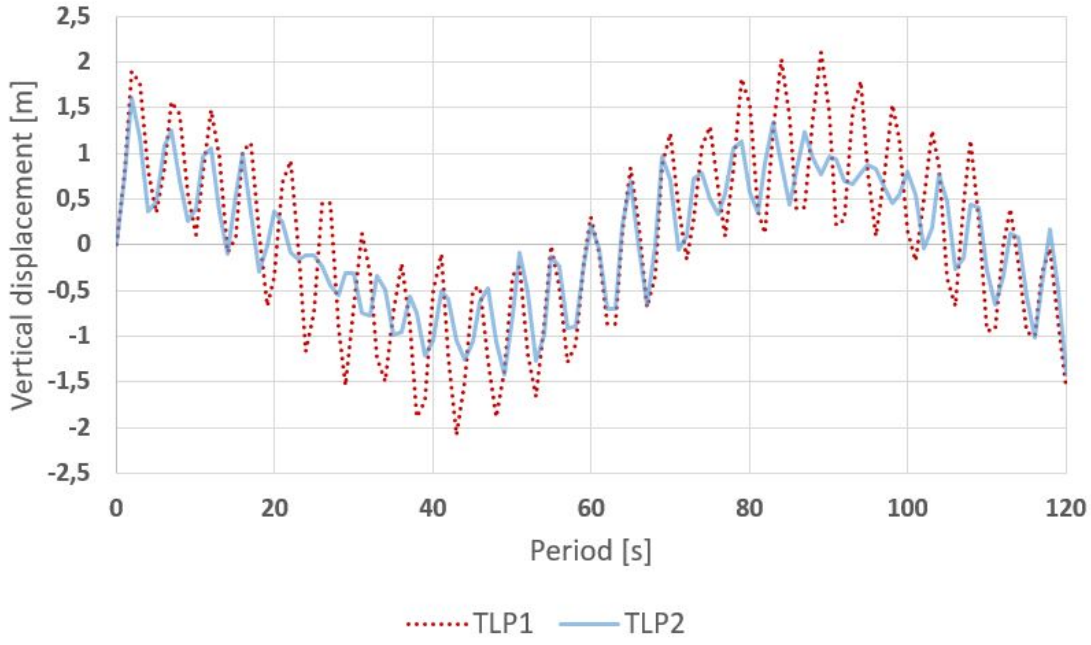

(a) Heave response

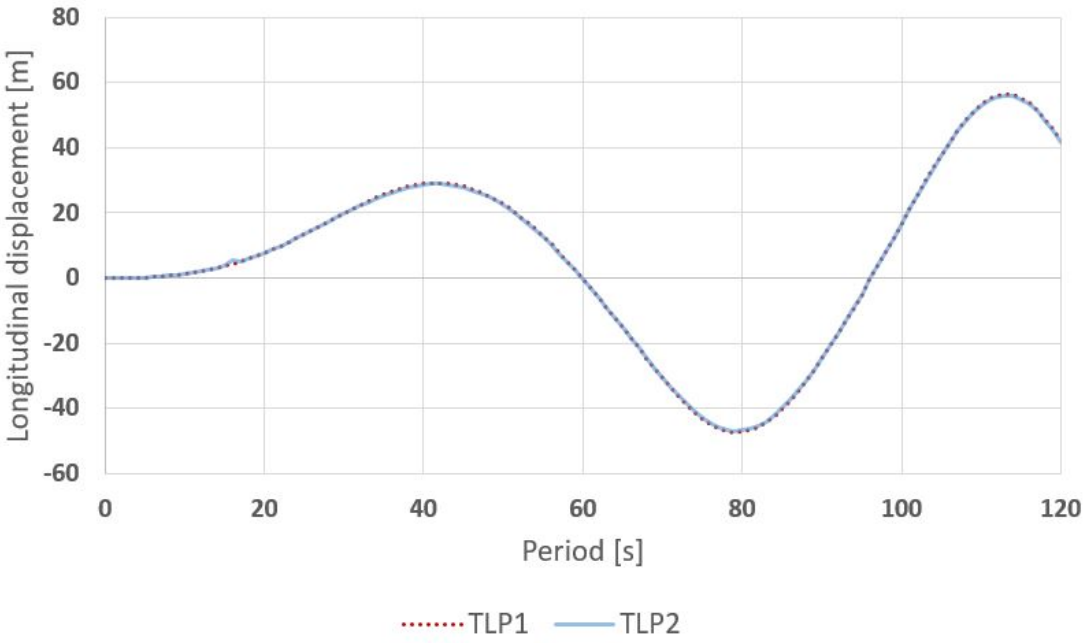

(b) Sway response

Figure 65: The dynamic response for Model 2

Model 3

When the eigenperiod is utilized as the period for the incoming wave, the response of TLP1 and TLP2 for Model 3, are seen in figure 66. The heave response is seen in figure 66a and sway response is seen in figure 66b.

According to figure 66a, the heave response is larger for TLP1 compared to TLP2, and the response occur for TLP1 before the displacement of TLP2 occur. The displacement of the TLPs are periodic, and maximum displacement occur about every 30 seconds. For both TLPs, the displacement changes its value dramatically every other second, yet they follow the periodic path. During a period of 120 seconds, the response for both TLPs reaches a maximum four times which is an increase compared to the heave response for Model 1 and Model 2.

The sway response indicates that the displacement of both TLPs are similar because there is no deviation between the sway displacement for the TLPs in the figure. The first peak occurs after 37 seconds, while the next after 71 seconds, and the third after 102 seconds, which gives a steady period between the peaks. The sway response increases as the period increases.

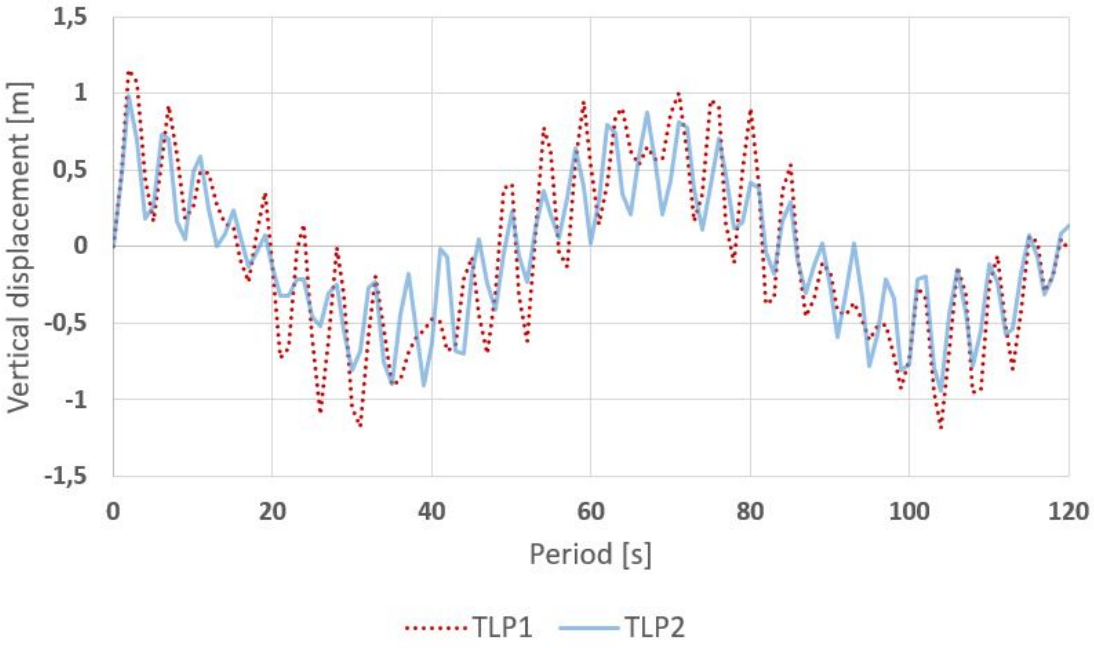

(a) Heave response

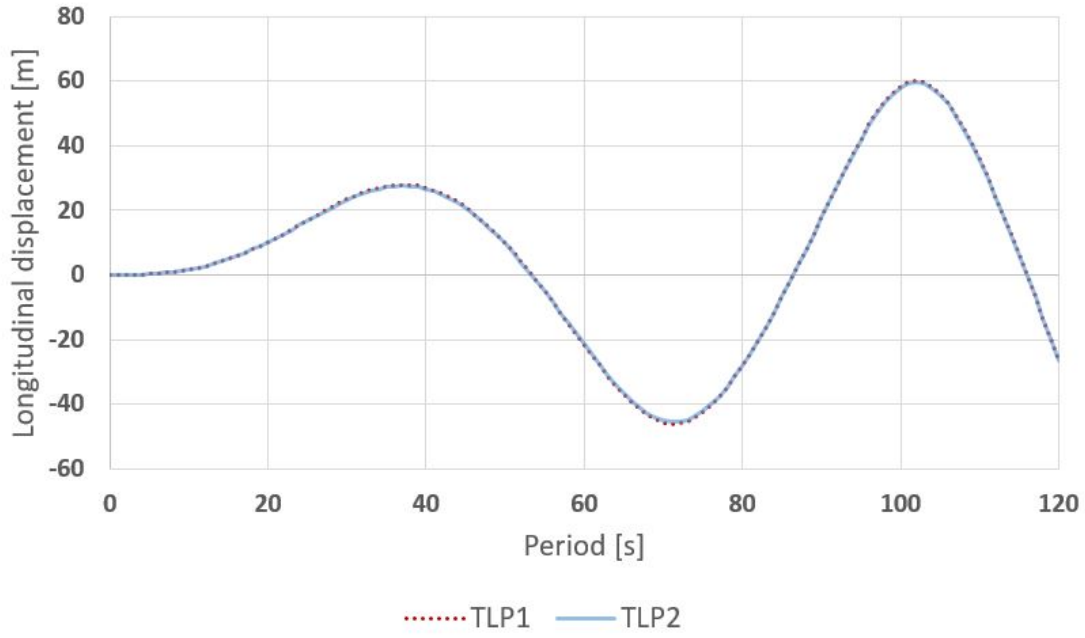

(b) Sway response

Figure 66: The dynamic response for Model 3

Model 4

When the eigenperiod is utilized as the period for the incoming wave, the response of TLP1^4, TLP2^4 and TLP3^4 for Model 4, are seen in figure 67. The heave response is seen in figure 67a and sway response is seen in figure 67b.

According to figure 67a, the heave response is larger for TLP2^4 compared to the other TLPs. The displacement of the TLPs are periodic, and maximum displacement occur about every 20 seconds. For the TLPs, the displacement changes its value dramatically every other second, yet they follow the periodic path. During a period of 120 seconds, the response for the TLPs, reaches a maximum six times. The maximum value is smaller than the maximum heave response for the previous models.

The sway response indicates that the displacement of TLP1^4 and TLP3^4 are similar because of no obviously deviation for the sway displacement between the TLPs in the figure. The first peak for these TLPs occurs after 30 seconds, while the next after 62 seconds. After 80 seconds, there are no displacement for nearly 20 seconds, before the response increases again, where the sway response increases as the period increases. For TLP2^4, the first maximum is reached after 29 seconds for a higher displacement than the other two. The second maximum, reached after 59 seconds, is a higher value than the end-TLPs achieves. The response is equal to zero for the same period as the end-TLPs, and starts to increase after 100 seconds, and it seems like TLP2^4 reaches an additional maximum value.

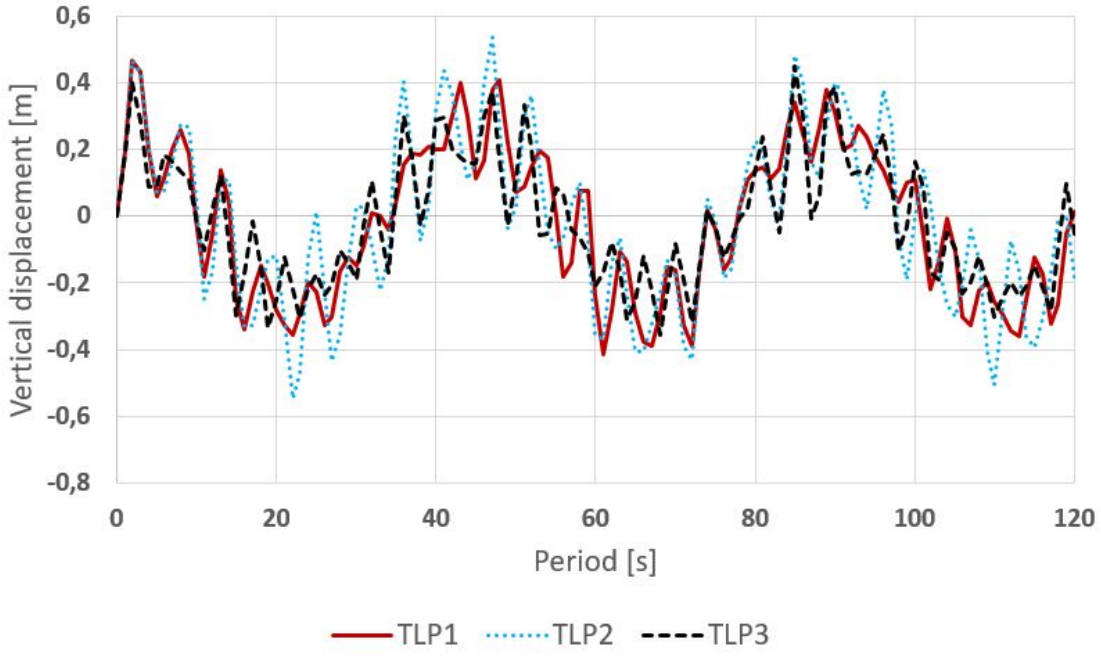

(a) Heave response

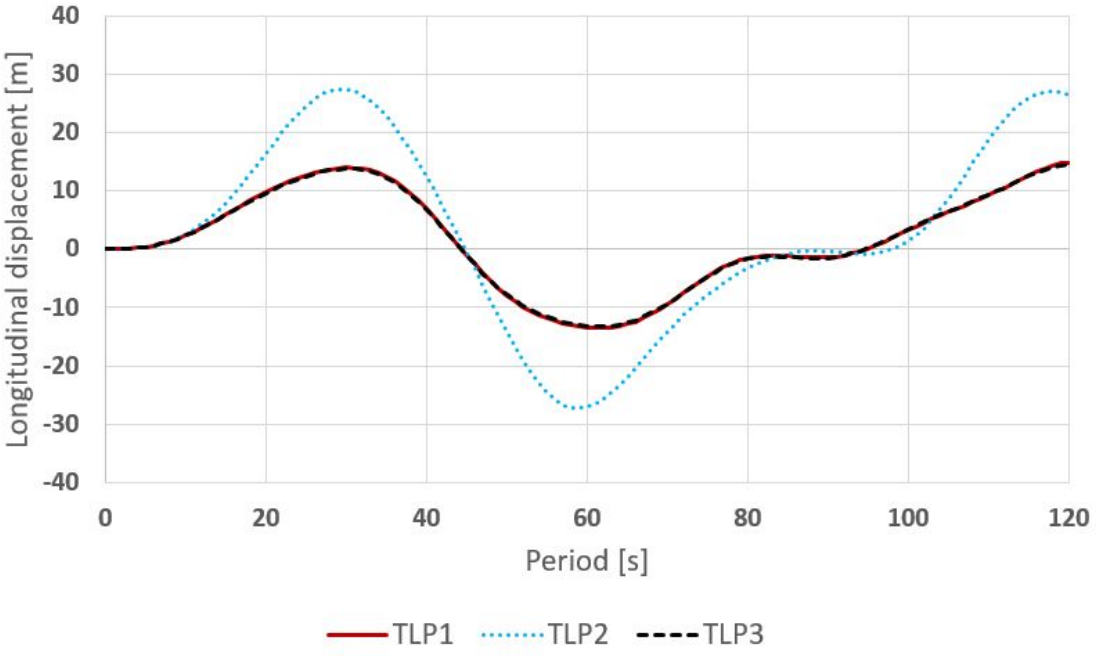

(b) Sway response

Figure 67: The dynamic response for Model 4

7 Discussion

Assumptions made throughout the thesis and the results obtained, are discussed in this chapter. Assumptions and simplifications made when determining the loads, simplification of the model and added mass and damping to the floater, are discussed in section 7.1. Further, results for the four models are discussed and compared. The results for the eigenvalue analysis are found in section 7.2, while the results for the static and dynamic analysis are found in section 7.3 and 7.4, respectively.

7.1 Applied loads and floater

The applied loads are illustrating some of the acting loads on a floating bridge. To be able to execute the analyses, simplifications were performed when determining the different loads, and even though the simplifications are reasonable, the analyses will be affected. Further, it was chosen to only include current, traffic, waves, and wind. The applied current load was determined at the sea surface, which means that the effect from the downward current load at the tethers are neglected. If the current load was applied as a distributed load along the tethers, a higher current load would act, which would cause a larger displacement in longitudinal direction.

The applied traffic load in the static analysis is significantly higher than the value utilized by the NPRA. The reason for this is that Eurocode 1 has been utilized in this thesis, while NPRA has utilized the N400 handbook for load calculations. Different understanding on how to calculate the load might also increase the gap. In this thesis, conservatism was always assumed, which results in considerable stiff, and thereby heavy, models. To resist the traffic load and have a maximum displacement less than -5.12 metres, which is a suggested displacement limit, the cross-section for the models have nearly a thickness of 1 metre.

The applied traffic load includes only the uniformly distributed traffic load since the concentrated traffic load is neglected. This was decided since the traffic load was applied as a static load and the concentrated traffic load is a fluctuating load that would move along the bridge during time. The pedestrian load was determined by assuming a value, instead of utilizing Eurocode 1 or N400. According to Eurocode 1 and N400, the uniformly distributed load is estimated to be 15 kN/m and 6 kN/m, respectively. The applied pedestrian load in this thesis was set to 2 kN/m, since the given pedestrian loads from the Eurocode 1 and N400 were considered as unrealistically high. Because of the length of the bridge, it is unlikely to have a fully loaded pedestrian lane in addition to fully loaded traffic lanes.

When calculating the wave load, needed data, such as the wave period and wave height, were adopted from Sognefjorden and then slightly increased due to the location of Bjørnafjorden. The location is probably more exposed to waves than Sognefjorden, but still sheltered, and the chosen values are considered as reasonable. Where the first horizontal and vertical eigenperiods were utilized as the wave period for the incoming wave, the applied wave load were significant large. The first horizontal eigenperiods were about 100 seconds and the first vertical eigenperiods varied from 45 seconds to 87 seconds. This means that the wave period has increased considerably, from 4 seconds which was considered a likely period. The eigenperiod utilized as the wave period is unlikely to occur. In addition, the waves were only applied as harmonic incoming waves, which is also a simplification.

Current and wind are assumed to be static loads, which might be a good assumption for the current, but not for the wind load. By applying the wind as a dynamic load, the response in the dynamic analysis would increase.

When calculating the value of the spring element, which represents the tethers, linear stiffness was assumed as a simplification, meaning that it is assumed no setdown of the floater. For a small setdown, which is true for deep water, the

equations for non-linear stiffness become similar as for linear stiffness. The set-down for the floaters in the models are estimated to be minor, which means that this assumption will not cause any major error in the analyses. The boundary conditions at the end-nodes were assumed to be fixed in all degrees of freedom. If this simplification is incorrect, it will affect the analyses because a symmetry would be introduced for the model. In the simplified models, structural design at the end-nodes, such as the pillars, which would introduce extra boundary conditions, are neglected.

The magnitude of the obtained added mass was compared to available data from NPRA to judge if they were representative. In heave, which was the only available added mass from NPRA, the behaviour was similar. The added mass in heave obtained by NPRA and from this thesis, are given in figure 68a and figure 68b.

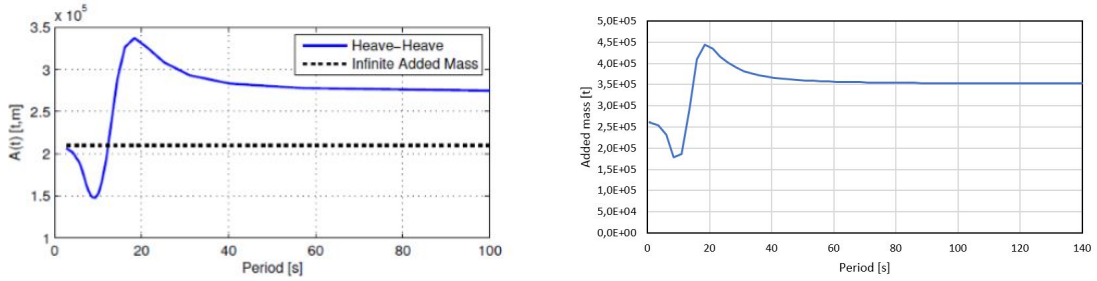

(a) Achieved by NPRA[21]

(b) Achieved from HydroD

Figure 68: Added mass in heave for the concrete floater

Although the added mass is frequency-dependent, it was applied in this thesis as a constant to avoid the need for updates throughout the analyses. Since convergence was obtained for high periods and it is expected that the models will have small eigenfrequencies, the converged values were applied as the added mass for heave and sway. This assumption might cause some error during the analyses, especially for low periods where the added mass has a significant value.

Damping in surge, given by NPRA and achieved through the analysis performed in this thesis, are given in figure 69a and figure 69b. According to the figures, the shape and magnitude are similar, with expectance of the first peak around 5 seconds in figure 69a. It seems like a larger period-interval have been utilized when the damping in this thesis were determined, which might explain why the first peak was not spotted.

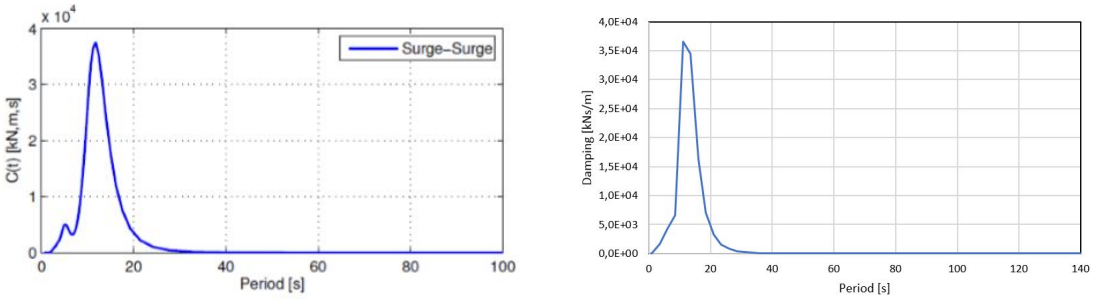

(a) Achieved by NPRA[21] (b) Achieved from HydroD

Figure 69: Damping in surge for the concrete floater

Since the damping is low outside the peak region, and nearly zero for higher periods, no damping was applied during the analyses. By including damping, the motions would be reduced since the damping would act like a mooring system, and this would have been specially noted during the dynamic analyses. Neglecting the damping of the floater will cause error for low periods.

7.2 Eigenvalue analysis

To have the same relation between the stiffness and mass as the proposed crossing, an eigenvalue analysis was performed for each model. The first two horizontal eigenvalues for the crossing proposed by NPRA and for all models, are given in table 21. For the first and second eigenfrequency, all models have a higher value, which indicates either that the stiffness is higher or that the mass and added mass

is smaller compared to NPRA, or a combination of these.

Table 21: The two first horizontal eigenvalues obtained by NPRA and for all models[24]

	NPRA	Model 1	Model 2	Model 3	Model 4
ω_1 [Hz]	9.09E-3	1.01E-2	9.99E-3	1.02E-2	9.97E-3
ω_2 [Hz]	1.67E-2	2.43E-2	2.40E-2	2.40E-2	2.42E-2

The deviation for the first horizontal eigenfrequency is slightly higher than the deviation for the second eigenfrequency. This might be a result of the constant applied added mass. By applying a constant added mass, the error will increase as increasing eigenfrequencies are determined, because of the peak in the added mass. Another component that causes the deviation, is the stiffness of the models. The height of the cross-sections to the models are higher compared to the cross-section created by NPRA. Also, since the cross-section is only a box, and no stiffeners and girders are included, the thickness was increased to nearly a metre in order to be capable to resist the static loads. By increasing the height and thickness of the cross-section, not only do the mass of the bridge increases, but the stiffness of the bridge increases. This will have a larger impact on the eigenvalue analysis than the constant added mass.

The deviation within the models are minor for both eigenfrequencies, but Model 3 has the largest deviation for the first eigenfrequency, while Model 1 has the largest deviation for the second eigenfrequency. Model 4 has the smallest deviation for the first eigenfrequency, followed by Model 2. For the second eigenfrequency, Model 2 and Model 3 are closest to the second eigenfrequency obtained by NPRA. Since Model 2 has a reduced cross-section height compared to the other models, it is more similar to the model created by NPRA. This means that by reducing the height of the cross-section, the reduction is larger for the stiffness than for the mass, which results in smaller eigenfrequencies.

From this analysis, the mass of the models was determined by changing the characteristics of the cross-section. The mass of the models is significantly higher than the original bridge, which might cause some difficulties with keeping the bridge floating, only supported by the floaters. The increased mass is mostly caused by applying a simplified cross-section, which should offer the same stiffness as a more complex cross-section. This causes a larger thickness for the entire bridge.

7.3 Static analysis

Largest vertical displacement arises when the traffic load is acting. The vertical displacement along the bridge for the four models, are given in figure 70.

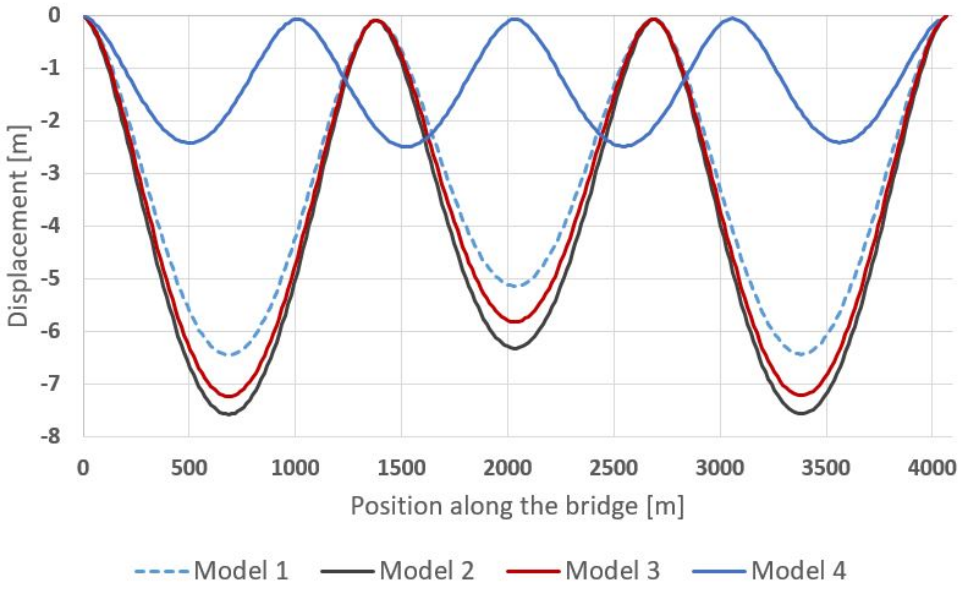

Figure 70: Vertical displacement

As a suggested displacement limit, the bridge length divided by 800 is the maximum allowable vertical displacement, which for these models are approximately -5.12 metres. To resist the traffic load by having a vertical displacement beneath this limit, the model's stiffness was adjusted. The height of the bridge was increased from 3.92 metres to 6 metres, in addition to the increase of the thickness

of the cross-section. However, the vertical displacement is above the limit, and according to figure 70, the largest vertical displacement is -7.57 metres and occurs for Model 2, which has a reduced cross-section height. The smallest maximum vertical displacement is -2.50 metres and occurs for Model 4, which is supported by an extra TLP. By reducing the length between the floaters, the stiffness of the bridge increases, and the vertical displacement is reduced. Another changeable parameter is the moment of inertia, I_z, given by equation 7.1, where H and W is outer height and width of the cross-section, and h and w is the inner height and width.

$$I_z = \frac{WH^3 - wh^3}{12} \tag{7.1}$$

Model 2 has a smaller moment of inertia compared to Model 1 because of the reduced cross-section height. The thickness of the horizontal beams of the cross-section in Model 3 is reduced, and thereby, the inner height of the cross-section is increased. Consequently, Model 2 and Model 3 have larger vertical displacement.

The other displacement studied, was the longitudinal displacement where current and wind have the major influence on the static response. Figures 71a and 71b illustrate the longitudinal displacement for all models for the 1-year and 50-year return period. Two elements in the figures support the previous argumentation about stiff models. First, the static loads give small longitudinal displacement, and secondly, the model with largest displacement, is the model with reduced horizontal thickness.

A deviation between figure 71a and figure 71b, is the position of Model 2 and Model 4. For the 1-year return period, Model 2 has the smallest longitudinal displacement, while Model 4 has the second largest. For the 50-year return period, Model 2 has the second largest longitudinal displacement, while Model 4 has the

smallest displacement. The traffic load is only applied in combination with the 1-year static loads, and according to figure 70, Model 2 has largest vertical displacement, while Model 4 has the smallest vertical displacement. This means that for Model 2, the traffic load causes a smaller longitudinal displacement, while the opposite occurs for Model 4.

The last static response studied in this thesis is the bending moment around the vertical axis. When the traffic load is applied in combination with the 1-year static loads, Model 4 has the largest bending moment, which occurs right before and after the mid-TLP. The bending moment is more similar for the first three models, but smallest for the model with a reduced thickness of the horizontal beams. For the 50-year and 100-year return period, the traffic load is no longer acting, and a result of this is that the bending moment for Model 4 is smaller than for the first three models at its mid-point. The first model achieves the highest bending moment followed by the model with a reduced height.

7.4 Dynamic analysis

The heave response for the first three models were generally larger for TLP1 than for TLP2. This is caused by the water depth where the floaters are positioned. The water depth where TLP1 is located, is larger than the water depth for TLP2, which means that the stiffness applied at TLP1 is smaller. For Model 4, the heave response was similar for TLP1[4] and TLP3[4]. These TLPs are positioned at different water depth, and located closest to land. These end-TLPs are restricted from moving freely because of the boundary condition at the end-nodes.

For the first three models, the sway was largest for the model with a reduced horizontal thickness, and this behaviour is given in figure 72. By reducing the thickness of the horizontal beams, the stiffness of the model is reduced, and larger displace-

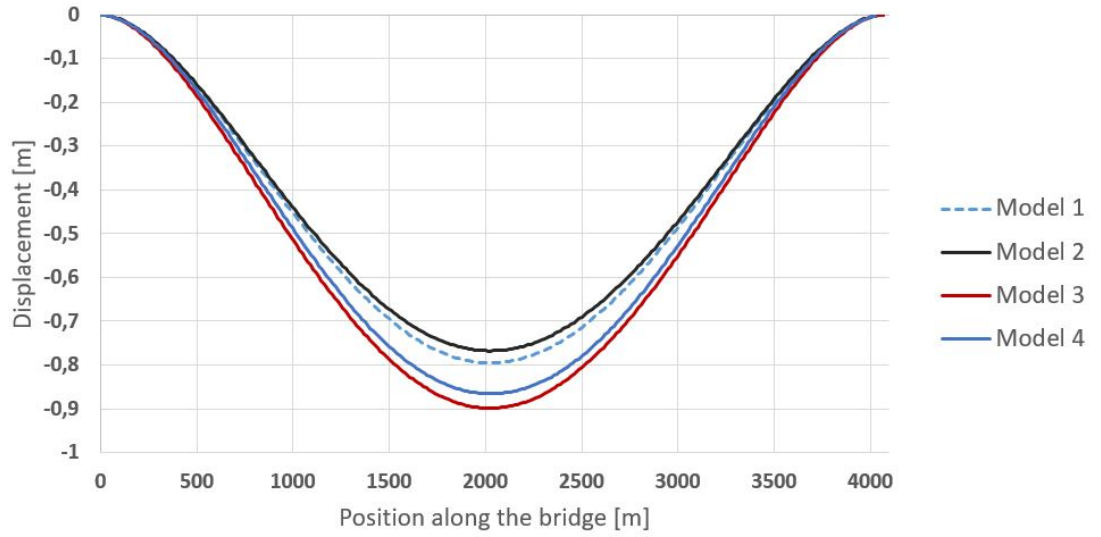

(a) 1-year static loads

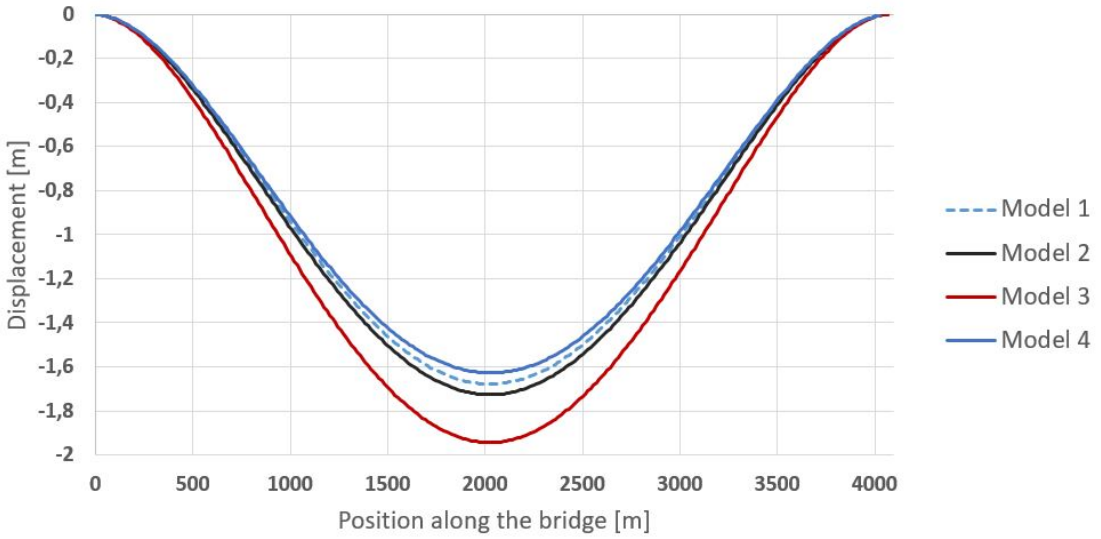

(b) 50-year static loads

Figure 71: Longitudinal displacement for all four models

ment is expected. The longitudinal moment of inertia, I_y, is given by equation 7.2.

$$I_y = \frac{W^3 H - w^3 h}{12} \tag{7.2}$$

The moment of inertia in longitudinal direction is more dependent on the cross-section's width than height. Since the inner and outer width for all models are equal, the inner and outer height causes the difference in longitudinal stiffness. From equation 7.2, it is expected that the response to the model with reduced height is closer to Model 1, which is seen in figure 72.

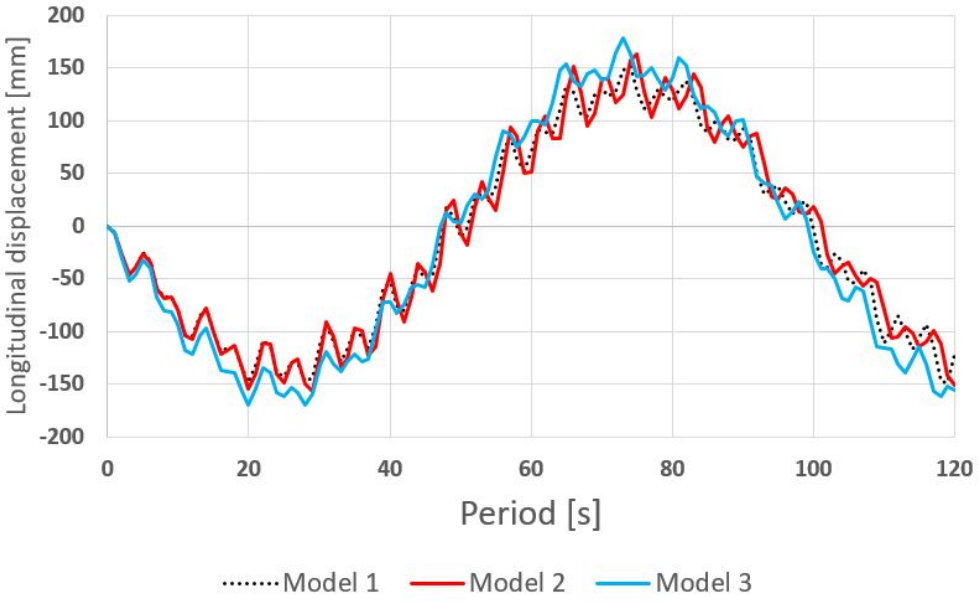

Figure 72: Sway response of TLP1 exposed for a 1-year dynamic wave

The sway response for Model 4 have the same behaviour as for the heave response; the response for TLP1[4] and TLP3[4] are similar and smaller than the response of TLP2[4]. As the return period increases, the displacement becomes smoother. Maximum longitudinal displacement, regardless return period and model, is 0.479 metre, which was obtained for TLP2[4] in Model 4 during a 100-year dynamic wave load. Such a small displacement indicates that the models are too stiff.

The last dynamic analysis was executed by utilizing the first obtained horizontal and vertical eigenfrequency for every model as the wave frequency to the incoming wave. The heave response for the first three models are given in figure 73.

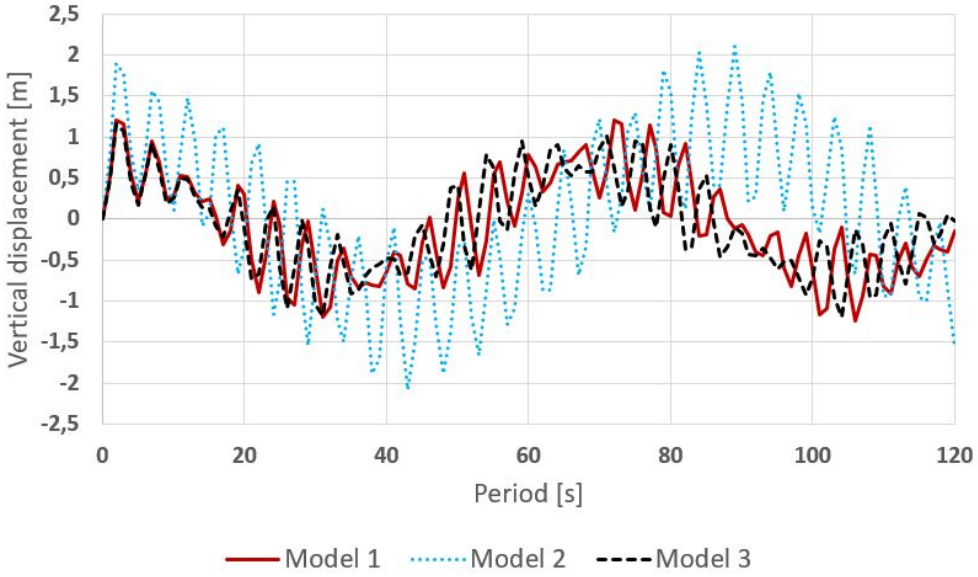

Figure 73: Heave response of TLP1 for the models for 1-year dynamic wave

The applied wave is different for every model since the first obtained horizontal and vertical eigenfrequency are different. Since the first vertical eigenfrequency to Model 1 and Model 3 are similar, the response will be similar, as seen in the figure. The first vertical eigenfrequency to Model 2 is smaller, and this is shown by its maximum occurs for a higher period. The heave response increases dramatically when resonance occur. The models have nearly 2 metres of vertical displacement. The movements are more periodic and the movements are continuous throughout the period of 120 seconds. For Model 4, the applied vertical eigenfrequency is higher than for the first three models, which results in an extra peak, and the achieved maximums are smaller.

The sway response for the first three models is seen in figure 74. Since Model 1 and Model 3 have higher first horizontal eigenfrequency than Model 2, the maximum response occurs at a smaller period compared to Model 2.

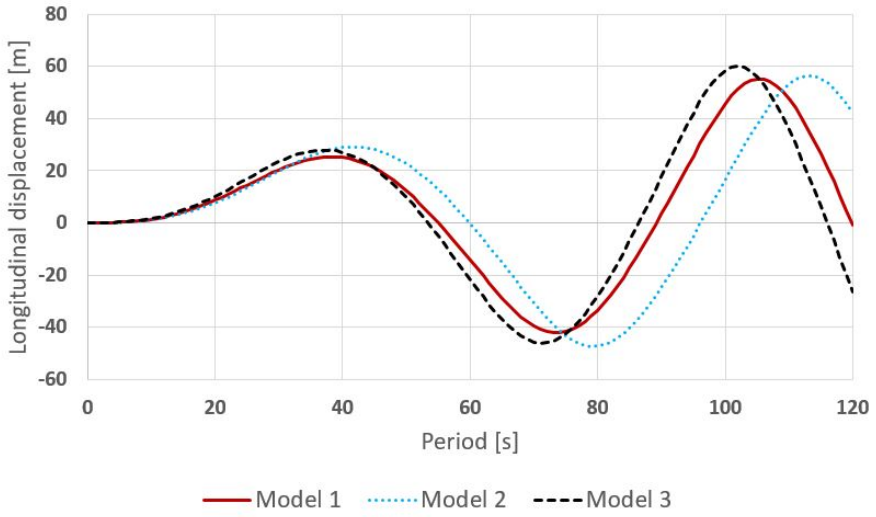

Figure 74: Sway response of TLP1 for the models for 1-year dynamic wave

When resonance occurs, the sway response increases dramatically, and throughout a period of 120 seconds, the maximum responses increase. When a harmonic incoming wave was applied, the displacement was steadier compared to when resonance occur. For Model 4, the sway response is similar as when a harmonic wave was applied; displacement of the mid-TLP is higher than for the end-TLPs.

8 Conclusion and further work

In this thesis, a simplified model of a floating bridge was created in Abaqus/CAE to illustrate static and dynamic analysis. Further, three additional models were created to study how the number of supports and alteration of cross-section affect the responses. From the results, it was demonstrated that by introducing an extra support, the vertical displacement was significantly reduced. Further, the inner cross-section height could be reduced, or the outer cross-section could be increased to reduce the vertical displacement. If only longitudinal loads were acting, these alterations also reduced the longitudinal displacement.

When utilizing a simple model, some of the achieved results were realistic, but nearly all results indicated that the utilized models were too stiff. By introducing a more complex cross-section, i.e. including the stiffeners and girders, the stiffness is slightly reduced and the mass would be significantly reduced. The model will then be able to resist the vertical loads, and at same time give more realistic results in longitudinal direction and for the dynamic results.

References

[1] Statens vegvesen. Ferjefri e39 utviklinsstrategi. Technical report, Statens vegvesen, 2016.

[2] M. M. Lwin. *Floating Bridges*. CRC Press, 2014.

[3] Statens vegvesen. Delprosjekt fjordkryssing. Technical report, Statens vegvesen, 2012.

[4] C.M. Wang and B.T Wang. *Large Floating Structures, Technological Advances*. Springer Singapore, Singapore, 2015.

[5] M. S. Seif and Y. Inoue. Dynamic analyisis of floating bridges. *Marine Structures*, pages 29–46, 1998.

[6] Floating bridge - when is the technology ready? Powerpoint presentation, 2015.

[7] M M. Lwin and J. M. Kulicki. *Bridge Engineering in the United States*. CRC Press, 2013.

[8] Guinness World Records. New bridge in washington state betters longest floating bridge record. `http://www.guinnessworldrecords.com/news/brand-or-agency/2016/4/new-bridge-in-washington-state-betters-longest-floating-bridge-record-425118`, Retrieved: 07-05-2017.

[9] G. Solland, E Landet, and Tronskar J.P. Use of high strength steel in norwegian floating bridges. *Strait Crossings 94*, pages 735–742, 1994.

[10] E. Bratteland. *Floating marine structures in Norway: state of the art*. Port and Harbour Research Institute, 1994.

[11] T. Stabenfeldt. The salhus bridge: Construction and installation. *Strait Crossings 94*, pages 543–546, 1994.

[12] P. Meaas, E. Landet, and V. Vindøy. Design of the salhus floating bridge (nordhordland bridge). *Strait Crossings 94*, pages 729–734, 1994.

[13] E. Watanabe and T. Utsunomiya. Analysis and design of floating bridges. *Progress in Structural Engineering and Materials*, pages 127–144, 2003.

[14] Structurae. West india quay footbridge. `https://structurae.net/structures/west-india-quay-footbridge`, Retrieved: 10-02-2017.

[15] Hawaii for Visitors. Ford island bridge. `http://www.hawaiiforvisitors.com/oahu/attractions/ford-island-photos-02.htm`, Retrieved: 28-04-2017.

[16] M. Nagai, Y. Okui, Y. Kawai, M. Yamamoto, and K. Saito. *Bridge Engineering in Japan*. CRC Press, 2013.

[17] Khaleejtimes. Dubai floating bridge closure on fridays extended. `http://www.khaleejtimes.com/nation/dubai/dubai-floating-bridge-closure-on-fridays-extended`, Retrieved: 10-05-2017.

[18] Partnerships British Columbia. William r. bennett bridge. `http://www.partnershipsbc.ca/projects/operational-complete/william-r-bennett-bridge/`, Retrieved: 2017-05-15.

[19] Statens vegvesen. Statusrapport ferjefri e39. Technical report, Statens vegvesen, 2015.

[20] Coastal highway route e39. Powerpoint presentation, 2015.

[21] Statens vegvesen. K1 and k2 design summary. Technical report, Statens vegvesen, 2016.

[22] Teknisk Ukeblad. Utvikler verdens første hengebru på flytende fundamenter.

[23] Suspension bridge on floating foundations. Powerpoint presentation, 2015.

[24] Multispan suspension bridge on floating foundations. Powerpoint presentation, 2016.

[25] T Moan. *Design of Marine Structures*. 1994.

[26] A Næss and T Moan. *Stochastic Dynamics of Marine Structures*. Cambridge University Press, 2012.

[27] The today file. Thousands lose power as powerful winds hit region. `http://blogs.seattletimes.com/today/2013/11/west-seattle-power-outage-expected-to-continue-into-afternoon/`, Retrieved: 2017-05-07.

[28] Det Norske Veritas. Environmental conditions and environmental loads. *DNV-RP-C205*, 2010.

[29] Det Norske Veritas. Modelling and analysis of marine operations. *DNV-RP-H103*, 2011.

[30] Eurocode 1: Actions on structures - part 2: Traffic loads on bridges. Standard, Comité européen de normalisation, Brussel, 2003.

[31] Traffic loads on road bridges and footbridges. Powerpoint presentation, 2016.

[32] O. M. Faltinsen. *Sea Loads on Ships and Offshore Structures*. Cambridge University Press, 1990.

[33] B. Pettersen. *Marin teknikk 3, Hydrodynamikk*. NTNU, 2007.

[34] Y. A. Cengel and J. M. Cimbala. *Fluid Mechanics, Fundamentals and Applications*. McGraw-Hill, 2006.

[35] R. T. Hudspeth. *Advanced Series on Ocean Engineering : Waves and Wave Forces on Coastal and Ocean Structures*. River Edge, SG: World Scientific Publishing Company, 2006.

[36] Det Norske Veritas. Structural design of tlps (lfrd method). *DNV-OS-C105*, 2008.

[37] I. Senjanović, M. Tomić, and N. Hadžić. Formulation of consistent nonlinear restoring stiffness for dynamic analysis of tension leg platform and its influence on response. *Marine Structures*, pages 1–32, 2013.

[38] K. A. Kvåle, R. Sigbjörnsson, and O. Øiseth. Modelling the stochastic dynamic behaviour of a pontoon bridge: A case study. *Computers and Structures*, pages 123–135, 2016.

[39] E. Watanabe, C.M. Wang, T. Utsunomiya, and T.Moan. Very large floating structures: Applications, analysis and design, 2004.

[40] T. Moan. *Finite Eement Modelling and Analysis of Marine Structures*. NTNU, 2003.

[41] M. A. Crisfield. *Non-linear Finite Element Analysis of Solids and Structures : 1Essentials*. Wiley, Chichester, 1991.

[42] Det Norske Veritas. *Sesam User Manual: Wadam*, 2010.

[43] D.S SIMULIA. *ABAQUS Theory Manual*, 1991-1995.

[44] D. S. SIMULIA. *Abaqus 6.12 Keywords Reference Manual*, 2012.

[45] D. S. SIMULIA. *Abaqus 6.12 Getting started with Abaqus: Interactive Edition*, 2012.

[46] D.S SIMULIA. *Abaqus 6.12 - Analysis User's Manual volume 4*, 1991-1995.

[47] Det Norske Veritas. Design of offshore steel structures general. *DNV-OS-C101*, 2011.

[48] Statens vegvesen. Design basis. Technical report, Statens vegvesen, 2016.

[49] Statens vegvesen. Hovedrapport. Technical report, Statens vegvesen, 2012.

[50] D. Myrhaug and W. Lian. *Marine Dynamics*. NTNU, 2009.

[51] I. Langen and R. Sigbjörnsson. *Dynamisk analyse av konstruksjoner*. Tapir, 1999.

A Linear wave theory

Potential Theory

By applying potential theory, it is assumed that the sea water is incompressible and inviscid and the fluid motion is irrotational[32][33]. Incompressible sea water means that the water has nearly a constant density throughout[34] and small viscous effects can be neglected. Thereby, the fluid is assumed to be inviscid [34]. Irrotational fluid motion means that the fluid particles do not rotate[34]. Mathematically, by assuming irrotational fluid, the vorticity in the fluid must be equal to zero[34], meaning that equation A.1 must hold.

$$\nabla \times \mathbf{V} = 0 \tag{A.1}$$

Where $\mathbf{V}$ is the fluid velocity potential. Since the fluid is assumed irrotational, it follows that the fluid velocity potential[33] is given by equation A.2.

$$\mathbf{V} = \nabla\phi \equiv \mathbf{i}\frac{\delta\phi}{\delta x} + \mathbf{j}\frac{\delta\phi}{\delta y} + \mathbf{k}\frac{\delta\phi}{\delta z} \tag{A.2}$$

Where ϕ is the velocity potential in three dimensions. By inserting equation A.2 into equation A.1, the Laplace equation is obtained and given in equation A.3.

$$\frac{\delta^2\phi}{\delta x^2} + \frac{\delta^2\phi}{\delta y^2} + \frac{\delta^2\phi}{\delta z^2} = 0 \tag{A.3}$$

By combining relevant boundary conditions with equation A.3, the velocity potential for potential theory can be determined[32][33]. The boundary condition for the sea bed is given by equation A.4. It simply means that the water cannot go

through the sea bottom.

$$\left(\frac{\delta\phi}{\delta z}\right)_{z=-h} \tag{A.4}$$

Additional boundary conditions are the kinematic and the dynamic boundary condition.

Kinematic boundary condition

When a fixed body is inserted in a fluid, the boundary condition for its body is given by equation A.5. It simply says that the fluid cannot go through the body or leave the body surface.

$$\left(\frac{\delta\phi}{\delta n}\right)_{on the body surface} = 0 \tag{A.5}$$

The kinematic free-surface condition is given by equation A.6. If a fluid particle has a velocity of $\mathbf{V}$ at time t in point (x, y, z), its motions are given in equation A.6.

$$\frac{DF}{Dt} = \frac{\delta F}{\delta t} + \mathbf{V} \cdot \nabla F \tag{A.6}$$

The free-surface can be defined by equation A.7.

$$z = \zeta(x, y, t) \tag{A.7}$$

where ζ is the wave elevation. The function $F(x, y, z, t)$ can then be defined as

equation A.8 since it is assumed that the fluid particle will remain on the free-surface, in other words, $DF/Dt = 0$.

$$F(x, y, z, t) = z - \zeta(x, y, t) = 0 \tag{A.8}$$

By inserting the definitions in equation A.8, and A.2 into equation A.6 and solving, the kinematic boundary condition is obtained, see equation A.9.

$$\frac{\delta\zeta}{\delta t} + \frac{\delta\phi}{\delta x}\frac{\delta\zeta}{\delta x} + \frac{\delta\phi}{\delta y}\frac{\delta\zeta}{\delta y} - \frac{\delta\phi}{\delta z} = 0 \tag{A.9}$$

Since it is assumed regular waves, only the linear terms in equation A.9 is kept. The linear kinematic boundary condition is then obtained and is given by equation A.10.

$$\frac{\delta\zeta}{\delta t} = \left(\frac{\delta\phi}{\delta z}\right)_{z=0} \tag{A.10}$$

Dynamic free-surface boundary condition

By assuming that the verical z-axis is positive upward, and the gravity is the only external force field, the Bernoulli equation is given by equation A.11.

$$p_0 + \rho g z + \rho\frac{\delta\phi}{\delta t} + \frac{\rho}{2}\mathbf{V}\cdot\mathbf{V} = C \tag{A.11}$$

C is an arbitrary function dependent of time. Equation A.11 is valid for an unsteady, irrotational and inviscid fluid motion[32]. When the atmospheric pressure p_0 and the arbitrary function C are assumed constant, equation A.11 will change

to equation A.12.

$$\left(g\zeta + \frac{\delta\phi}{\delta t} + \frac{1}{2}\left(\left(\frac{\delta\phi}{\delta x}\right)^2 + \left(\frac{\delta\phi}{\delta y}\right)^2 + \left(\frac{\delta\phi}{\delta z}\right)^2\right)\right)_{z=\zeta(x,y,z)} = 0 \tag{A.12}$$

Since the waves are assumed linear, equation A.12 can be linearized and still give sufficient information. By neglected all terms that are not linear, the dynamic boundary conditions is given by equation A.13.

$$g\zeta + \left(\frac{\delta\phi}{\delta t}\right)_{z=0} = 0 \tag{A.13}$$

By inserting the dynamic boundary condition for the free-surface elevation, ζ, into the kinematic boundary condition, equation A.14 is obtained.

$$\left(\frac{\delta^2\phi}{\delta t^2} + g\frac{\delta\phi}{\delta z}\right)_{z=0} = 0 \tag{A.14}$$

Linear wave theory

When the velocity potential is proportional to the wave amplitude, linear theory is fulfilled[32]. By satisfying the Laplace equation, the sea bed boundary condition and the dynamic boundary condition, the velocity potential can be derived[33]. The velocity potential for deep water with propagating regular sinusoidal waves, is given by equation A.15.

$$\phi = \frac{g\zeta_a}{\omega}e^{kz}\cos(\omega t - kx) \tag{A.15}$$

The relationship between the wave number, k, and the wave frequency, ω, are given in equation A.16 when the kinematic boundary condition are satisfied.

$$\omega^2 = kg \tag{A.16}$$

For a regular sinusoidal propagating wave, the velocity potential and the relationship between the wave number and the wave frequency are given in equation A.17 and A.18, respectively, when the water depth is finite.

$$\phi = \frac{g\zeta_a}{\omega} \frac{\cosh k(z+h)}{\cosh(kh)} \cos(\omega t - kx) \tag{A.17}$$

$$\omega^2 = kg \tanh(kh) \tag{A.18}$$

The relation between the wave period, T, and wave frequency for both deep water and finit water, is given by equation A.19.

$$T = \frac{2\pi}{\omega} \tag{A.19}$$

B Eigenvalues obtained by shift

When some eigenvalues, and thereby some eigenfrequencies, are wanted, vector iteration can be used[51]. To explain direct vector iteration and inverse iteration, the special eigenvalue problem is introduced. By assuming that $\mathbf{M}$ is symmetric and invertible, the special eigenvalue problem can be obtained by using Cholesky decomposition of $\mathbf{M}$. Thus,

$$\mathbf{M} = \mathbf{L}\mathbf{L}^T$$

Introducing a new eigenvector, $\mathbf{x}$

$$\begin{aligned} \mathbf{x} &= \mathbf{L}^T\phi \\ \phi &= \left(\mathbf{L}^T\right)^{-1}\mathbf{x} \end{aligned}$$

When inserting the new eigenvector and decomposition of the mass matrix, the general eigenvalue is given by equation B.1.

$$\left[\mathbf{K} - \omega^2\mathbf{L}\mathbf{L}^T\right]\left(\mathbf{L}^T\right)^{-1}\mathbf{x} = 0 \tag{B.1}$$

By multiply equation B.1 with $\mathbf{L}^{-1}$, the equation becomes

$$\mathbf{L}^{-1}\left[\mathbf{K} - \omega^2\mathbf{L}\mathbf{L}^T\right]\left(\mathbf{L}^T\right)^{-1}\mathbf{x} = 0 \tag{B.2}$$

When introducing $\mathbf{A} = \mathbf{L}^{-1}\mathbf{K}\left(\mathbf{L}^T\right)^{-1}$ and the eigenvalue, λ, the special eigenvalue problem is given by equation B.3.

$$(\mathbf{A} - \lambda \mathbf{I})\,\mathbf{x} = 0 \tag{B.3}$$

Direct vector iteration

Direct vector iteration is a recursive relation, and for the special eigenvalue problem, it is given by

$$\mathbf{z}_k = \mathbf{A}\mathbf{z}_{k-1} \qquad k = 1, 2, \ldots n \tag{B.4}$$

Where $\mathbf{z}$ is an approximation to the eigenvector $\mathbf{x}$, and is given as

$$\mathbf{z} = c_1\mathbf{x}_1 + c_2\mathbf{x}_2 + \cdots + c_n\mathbf{x}_n = \sum_{i=1}^{n} c_i\mathbf{x}_i \tag{B.5}$$

It can be shown that the direct vector iteration will give the largest eigenvalues by deducing equation B.4. First, the eigenvalues are reorganized in increasing order, hence

$$|\lambda_1| \leq |\lambda_2| \leq \cdots \leq |\lambda_{n-1}| < |\lambda_n| \tag{B.6}$$

By deducing equation B.4

$$
\begin{aligned}
\mathbf{z}_0 &= c_1\mathbf{x}_1 + c_2\mathbf{x}_2 + \cdots + c_n\mathbf{x}_n \\
\mathbf{z}_1 &= c_1\lambda_1\mathbf{x}_1 + c_2\lambda_2\mathbf{x}_2 + \cdots + c_n\lambda_n\mathbf{x}_n \\
&= \mathbf{z}_0\mathbf{A} \\
\mathbf{z}_2 &= c_1\lambda_1^2\mathbf{x}_1 + c_2\lambda_2^2\mathbf{x}_2 + \cdots + c_n\lambda_n^2\mathbf{x}_n \\
&= \mathbf{A}\mathbf{z}_1 = \mathbf{A}^2\mathbf{z}_0 \\
\mathbf{z}_k &= c_1\lambda_1\mathbf{x}_1 + c_2\lambda_2\mathbf{x}_2 + \cdots + c_n\lambda_n\mathbf{x}_n \\
&= \mathbf{A}\mathbf{z}_{k-1} = \mathbf{A}^k\mathbf{z}_0
\end{aligned}
\tag{B.7}
$$

It can be shown that the direct vector iteration gives the largest eigenvalues. Since the eigenvalues are in increasing order, equation B.7 becomes

$$
\mathbf{z}_k = \lambda_n^k \left\{ c_n\mathbf{x}_n + c_{n-1}\left(\frac{\lambda_{n-1}}{\lambda_n}\right)^k \mathbf{x}_{n-1} + \cdots + c_1\left(\frac{\lambda_1}{\lambda_n}\right)^k \mathbf{x}_1 \right\} \tag{B.8}
$$

As can be seen in equation B.8, the first term on the right-hand side will be the dominated term since all the other terms will have a small value. Hence, the direct vector iteration will give the highest eigenvalue. Since, the smallest eigenvalue is of most interest, the inverse iteration will be used. The reason for this, is that the inverse of the highest value is the same as the smallest value.

Inverse iteration

The inverse eigenvalue problem for the special eigenvalue problem is given as

$$
\mathbf{A}^{-1}\mathbf{x} = \frac{1}{\lambda}\mathbf{x} \tag{B.9}
$$

Deducing the direct vector iteration with the inverse eigenvalue, equation B.10 is

obtained.

$$\mathbf{z}_k = \mathbf{A}^{-1}\mathbf{z}_{k-1} \tag{B.10}$$

Equation B.10 can also be written as

$$\mathbf{z}_{k-1} = \lambda \mathbf{z}_k \tag{B.11}$$

By multiplying equation B.11 with $\mathbf{z}^T$ and solve for λ, the Rayleigh quotient for the special eigenvalue problem is obtained, see equation B.12.

$$\lambda_R = \lambda = \frac{\mathbf{z}^T\mathbf{z}_{k-1}}{\mathbf{z}^T\mathbf{z}_k} \tag{B.12}$$

The same procedure can be used for the general eigenvalue problem. Hence, the Rayleigh-quotient for the general eigenvalue problem which find the smallest eigenvalues are given by equation B.13.

$$\lambda_R = \omega^2 = \frac{\mathbf{z}^T\mathbf{M}\mathbf{z}_{k-1}}{\mathbf{z}^T\mathbf{M}\mathbf{z}_k} \tag{B.13}$$

By using equation B.14, the smallest eigenfrequency of the system is obtained.

$$\omega = \sqrt{\lambda_R} \tag{B.14}$$

However, it is not only the smallest eigenfrequency that are of interest. Thus, by introducing a shift, other eigenvalues can also be obtained[51]. By introducing a shift, μ, the eigenvalue for the general problem will the be given by equation B.15.

$$\lambda_i = \bar{\lambda}_i + \mu \tag{B.15}$$

Where $\bar{\lambda}_i$ is the new eigenvalue, μ is the shift value and λ_i is the eigenvalue. When introducing a shift, it means that the axis move along the x-axis to determine the eigenvalues[51]. In other words, when introduce a shift, the iteration will converge to the eigenvalue λ_i which is closest to the shift[51]. By inserting equation B.15 into equation 3.3, the general eigenvalue will then be given by equation B.16.

$$\left(\mathbf{K} - \left(\bar{\lambda}_i + \mu\right)\mathbf{M}\right)\phi = 0 \tag{B.16}$$

Inverse iteration with the introduced shift will then be given by equation B.17[51].

$$\left(\mathbf{K} - \mu\mathbf{M}\right)\mathbf{z}_k = \mathbf{M}\mathbf{z}_{k-1} \tag{B.17}$$

Hence, the eigenvalue is given by equation B.18, which says that the eigenvalue will converge to the eigenvalue which is closest to the introduced shift.

$$\lambda_i = \mu + \bar{\lambda}_i = \mu + \frac{\mathbf{z}_k^T\mathbf{M}\mathbf{z}_{k-1}}{\mathbf{z}_k^T\mathbf{M}\mathbf{z}_k} \tag{B.18}$$

C Attached Excel-files

Convergence of added mass and damping to the floater

The convergence grade of added mass and damping to the floater is given in the excel-document AddedMass.xlsx, in the attached folder HydroD/Results. In addition, a file for every meshes executed, are found in this folder.

Calculated stiffness

The calculated stiffness applied as the tethers at the floaters are given in the excel-sheet UtregningBro.xlsx, in the attached folder Calculations.

COB and COG

The calculated centre of buoyancy and centre of gravity to the floater is given in the excel-sheet COBandCOG.xlsx, in the attached folder Calculations.

Current

The calculated current load is given in the excel-sheet Loads.xlsx, in the attached folder Calculations.

Traffic

The Traffic load is given in the excel-sheet Loads.xlsx, in the attached folder Calculations.

Wave

The horizontal and vertical wave load, for small wave periods and when the first horizontal and vertical eigenfrequency is utilized as the wave frequency, are given in the excel-sheet Loads.xlsx, in the attached folder Calculations.

Wind

The wind load is given in the excel-sheet Loads.xlsx, in the attached folder Calculations.